A MEMS THERMOELECTRIC ENERGY HARVESTER FOR ENERGY GENERATION IN MOBILE SYSTEMS

A THESIS SUBMITTED TO
THE GRADUATE SCHOOL OF NATURAL AND APPLIED SCIENCES
OF
MIDDLE EAST TECHNICAL UNIVERSITY

BY

EMRE TAN TOPAL

IN PARTIAL FULFILLMENT OF THE REQUIREMENTS
FOR
THE DEGREE OF MASTER OF SCIENCE
IN
MICRO AND NANOTECHNOLOGY

SEPTEMBER 2011

Approval of the thesis:

A MEMS THERMOELECTRIC ENERGY HARVESTER FOR ENERGY GENERATION IN MOBILE SYSTEMS

submitted by **EMRE TAN TOPAL** in partial fulfillment of the requirements for the degree of **Master of Science in Micro and Nanotechnology Department, Middle East Technical University** by,

Prof. Dr. Canan Özgen _____
Dean, Graduate School of **Natural and Applied Sciences**

Prof. Dr. Mürvet Volkan _____
Head of Department, **Micro and Nanotechnology**

Assoc. Prof. Dr. Haluk Külah _____
Supervisor, **Electrical and Electronics Eng. Dept., METU**

Prof. Dr. Tuna Balkan _____
Co-Supervisor, **Mechanical Eng. Dept., METU**

Examining Committee Members

Prof. Dr. Tayfun Akın _____
Electrical and Electronics Eng. Dept., METU

Assoc. Prof. Dr. Haluk Külah _____
Electrical and Electronics Eng. Dept., METU

Prof. Dr. Tuna Balkan _____
Mechanical Eng. Dept., METU

Assist. Prof. Dr. Ali Muhtaroğlu _____
Electrical and Electronics Eng. Dept., METU NCC

Dr. Özge Zorlu _____
METU MEMS Research and Application Center

Date: 13.09.2011

I hereby declare that all information in this document has been obtained and presented in accordance with academic rules and ethical conduct. I also declare that, as required by these rules and conduct, I have fully cited and referenced all referenced material and results that are not original to this work.

Name, Surname: Emre Tan TOPAL

Signature:

ABSTRACT

A MEMS THERMOELECTRIC ENERGY HARVESTER FOR ENERGY GENERATION IN MOBILE SYSTEMS

Topal, Emre Tan

M. Sc., Micro and Nanotechnology Department

Supervisor: Assoc. Prof. Dr. Haluk Külah

Co-supervisor: Prof. Dr. Tuna Balkan

September 2011, 157 pages

In this thesis design, optimization, fabrication and performance characterization of MEMS thermoelectric (TE) energy harvesters for harnessing waste heat in mobile systems are presented. As a proof of concept, chromium and nickel are used as the thermoelectric material in the proposed design. The feasibility of the state of the art thermoelectric materials is also discussed.

MEMS TE energy harvesters proposed in this study are designed to generate power at relatively lower ΔT values. The performance of the MEMS TE energy harvesters was optimized using analytical and 3-D finite element models. An analytical code

was used for profiling the electrical power output with varying geometry. The design points with maximum generated power were selected, and the microfabricated thermoelectric energy harvesters were designed accordingly. The fabricated devices are formed on a silicon wafer and composed of Nickel and Chromium thermocouples on SiO_2/Si_3N_4 diaphragms, and Titanium heater and monitor resistors for testing purposes.

Microfabrication was followed by the performance characterization of MEMS TE energy harvesters with the conducted tests. For 10 °C temperature difference between the hot and cold junctions (a heat source at 35 °C), the proposed TE energy harvesters are capable of providing 1.1 $\mu W/cm^2$ power density and 1.71 V voltage. The performance of the thermoelectric generators in general is limited by Carnot cycle efficiency. Nevertheless, the validated practical performance of MEMS TE energy harvesters proposed in this thesis is comparable to other examples in literature. It is anticipated by the calculations that this design will be able to provide the highest thermoelectric efficiency factor (4.04 $\mu W/K^2cm^2$) among the lateral TE energy harvesters if thermoelectric materials having high Seebeck coefficient values (such as p-Si, n-Si, polysilicon, Bi_2Te_3 etc.) are used. According to the performance results, the MEMS TE energy harvesters can be implemented in mobile systems to convert waste heat into electricity. The fabrication process can be adapted to CMOS with some modifications if needed. The lateral MEMS thermoelectric energy harvesters can also be combined with vibration energy harvesters to realize multi-mode energy scavenging.

For prospective study, vertical thermoelectric generator configurations are also discussed in order to further increase the power density generated. The finite element simulations for proposed vertical configurations with air and water convection were completed. The vertical TE generators proposed can supply up to 4.2 mW/cm^2 with a heat source at a temperature of 310 K.

Keywords: energy harvesting, thermoelectric conversion, heat transfer, energy generation, MEMS, finite element method

ÖZ

MOBİL SİSTEMLERDE ENERJİ HARMANLAMA İÇİN MEMS TERMOELEKTRİK ENERJİ ÜRETECİ

Topal, Emre Tan

Yüksek Lisans, Mikro ve Nanoteknoloji Bölümü

Tez Yöneticisi: Doç. Dr. Haluk Külah

Ortak Tez Yöneticisi: Prof. Dr. Tuna Balkan

Eylül 2011, 157 sayfa

Bu tez çalışmasında, mobil sistemlerde ısıdan enerji harmanlayan MEMS tabanlı termoelektrik enerji üreteçlerinin tasarımı, optimizasyonu, üretimi ve performans karakterizasyonu yapılmıştır. Konseptin doğrulanması amacıyla, Cr ve Ni metallerinin termoelektrik malzeme olarak kullanıldığı MEMS tabanlı termoelektrik mikrojeneratörler üretilmiştir. Ayrıca, son teknoloji termoelektrik malzemelerin tasarımda uygulanabilirliği değerlendirilmiştir.

MEMS TE enerji üreteçleri, sıcaklık farkının nispeten daha düşük olacağı uygulamalara uygun olarak tasarlanmıştır. MEMS TE enerji üreteçlerinin performans analizi analitik modellerle ve 3 boyutta sonlu eleman simülasyonları vasıtasıyla yapılmıştır. Analitik hesaplardan maksimum gücün elde edilebileceği

tasarım parametreleri belirlenmiş, ve üretilecek tasarımlar bu bilgilere göre yapılmıştır. MEMS fabrikasyonu için kullanılacak maskeler bu bilgiler ışığında çizilmiştir. Üretilen aygıtlar silicon pul üzerinde, SiO_2/Si_3N_4 diyaframlar, Ni ve Cr termokupullar, ve test amacıyla üretilen Ti ısıtıcı ve monitör dirençlerden oluşmaktadır.

MEMS TE çiplerin üretiminden sonra performans karakterizasyonu için testler yapılmıştır. Uygulama alanına göre sıcaklık farkları daha fazla veya daha az olabilir. Isı kaynağının 35 °C olduğu bir durumda (ΔT=10 °C), Cr ve Ni kullanılan MEMS TE enerji üreteçleri 1.1 $\mu W/cm^2$ elektriksel güç sığası ve 1.71 V/cm^2 voltaj üretebilir. Termoelektrik enerji çevrimi, termodinamik olarak Carnot çevrimi verimliliği ile sınırlıdır. Buna rağmen, sunulan MEMS TE tasarımı enerji sığası açısından literatürde sunulan örneklerle karşılaştırılabilecek durumdadır. Seebeck katsayısı yüksek termoelektrik malzemeler (p-Si, n-Si, polysilicon, Bi_2Te_3 vb.) kullanılması halinde, üretilen enerji sığasının (4.04 $\mu W/K^2cm^2$) bilgimiz dahilinde literatürde sunulan diğer termoelektrik üreteçlere üstünlük sağlayacağı yapılan hesaplamalarla öngörülmektedir. Ayrıca, sunulan TE üreteç tasarımı uygun bir paketlemeyle CPU üzerinden yayılan fazla ısıyı elektrik enerjisine dönüştürmeye uygundur. Üretim yöntemi, bazı değişikliklerle CMOS'a adapte edilebilir. Ayrıca yatay MEMS TE enerji üreteçleri titreşimden enerji harmanlama ile birleştirilerek çok kaynaklı enerji harmanlama gerçekleştirilebilir.

İleriye yönelik bir çalışma olarak, güç sığasını daha da yükseltmek amacıyla dikey termoelektrik konfigürasyonları tasarlanmıştır. Hava ve su soğutmalı konfigürasyonlar için dikey TE jeneratörlerin performansı sonlu elemanlar yöntemi ile hesaplanmıştır. Dikey TE jeneratörlerin, 310 K sıcaklıktaki bir ısı kaynağı kullanıldığında 4.2 mW/cm^2 güç üretebildiği hesaplanmıştır.

Anahtar Kelimeler: enerji harmanlama, termoelektrik çevrim, ısı transferi, enerji üretimi, MEMS, sonlu elemanlar metodu

To my parents, my sister Gizem and my beloved Hilâl

ACKNOWLEDGMENTS

I would like to thank my thesis supervisor, Assoc. Prof. Dr. Haluk Külah for his guidance throughout my study and his patience. He has been the person to show me the importance of self-discipline and dedication in every work done.

My foremost thanks go to Dr. Ali Muhtaroğlu, who supported this work and always encouraged me to do better with his helpful and positive nature. His contribution is priceless, which made this study valuable. I also like to thank my co-supervisor Tuna Balkan for his nice behavior and warm attitude. I am grateful to Dr. Özge Zorlu for his invaluable help through all the phases of my thesis study. I would also like to thank him for his great support through difficult times that helped me to gain the motivation I needed to complete my thesis. I give my many thanks to Hakan Töreyin for broadening my vision and providing a correct methodology in the assignments we have done together. I thank my colleagues and my friends Levent Beker and Serol Türkyılmaz, for their company at good times and bad times. I thank to all of my colleagues in METU MEMS Center, especially Mert Torunbalcı, Başak Kebapçı, Hatice Ceylan, Ufuk Şenveli, Evrim Özçakır, Numan Eroğlu, Selçuk Keskin who helped me with the fabrication. I am grateful to Akın Aydemir for his efforts and his never ending patience in completing the fabrication. I wouldn't be able to finish my work in a limited time if he hadn't contributed so much in the completion phase of the fabrication. I also like to thank Orhan Akar for sparing his valuable time and his guidance in METU MEMS Center. He provided me the discipline and inquisitive point of view to complete my work attentively.

I would like to thank my other half, Hilâl Kantekin, for her endless support and her love that keeps me strong at all times. I could never repay her for her contributions.

My special thanks go to my parents Z. Esen and Yaşar Topal, for supporting me in every condition. I would never have accomplished this much if it hadn't been for them.

This study is supported by the Scientific and Technological Research Council of Turkey (TÜBİTAK) under grant number 109E220; and MER, a partnership between Intel Corporation and King Abdul-Aziz City for Science and Technology, to conduct and promote research in the Middle East.

TABLE OF CONTENTS

LIST OF FIGURES

FIGURES

LIST OF TABLES

TABLES

CHAPTER 1

INTRODUCTION

For powering mobile electronic devices, batteries have long been used. However, as the power need of electronic components increase, battery technology progresses slowly. Increasing the energy density of batteries with the use of new materials and chemical structure has been the focus in recent years. However, battery technology advances much more slowly than the power need itself. Therefore, self-sufficient systems which generate their own power are being developed for the last few decades. Although autonomous systems and energy generation from ambient sources is not a new concept, 'energy harvesting' concept has been the increasing trend in recent years.

Energy generation in microscale can be done by microbatteries, micro fuel cells and energy harvesting. Microbatteries involve electrochemical compounds that pose threat to environment in the long run. Moreover, the energy density of microbatteries is becoming limited as the energy conversion systems scale down. Microfuel cells, on the other hand, have high energy output potential. However, they still need an external fuel source to run, and complex conversion methods are practiced for reliable operation. Energy harvesting is used to convert ambient energy sources (heat, light, vibration, sound, RF waves) into useful electricity [1]. Energy harvesting is preferred over microbatteries and fuel cells as it has high power density, poses no threat to environment and the ambient energy sources are inexhaustible. Energy harvesting divides into two in itself: active and passive harvesting systems. In active energy conversion system like vibration energy harvesting, moving parts are needed to utilize the electricity generation. Electromagnetic, electrostatic, and

piezoelectric conversion are mostly used in vibration energy harvesting [2]. In passive energy harvesting systems, no moving parts are needed for energy conversion. Photovoltaic, thermoelectric, fuel cells, and pyroelectric systems can be shown as examples of passive conversion systems. In these types of systems, the efficiency of the system mostly relies on the efficient implementation physical phenomena and the conversion characteristics of the materials used in addition to the design. Thermoelectric energy harvesting is a common method through these passive conversion systems as it supplies an uninterrupted voltage and waste heat sources are virtually unlimited in almost every industrial or household environment. The knowledge background and fabrication technology for thermoelectric energy generation is well established, providing reliable operation in every application.

In this study, thermoelectric energy harvesting is the main scope. The design and fabrication of MEMS based thermoelectric energy harvesters are explained. Thermoelectric energy harvesting has been of interest for many decades. In industrial machines, aerospace applications, automotive industry thermoelectric energy generation has been in use for a long time [3]. There is ambient heat everywhere in our daily life. Human body, electric devices, mobile systems (notebooks, netbooks, PDA's), industrial machines are all sources of heat generation. There is a need to recycle some of this waste heat into electricity in order to increase the overall efficiency of these systems. There are several methods to convert this excess heat: thermoelectricity, pyroelectricity, thermophotovoltaic systems. Though not the most efficient of all, thermoelectric energy conversion has been one of the most practical and cheapest methods. Some of the waste heat can be converted to electricity to supplement the energy need of a system. Even some of the electronic components could be solely run from this excess heat energy. In satellites and space shuttles, thermoelectric layers on the surface supplement solar harvesting systems to generate electricity from heat. In thermoelectric energy harvesting, state of the art materials like Bi_2Te_3, Sb_2Te_3 having high figure of merit are used to increase efficiency.

In mobile electronic systems (notebooks, netbooks, smart phones, PDA's) there are various components that generate excess heat energy. In notebooks, the LCD

displays, CPU, and even batteries are the components that generate most excess heat while in operation. Some of this excess heat can be harnessed to provide electric power to low power electronic components. The energy generated can supplement the battery as well. In this way, the mobile systems can operate on battery for longer times. The area where this excess heat created is also large enough in these systems, when a system with a high energy density is designed. For example, in LCD screens there is at least an area of few tens of cm^2 area where excess heat can be harnessed. When a steady heat source is available, thermoelectric energy harvesters can provide uninterrupted DC voltage.

Thermoelectric energy harvesters are mostly in the form of solid state converters, where Seebeck effect of materials is utilized for voltage generation. State of the art materials (Bi_2Te_3, Sb_2Te_3, SbTe, InAs, YBCO) have a high Seebeck coefficient which results in higher voltage and power generation. Figure of merit is an important consideration in benchmarking of thermoelectric materials, which is discussed in Chapter 2.

1.1 Thermoelectric Generator Designs

Thermoelectric generators reported in literature are either lateral or vertical in terms of heat flow path. MEMS fabrication techniques, especially surface micromachining is more suitable for the production of lateral thermoelectric energy harvesters. In lateral thermoelectric energy harvesters, the thermocouples lie on x-y plane, and the temperature difference is created in this plane. A substrate is used as the heat sink, on which the cold junctions reside. This heat sink further allows the heat flow to a larger heat sink (could be a metal plate or base) where the temperature is kept at room temperature. Larger the heat sink and the base it's connected to, larger the heat capacitance of the cold side of the complete system. This provides a high temperature difference between the hot and cold junctions, hence a superior thermoelectric power.

On the other hand, the vertical thermoelectric harvesters consist of thermoelectric columns connected in series with a bonding layer. This type of generator has thermally conductive ceramic on top and bottom of the columns. These conductive

ceramics are used to couple the thermoelectric generators to a heat source and sink. The temperature difference is created between the top and bottom of the columns, namely the z-direction.

One of the earlier examples of lateral TE energy harvesters is the work of Glosch et al. [4]. This generator fabricated by microfabrication utilizes p-doped silicon and aluminum lateral couples on a diaphragm for thermoelectric energy generation. A power of 1.5 μW could be extracted from a 11mm x 1.5mm prototype. This power is used to drive a preamplifier and a small sensor. The TE design is seen in Figure 1.1.

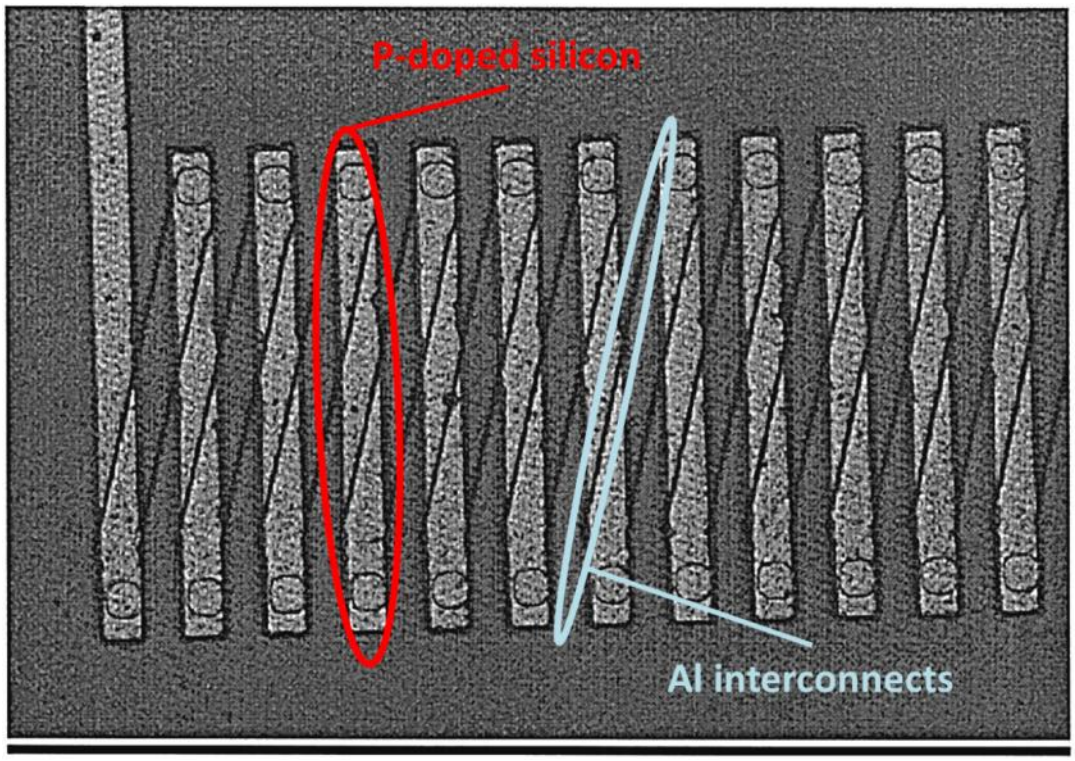

Figure 1.1. Lateral type thermoelectric generator. p- and n-silicon thermopile is shown [4].

Another lateral TE design is the work of Strasser et al. [5]. In this design, n polysilicon and p polysilicon are used as n-and p-type thermoelectric materials. The device is able to generate 5 volts of Seebeck voltage and 1 μW electrical power with 5 K temperature difference between the hot and cold junctions. The device structure is shown in Figure 1.2.

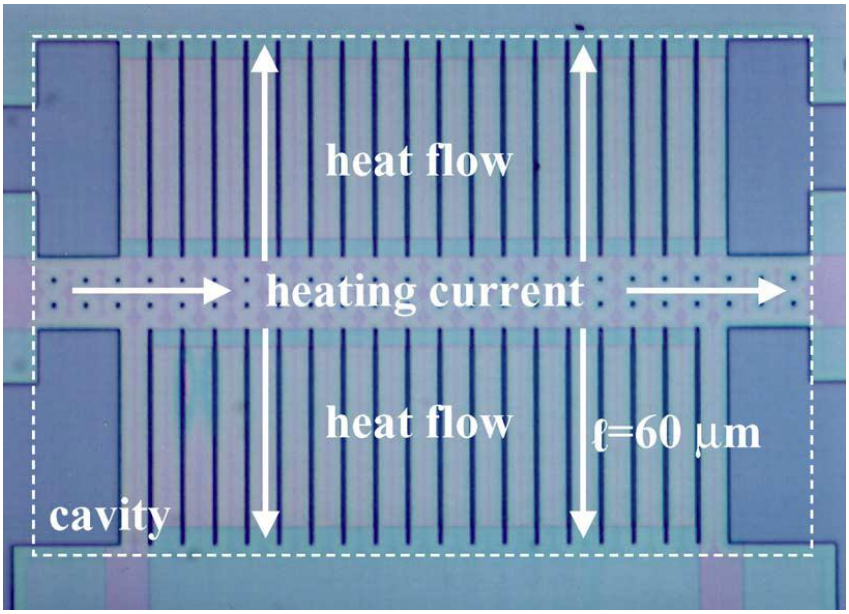

Figure 1.2. The lateral TE harvester utilizing poly-Si and poly-SiGe as thermoelectric materials [5].

One interesting state of the art example in lateral TE energy harvesters is the work of Wang et al. [6]. Bi_2Te_3 nanowires are synthesized to be used as the thermoelectric material in this work. The process involves potentiastatically electrodeposition of Bi_2Te_3 powders for the formation of nanowire thermoelectric layers. The nanowire Bi_2Te_3 thermolegs of the energy harvester and the schematic of the harvester structure from top are shown in Figure 1.3.

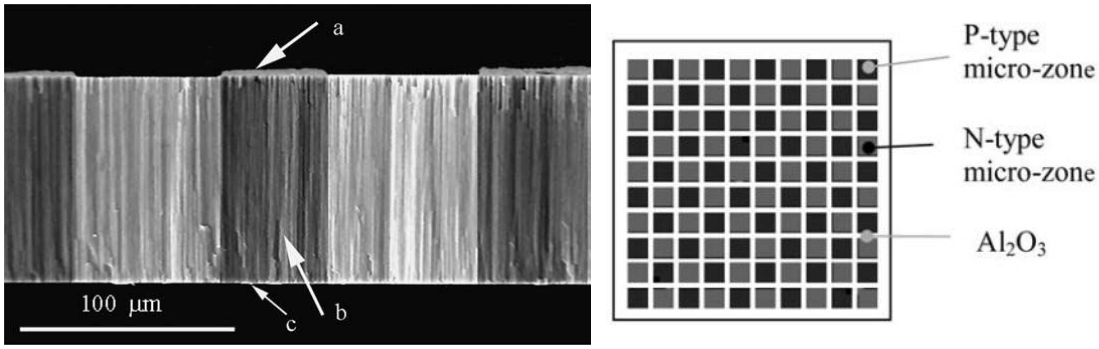

Figure 1.3. Synthesized Bi_2Te_3 nanowires assembled on the alumina template [6].

Weber et al. introduced a foil shaped thermoelectric energy harvester fabricated by screen printing method. The thermocouples are patterned on a flexible polyimide

substrate for energy generation for wrist watches. This design allows stacking of many Sb and Bi thermocouples in a limited area and increased thermoelectric power [7]. The fabricated devices are seen in Figure 1.4.

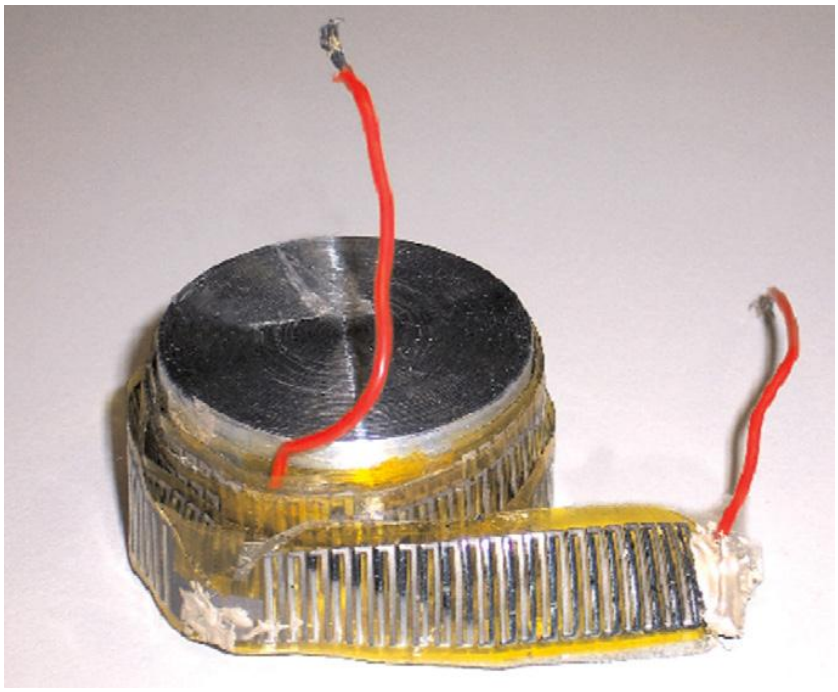

Figure 1.4. Foil shaped flexible thermoelectric energy harvester [7].

The second type of thermoelectric energy harvesters is the vertical TE harvesters. There are several fabrication methods to produce these thermoelectric harvesters, most of which include high temperature process steps.

Snyder et al. [8] introduced a more MEMS-like fabrication method, where Cu and Ni metals are electroplated at a high aspect ratio. BiTe was also utilized with the same fabrication method. An electrical power of 40 $\mu W/cm^2$ can be obtained from the devices. The fabrication is seen briefly in Figure 1.5.

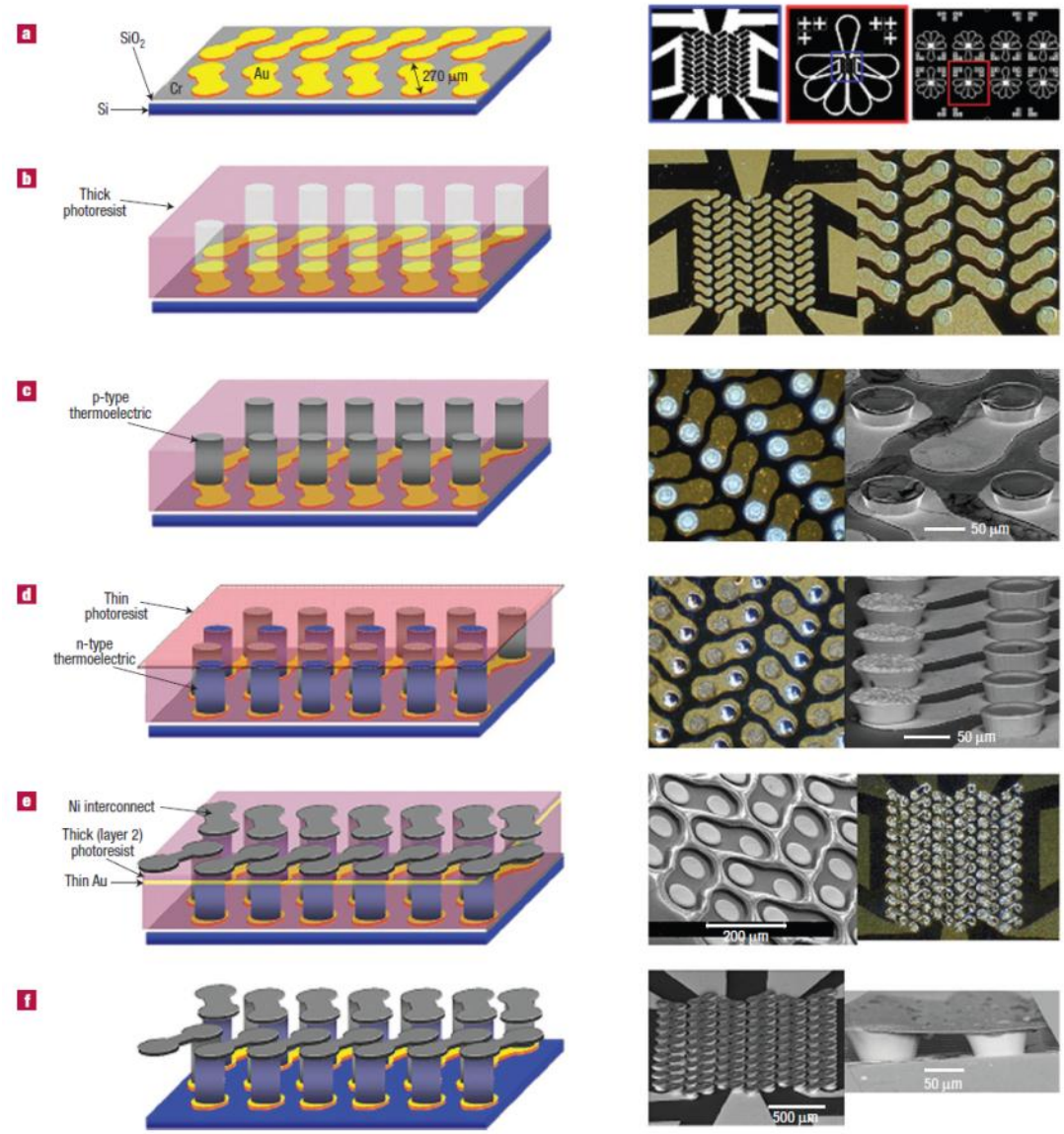

Figure 1.5. The vertical TE energy harvester fabricated by electrodeposition. All the fabrication steps are illustrated and shown by pictures [8].

BiTe and SbTe sintered powders can also be used in vertical TE energy harvesters. A distinctive fabrication process is developed by Li et al. where sintered BiTe powder is used as thermoelectric material. The fabrication process is briefly based on preparing a mold on silicon substrate by DRIE, and patterning the thermoelectric legs in these molds. The thermoelectric device formed of sintered thermoelectric material powders is seen in Figure 1.6 [9].

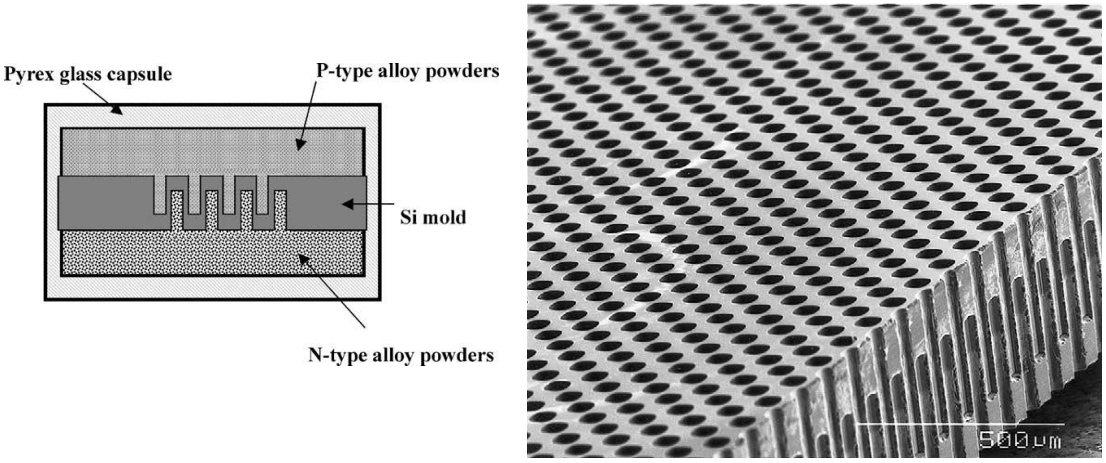

Figure 1.6. a) The structure of the TE energy harvester using Si mold and thermoelectric material powders, b) The SEM photograph of the micromachined Si mold [9].

One of the earliest implementation of thermoelectric energy harvesting for autonomous systems is the vertical TE harvester fabricated for Casio thermic watches. In this study, the thermocouples are formed by dicing, aligning and bonding [10], [11]. The fabrication is a straightforward and practical one, and a power of 22.5 μW and a steady DC voltage of 20 mV can be obtained in this design. The fabrication and prototype is seen in Figure 1.7.

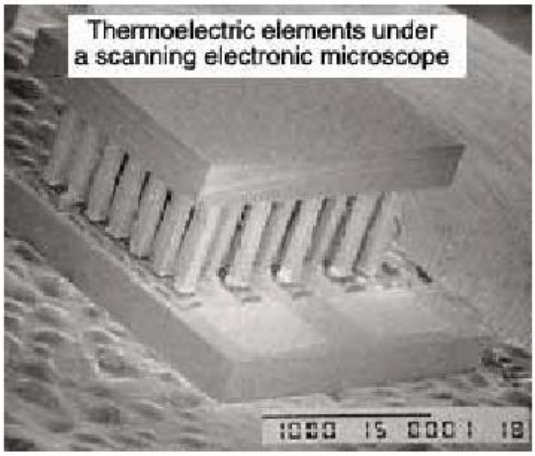

Figure 1.7. Vertical TE energy harvester designed for Casio thermic watches [10].

Other non-conventional methods like micro-jet printing of thermoelectric material also are applied [12]. The Seebeck coefficient of printed powders can reach half of

their maximum values by conventional fabrication methods. This type of fabrication provides easy and cheap implementation. The fabrication can also be done on flexible substrates. The wax molds for patterning thermoelectric samples prepared by this method are shown in Figure 1.8.

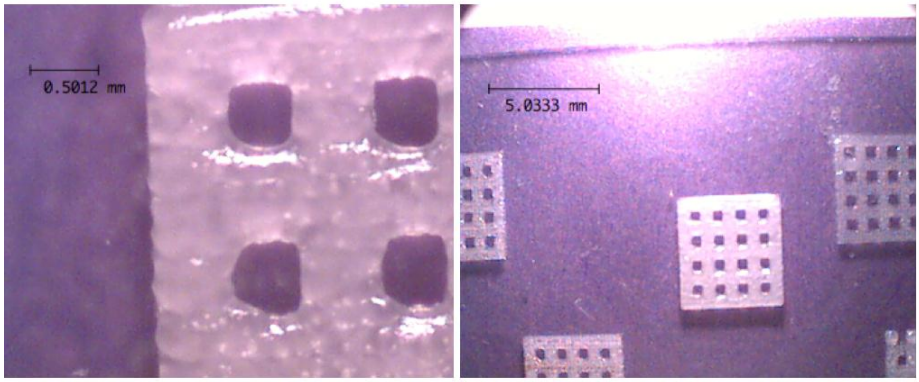

Figure 1.8. Wax mold for patterning the printed thermoelectric powders [12].

More conventionally, physical vapor deposition (PVD) can be used to form vertical thermocouples. In [13], [14], the heights of the couples prepared by PVD could reach up to 5 micrometers. The electrical power generated in this study is 1.2 $\mu W/cm^2$ for 100°C temperature difference between the junctions. The 3-D thermoelectric generator structure from the top is seen in Figure 1.9.

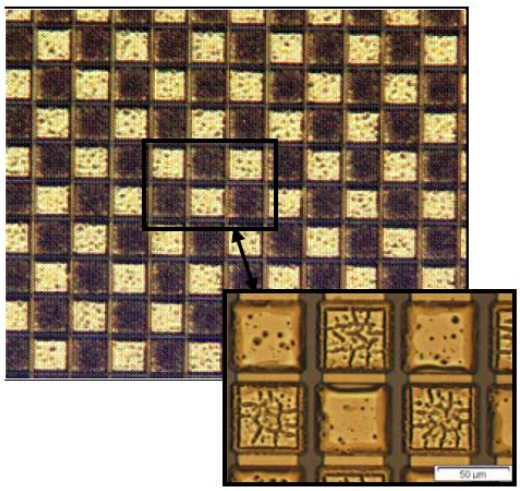

Figure 1.9. Bismuth and antimony legs of 3-D vertical thermoelectric generator fabricated with PVD are shown [13].

1.2 Thermoelectric Energy Conversion in Mobile Systems

As the power dissipation of desktop and notebook computers, smart phones, PDA's and other mobile systems increase, power management emerges to be an important issue. With the developing technology, especially electrical power supplied to processors increase. Most of the electrical power supplied in a mobile system is converted to waste heat, which contributes to inefficiency where energy efficiency is considered. The waste heat or some portion of it can be converted to electrical energy in a reversible way to power some of the components in mobile systems. For industrial applications, systems utilizing Brayton cycle or Carnot cycle are relatively efficient converting heat into electricity. However, the space is limited and there is a need for a quiet and a cheap solution for power generation in mobile systems. Thermoelectric energy harvesting fits to this case in terms of scalability, easy fabrication, robustness and quiet operation. In order to analyze the feasibility of thermoelectric energy harvesting in mobile systems, it is important to understand the thermal characteristics of these systems. The locations where most heat is generated, the overall temperature distribution, the location and thermal characteristics of the fans and heat sinks are all major considerations for evaluating the applicability of thermoelectric energy conversion in these systems. All these thermal considerations combined together make up the term 'thermal management'. Once the thermal characterization of a system is correctly made, the locations applicable for thermoelectric power conversion and conversion efficiency in these locations can be properly analyzed. Thermal and power management in mobile systems are the most commonly discussed issues in recent years. Thermal management is related with designing systems that will eliminate the excessive heating (cooling solutions). On the other hand, power management is related with decreasing the power needs for the operation of the system by system architecture, electronic or mechanical design or energy conversion. It is important to note that these two terms: thermal and power management are interrelated to each other. A cooling solution also needs to be power efficient to reduce the energy invested in the operation of these systems. The challenges in thermal design in mobile systems are clearly pointed out in [15]. Non-uniform and increasing heat generation of the components is one of the major concerns discussed in this study. Energy efficient cooling and decreasing volume

issue were further studied in [16]. For the thermal design, an approach towards lowering the energy expenditure has been conducted. In the thermal design methodology developed for a notebook computer, the system was analyzed by two parts: the base-box section and LCD display section. The heat dissipation from the base-box section of a notebook computer is expressed by Equation (1.1) [16].

$$Q_s = \sum_{i=1}^{6} h_i A_i \left(T_{face} - T_{ambient}\right) + \sum_{i=1}^{6} A_i \varepsilon_i \sigma \left(T_{face}^4 - T_{ambient}^4\right) \tag{1.1}$$

Considering this equation, the passive cooling limit on laptop computers has been investigated. The experimental work depicting the cooling limit on a variety of computers are shown in Figure 1.10.

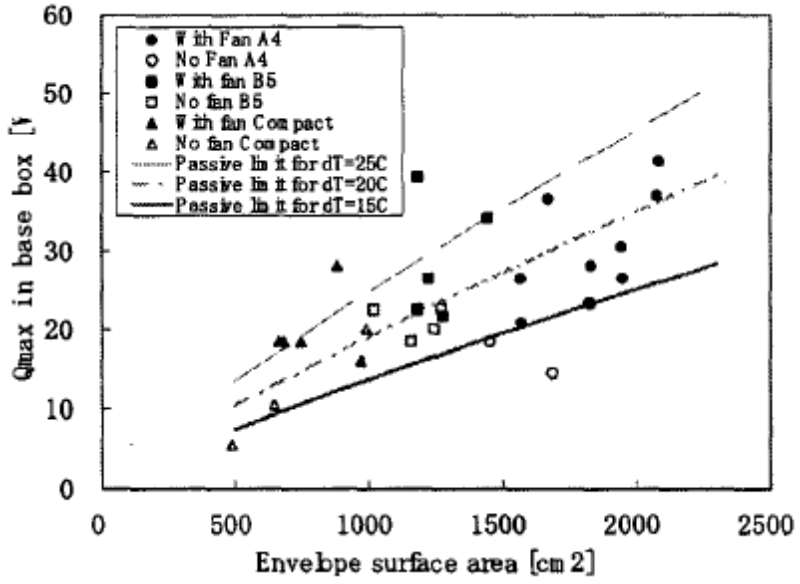

Figure 1.10. Passive and active cooling heat dissipation limits from a notebook CPU [16].

It can be seen that passive cooling (natural air convection) limits can provide sufficient heat dissipation to a degree. Forced convection can be used to extend the heat dissipation limits, but this will also add to the electrical power needed for the system. Using the reference data, an optimized thermal network and compact fan

with minimum pumping power requirement was proposed to decrease the energy needed to run the system.

In another study, a thermal management method utilizing scaling of CPU working frequency and voltage to reduce the electrical power delivered was presented [17]. A power management architecture was designed in order to reduce the voltage and frequency delivered to the CPU on the start of an application. It was claimed that this method provides %50 power consumption compromising performance by %20. The algorithm performed by the architecture is shown in Figure 1.11.

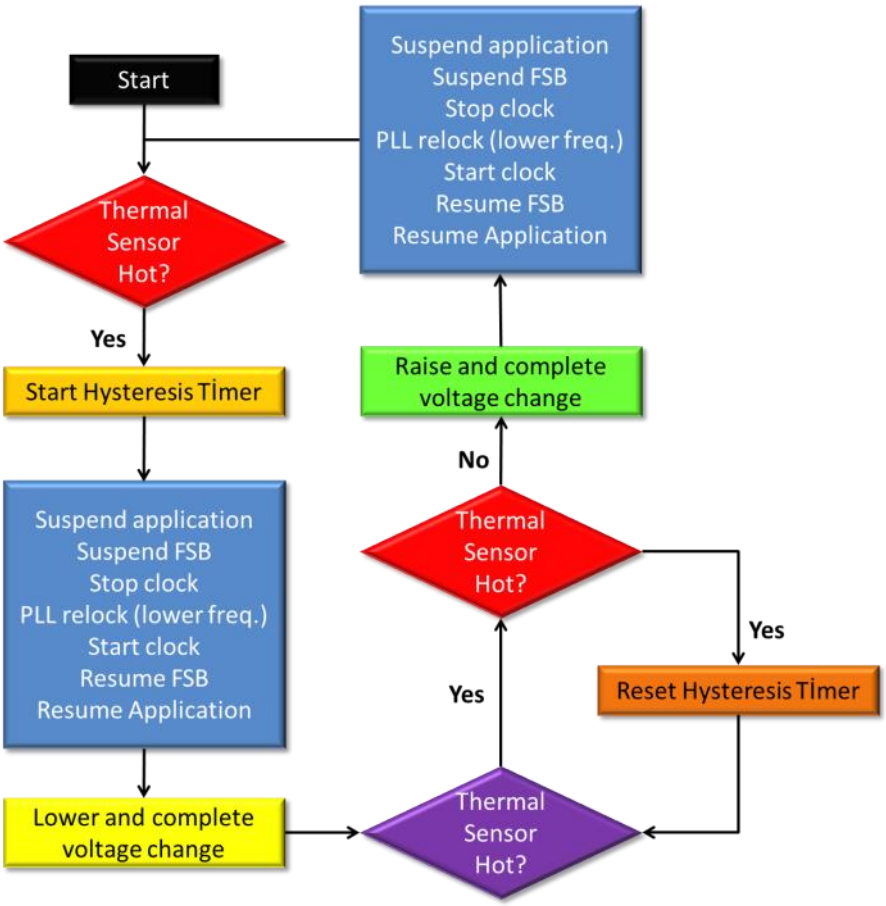

Figure 1.11. The thermal management algorithm used to reduce the power requirements of a CPU [17].

It was pointed out in [18] that thermal management issue plays an important role for the performance and reliability in IC technology. It was then predicted that the heat generation of microelectronic modules would increase greatly and radical cooling

solutions or developing the thermal packaging technology was needed to meet the market requirements. Energy optimization for cooling solutions (plate fin heat sinks, fans etc.) is also important to meet the cost requirements. Sometimes the energy invested for cooling can exceed the optimum limit for a particular system, increasing the cost. In [19], the energy optimization is made by maximizing the thermal energy extracted from available space while trying to reduce the material and energy consumed in fabrication plate fin heat sinks. Figure 1.12 shows the least energy optimization for a plate fin heat sink with varying properties.

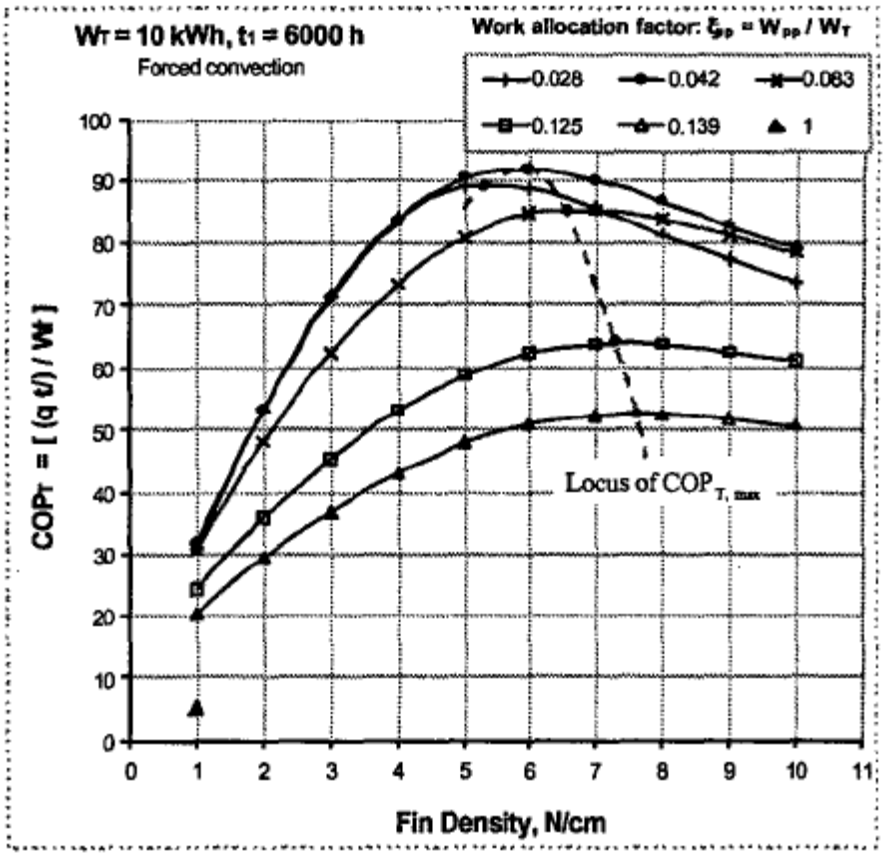

Figure 1.12. Least energy optimization for cooling of CPU with plate fin heat sinks [19].

The use of thermoelectric cooling for electronic equipment was investigated in [20], [21]. However, applying thermoelectric refrigeration in mobile systems requires relatively high currents and additional energy input into the system. Thermal management in portable mobile systems by utilizing thermoelectric conversion was first discussed in detail in [22]. It was also specified in this study that energy

harnessing from microprocessor waste heat was first proposed by Suski [23] in a patent by directly attaching the TE module to the microprocessor. In Solbrekken's paper, shunt attach configuration was proposed for energy harnessing from waste heat in high end microprocessors. In this configuration, excessive heating of the CPU was prevented by providing an alternate heat path in the system. With thermoelectric energy generators in shunt attach design, it was also possible to drive a cooling fan. The shunt heat path is formed by using a heat spreader providing an alternate heat flow path from the CPU and controlling the heat flow through the TE generator. The shunt configuration is shown in Figure 1.13 [22].

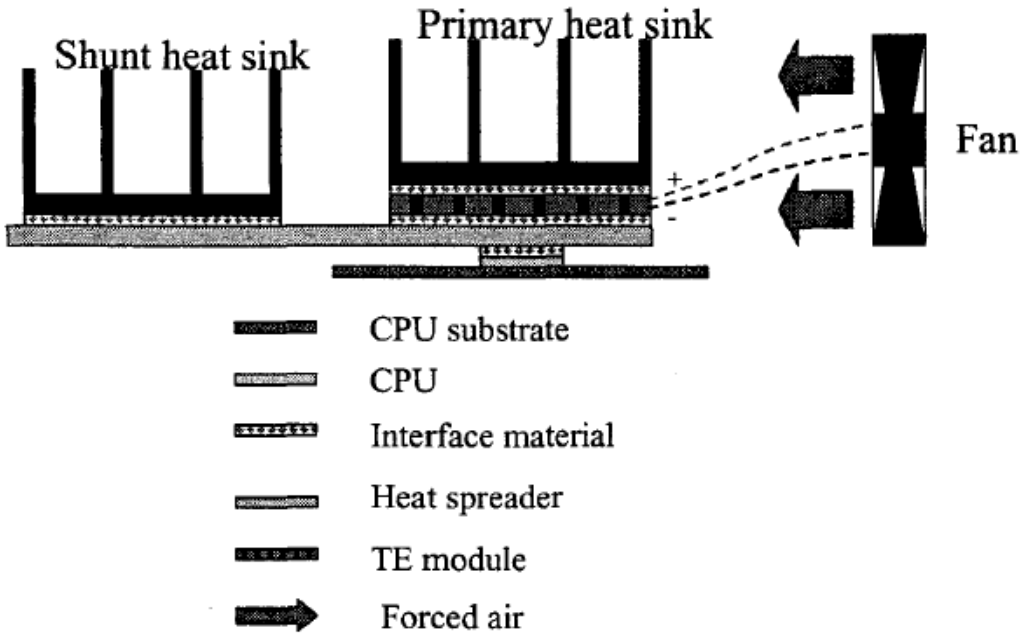

Figure 1.13. The shunt attach configuration for TE energy harvesting from waste heat generated in microprocessors [22].

Many parametric studies have been conducted to observe the thermoelectric power generation in a shunt configuration. Keeping the hot junction temperature fixed at 85°C, the power generated by TE modules with varying heat dissipation is seen in Figure 1.14 [22].

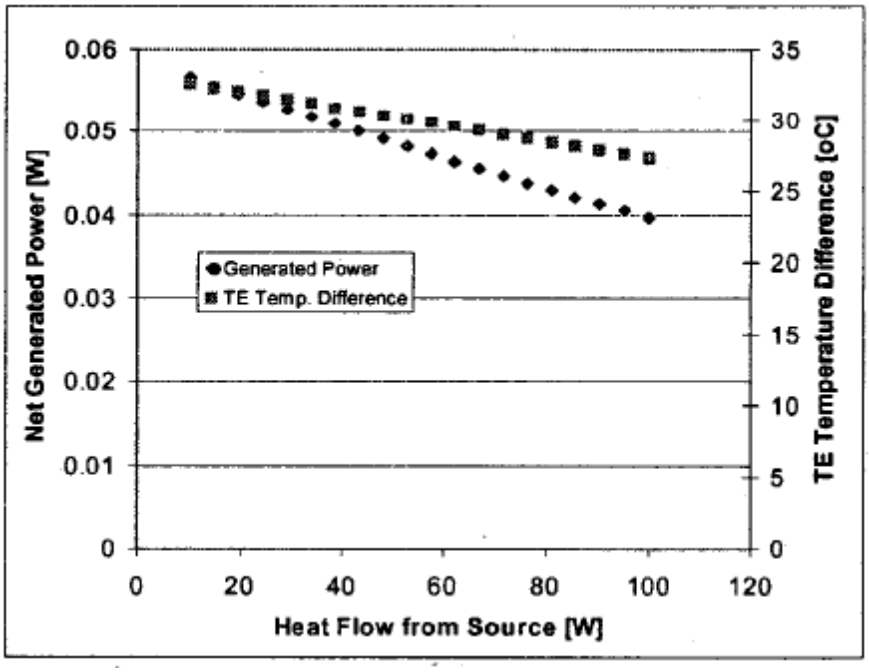

Figure 1.14. The energy generated with TE generator with varying heat flow from the microprocessor. Because the junction is forced to be kept at 85°C, the temperature drop between in the CPU-heat spreader interface increases. This decreases the TE generator performance as the heat generation increases [22].

At this point, thermoelectric energy conversion proved to be an efficient way for harvesting waste heat also in mobile systems, capable of generating over 40 mW over a processor package area of 25cm^2. It was also shown in Solbrekken's work that heat driven cooling for a microprocessor is possible.

1.3 Feasibility of Energy Harvesting in a Mobile System

For the feasibility of energy harvesting from waste heat on a processor, thermal profiling of the region is made. A basic thermal model of the CPU and the space around it where energy harvesting will be utilized is constructed using a finite element model. It is assumed that a maximum area of 100 cm^2 can be used by a heat spreader and thermoelectric energy harvesters placed on this area. The hot junction and cold junction temperature profile around the CPU region is shown in Figure 1.15 and Figure 1.16.

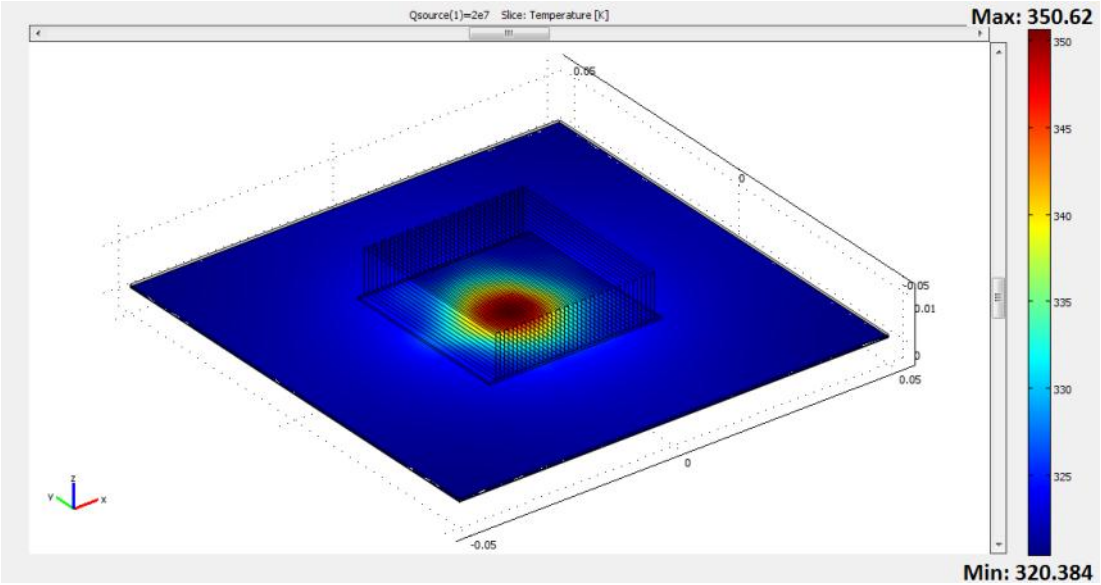

Figure 1.15. Temperature profile on a high-end CPU.

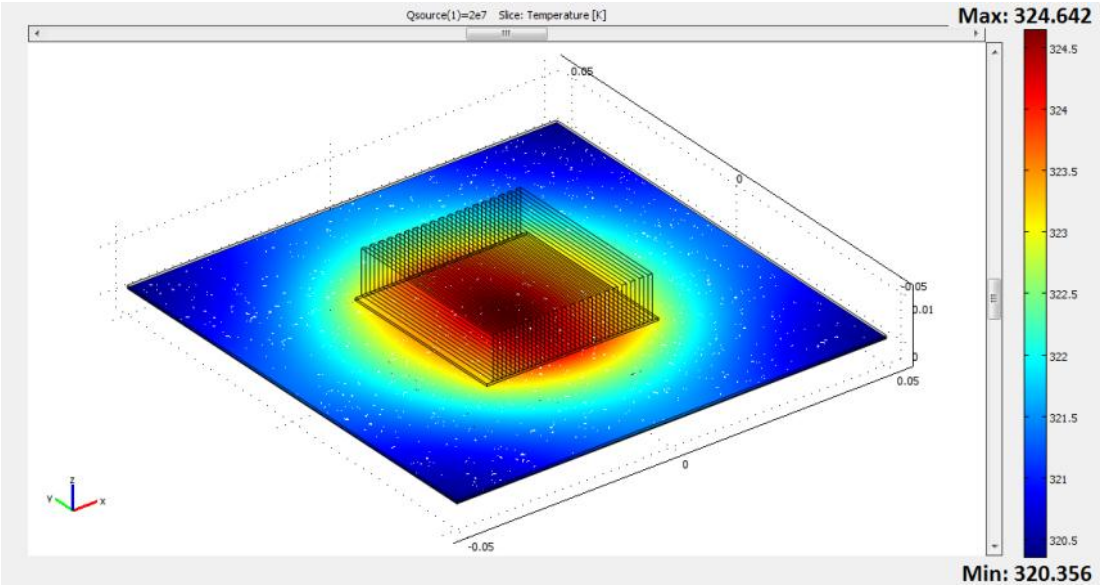

Figure 1.16. Temperature profile on the heat spreader (cold junction) of the CPU region.

In this model, air cooling by a fan at a flow rate of 0.1m/s was assumed. It can be concluded from the figure that hot junction temperature decreases as the distance from CPU core increases. This results from thermal conduction and forced convection from the heat spreader material. When the CPU temperature is around 75 °C, there is a ΔT value of 25 °C that can be applied to the MEMS TE energy

generator within the CPU area of $1cm^2$. As the distance reaches to the edges of the heat spreader, the ΔT decreases to ~0.1 °C. The performance results for a possible implementation of MEMS TE Harvesters are given in Chapter 3.

1.4 Motivation of the Research

There are many thermoelectric generator designs reported in literature, but almost none of them are designed for a specific application. The TE generators harnessing waste heat are often bulky and need large volumes for implementation. The feasibility of TE harvesting on mobile systems was done, but no commercial solution or product has been offered for this application. On the other hand, the available thermoelectric generators utilize materials that need high temperature fabrication procedures that render them unsuitable with standard MEMS fabrication methods. At this stage, the primary aim of this work is to develop MEMS thermoelectric energy harvesters for energy generation from waste heat in mobile systems (notebooks, netbooks, PDA's, smart phones etc.). The MEMS TE energy harvester proposed in this study:

- Uses materials and fabrication procedures totally available in MEMS technology
- Occupies a small volume and height for implementation in mobile systems
- Is suitable for merging with vibration energy harvesting to realize multi-mode energy harvesting.

For the development of MEMS TE energy harvesters proposed in this work,

- The design
- Analytical and finite element simulations
- Performance optimization
- Fabrication
- Performance testing
- Correlation of test and simulation results

of these MEMS thermoelectric energy harvesters have been done. The contribution of this work includes but not limited to:

- A design methodology that can be applied to lateral MEMS TE energy harvester structures for any thermoelectric material.
- The fabrication process for MEMS TE energy harvesters. The fabrication can be improved to produce TE energy harvesters in which state-of-the art materials can be used. The problems in fabrication are analyzed systematically to cumulate a background, which can be benefited later on to improve the reliability of the fabrication.
- The testing of MEMS TE energy harvesters. The correlation of the test results with the simulations. An insight to miscorrelation factors that affect the performance of the thermoelectric energy harvesters.
- An initiation for the design of vertical TE energy harvesters, which will enable more power generation in the same area (~1000 times). A simulation methodology that can be applied to any vertical TE geometry and configuration. A possible fabrication flow that can be evaluated for future work.

1.5 Thesis Outline

There are totally 7 chapters in this thesis. First chapter is the introduction to thermoelectric energy harvesting and some examples in literature.

Second chapter covers the theory behind thermoelectric conversion phenomena, and the common concepts used in thermoelectric energy conversion.

In the third chapter, modeling, design and computer simulations of MEMS TE energy harvesters are explained in detail.

Fourth chapter covers the fabrication flow of the thermoelectric energy harvesters. All microfabrication details and intermediate steps are explained and shown by tables and figures.

The test results of MEMS TE energy harvesters are presented in the fifth chapter.

The sixth chapter is the conclusion and future work for this thesis.

CHAPTER 2

THEORY AND MODELING OF THERMOELECTRIC ENERGY CONVERSION

This chapter introduces the basic theory and modeling of thermoelectric energy conversion. In Section 2.1, the theory behind Seebeck effect is explained. In Section 2.2, the physical properties of thermoelectric materials and the effect on the design is discussed. In section 2.3, the performance parameters and design criteria of a thermoelectric generator are discussed in detail. Finally, Section 2.4 summarizes the chapter.

2.1 Thermoelectric Energy Harvesting

Thermoelectric generation is used to convert heat (mostly waste heat) into electricity utilizing the Seebeck effect. Once a temperature difference is created between the two ends of a conductor/semiconductor material, an electric potential is created within that material with the motion of the charge carriers. Although there are other thermoelectric effects like Peltier and Thomson effects, the major physical phenomenon responsible for voltage generation is the Seebeck effect. All of these thermoelectric effects are discussed in next sections.

2.1.1 Seebeck Effect

The Seebeck effect occurs when two thermoelectric materials are combined to form a junction, and a temperature difference is supplied between the junction and open ends. The thermocouple structure is shown in Figure 2.1.

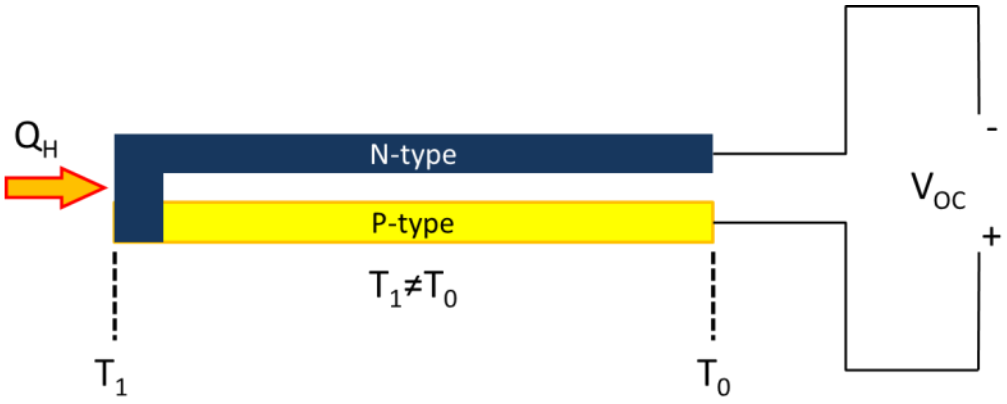

Figure 2.1. The thermocouple structure. V_{OC} is the open circuit voltage generated by Seebeck effect.

When a temperature difference is applied at the two ends of a thermoelectric material, there is a net transfer of majority charge carriers in that material. A diffusion of charge carriers occurs in a thermoelectric material. Hot carriers diffuse from the hot end to the cold end of the thermoelectric material due to a lower density of hot carriers at the cold junction. The charge carrier motion occurs to reach thermodynamic equilibrium. As these charge carriers move, also an electric current occurs through the thermoelectric material. This phenomenon is called the Seebeck effect and was discovered by T. J. Seebeck (1770-1831) in 1821.

In a p-type material the majority charge carriers (holes) diffuse from the hot and to cold end. Likewise, electrons in an n-type thermoelectric material diffuse from the hot end to the cold end. If these p and n-type materials were to form a thermocouple, the electric current will flow from the cold junction of the n-type material to cold junction of p-type material. The direction of electric current flow in a thermoelectric generator is shown in Figure 2.2.

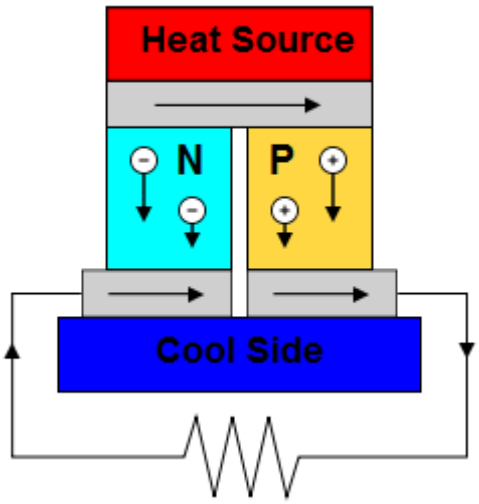

Figure 2.2. Current flow in a simple thermoelectric generator.

The Seebeck voltage depends on the characteristics of the thermoelectric material used and the temperature difference between the hot and cold junctions. The formula used for calculating the Seebeck voltage is shown by Equation (2.1).

$$V_{oc} = n \cdot \alpha_{AB} \cdot (T_H - T_C) \tag{2.1}$$

Where n is the number of thermocouples used, α_{AB} is the relative Seebeck coefficient of the materials $(\alpha_A - \alpha_B)$ A and B, T_H and T_C are the absolute value of hot and cold junctions, respectively.

The Seebeck coefficient for thermoelectric materials (semiconductor or metal) is directly related to the asymmetry in the distribution of electrons around the Fermi level when a temperature gradient is applied between the ends of that material. Figure 2.3 shows the energy band diagram of a p-type crystalline semiconductor material [24]. For p-type thermoelectric materials, the majority charge carriers transport from the hot end to the cold end as they are more energetic. This motion continues until a thermodynamic equilibrium is reached through the material. As the holes diffuse from the hot end to the cold end, the cold end is more positive relative to the hot end. Thus, a voltage builds up in the material. This is how the phenomenon occurs for a p-type thermoelectric material. On the other hand, the electrons move from the hot end to the cold end for an n-type thermoelectric material. Thus, the

Seebeck coefficient is negative. The magnitude of the Seebeck coefficient depends on the mobility and mean free path of the charge carriers of the thermoelectric material.

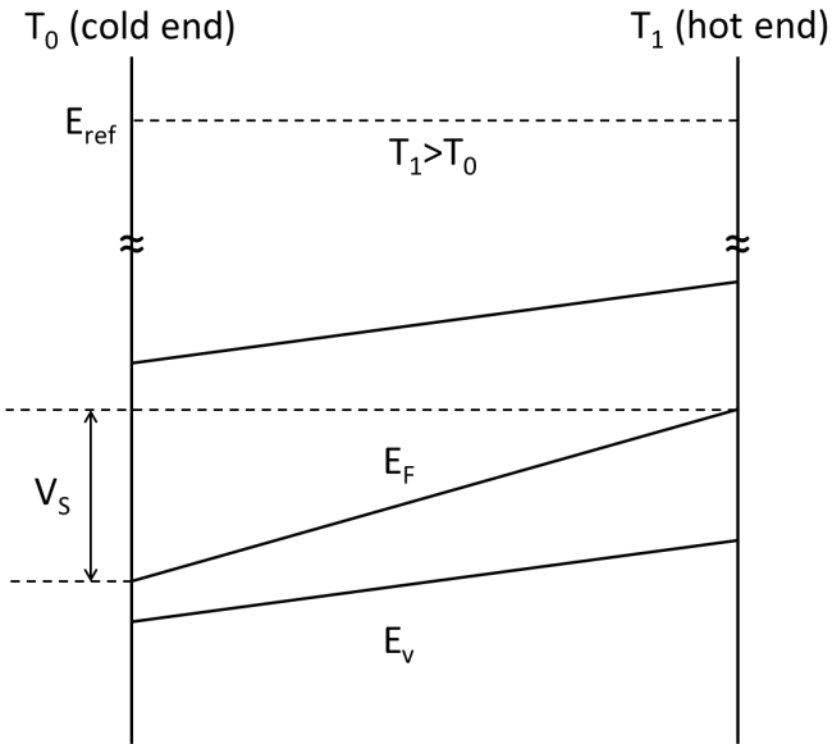

Figure 2.3. The energy band diagram for a p-type crystalline silicon substrate. One end of the semiconductor is kept at temperature T_1 and the other end is at temperature T_0. V_s, is the Seebeck voltage generated between the hot and cold ends of the semiconductor.

2.1.2 Peltier Effect

Peltier effect occurs at a junction of two different thermoelectric materials when a current passes through the junction. Figure 2.4 represents the Peltier effect.

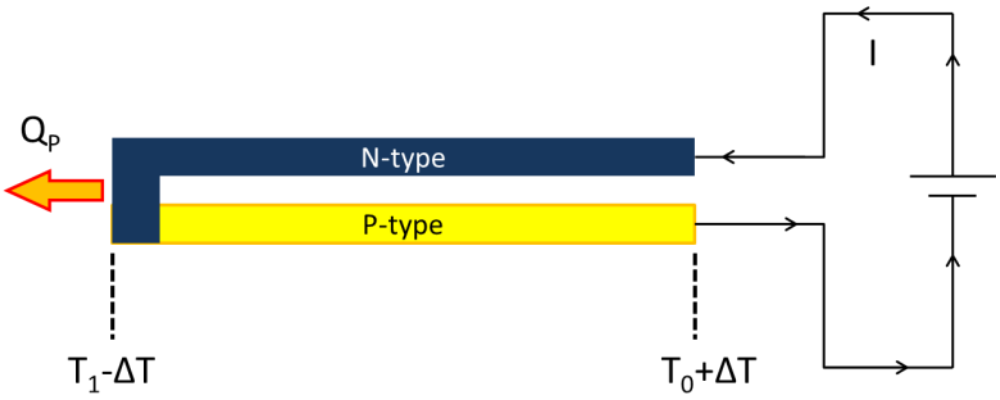

Figure 2.4. The Peltier effect; heat is either absorbed from or released to ambient at the junction depending on the current direction.

Referring to Figure 2.4, when a specific amount of electrical current 'I' flows through a junction constructed from two different materials, a specific amount of heat is released to or absorbed from the ambient depending on the direction of the current. The amount of heat, which is called the 'Peltier Heat' and denoted as 'Q_p', is calculated as follows:

$$Q_p = \pi_{AB} \cdot T \cdot I \tag{2.2}$$

Here, T is the temperature of the junction shown in Figure 2.4, I is the electrical current, and π_{AB} is the relative Peltier coefficient. The Peltier coefficient is related with the relative Seebeck coefficient α_{AB} as follows:

$$\pi_{AB} = \alpha_{AB} \cdot T \tag{2.3}$$

The Peltier effect is not the dominant effect in thermoelectric energy generation.

2.1.3 Thomson Effect

The Thomson effect occurs when a temperature difference is provided along a thermoelectric material while an amount of electrical current flows through. Consider the system in Figure 2.5.

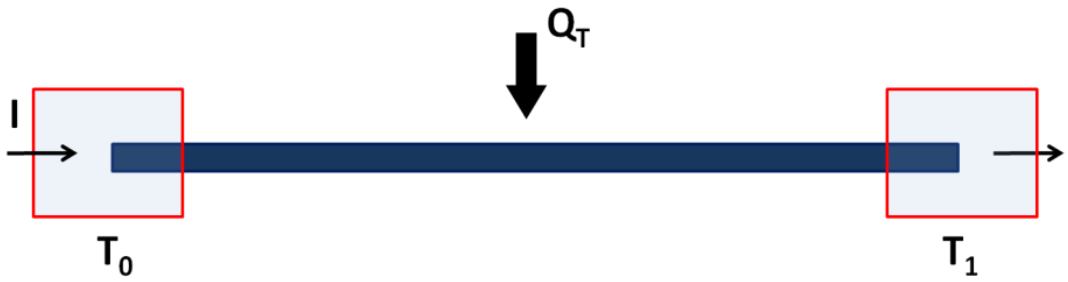

Figure 2.5. The Thomson effect; heat is either released to or absorbed from the ambient depending on the current and temperature gradient direction.

For a conductor with a temperature difference, T_1-T_0, across its ends as shown in Figure 2.5, a specific amount of heat is released to or absorbed from the ambient. The absorption or release of the heat depends on the direction of the current and the temperature gradient. The amount of heat is called the 'Thomson heat', denoted as Q_T, and is calculated as follows:

$$Q_T = \int_{T_0}^{T_1} \tau(T) \cdot I \cdot dT \tag{2.4}$$

Here T is the temperature, I is the current, and $\tau(T)$ is the Thomson coefficient of the conductor. $\tau(T)$ is related with the Seebeck coefficient α of the conductor as follows:

$$\tau(T) = T \cdot \frac{d\alpha(T)}{dT} \tag{2.5}$$

2.2 Thermopile Materials

As thermoelectric materials, there is a wide range of possibilities through semiconductors and metals. Semiconductors mostly have high Seebeck coefficient and lower thermal conductivity. Compounds of Bismuth and Telluride are widely used for high thermoelectric voltages. However, fabrication of these materials on chip scale requires an elaborate process technology. Here, we present a proof of

concept thermoelectric generator design utilizing metals with high thermopower (Cr and Ni). Once the performance of the designs is verified, other thermoelectric materials can be used for higher performance. Thermopower ($S^2\alpha$) of a material is as important as the Seebeck coefficient. It is the multiplication of the Seebeck coefficient square with the electrical conductivity. Cr and Ni are easily processable materials in MEMS fabrication, and they have a relatively higher thermopower than other metals. For a higher thermoelectric voltage, the thermal conductivity should also be as low as possible to obtain a good temperature gradient through the material. The calculation of the Seebeck coefficient and the effect of thermal conductivity on the thermoelectric performance are discussed in the following sections.

2.2.1 Seebeck Coefficient (α) and Thermal Conductivity (κ)

The Seebeck effect originates from the temperature dependence of the Fermi level of the charge carriers through the material. Thus, Seebeck coefficient of a thermoelectric material can be expressed as the ratio of the change in the Fermi level (ΔE_F) to the change in temperature (ΔT), i.e.,

$$\frac{\Delta E_F}{\Delta T} = \alpha \cdot q \tag{2.6}$$

or,

$$\alpha = \frac{1}{q} \cdot \frac{\Delta E_F}{\Delta T} \tag{2.7}$$

Here, α is the Seebeck coefficient of the material, and q is the electronic charge constant, which is equal to 1.6 x 10^{-19} C.

Suppose that some amount of ΔT is applied between the open ends of an n-type thermoelectric material (e.g. aluminum). The majority charge carriers (electrons in our case) will move from more energetic side (hot side) to the low energy state (cold side). The average energy of an electron in a metal is expressed by Equation (2.8) [25].

$$E_{av}(T) = \frac{3}{5} E_{FO} \left[1 + \frac{5\pi^2}{12} \left(\frac{kT}{E_{FO}} \right)^2 \right] \quad (2.8)$$

Here E_{FO} is the Fermi energy at 0 K, k is the Boltzmann constant, and T is the absolute temperature in K. It can be depicted from Equation (2.8) that the average energy at the hotter end is greater. As the diffusion of the high energy electrons occur from the hot and to the cold end, a potential ΔV is generated which prevents further electron motion to the cold side.

The Seebeck coefficient of a metal can be fundamentally calculated by constituting an energy equilibrium state in a finite length δx in the material. Assume that a voltage difference δV is created in this finite length by a finite amount of temperature difference δT. One electron diffusing from the hot end to the cold end does work against the potential difference δV. The amount of work is $-e\delta V$. Writing the energy equilibrium:

$$-e\delta V = E_{av}(T + \delta T) - E_{av}(T) \quad (2.9)$$

Substituting Equation (2.9) into (2.8), and omitting the δT^2 term we get:

$$-e\delta V \approx \frac{\pi^2 k^2 T \delta T}{2E_{FO}} \quad (2.10)$$

Where k is the Boltzmann's constatnt, and T is the absolute temperature.

Since the Seebeck coefficient $S = {}^{\delta V}/_{\delta T}$, it can also be expressed as:

$$S \approx -\frac{\pi^2 k^2 T}{2eE_{FO}} \quad (2.11)$$

Let's take Cu as our thermoelectric material. $E_{FO} = 7.0\, eV$ for copper. At $T = 300\, K$ the Seebeck coefficient for copper is calculated as 1.57 μV/K. This value is consistent with 1.7 μV/K, reported in [25].

It is important to count for the scattering of the electron to decide the sign of the Seebeck coefficient. The free electron theory is insufficient for the determination of the Seebeck coefficient. The brief derivation of electron flux is made in [25]. Considering the scattering process, Mott and Jones derived the fundamental formula for an electron:

$$S \approx -\frac{\pi^2 k^2 T}{3eE_{FO}} x \tag{2.12}$$

Where x is a constant determined by the charge transport characteristics of the material. However, (2.12) does not apply to transition metals as the band structure is different.

In non-degenerately doped (not very highly doped) semiconductors, there are mainly three physical effects that contribute to the Seebeck coefficient. These are the temperature dependence of the Fermi level, the velocity of the charge carriers due to temperature, and phonon drag induced by the temperature gradient. These effects are discussed in detail in [26], [27]. Note that, at higher doping concentrations Fermi-Dirac statistics is executed to calculate the phonon drag in a semiconductor. Taking all the physical effects of thermoelectricity, the Seebeck coefficients for an n-type and p-type semiconductor are calculated by Equations (2.13) and (2.14).

$$\alpha_n = -\frac{k}{q} \cdot \left[ln\left(\frac{N_c}{n}\right) + \frac{5}{2} + S_n + \phi_n \right] \tag{2.13}$$

$$\alpha_p = +\frac{k}{q} \cdot \left[ln\left(\frac{N_v}{p}\right) + \frac{5}{2} + S_p + \phi_p \right] \tag{2.14}$$

Here, k: Boltzmann's constant

q: Electronic charge constant (1.6 x 10^{-19} C)

n and p: Doping level of n and p type semiconductor

N_c: Conduction band density of states

N_v: Valence band density of states

S_n and S_p: a parameter that interrelates the relaxation time and the energy of a charge carrier

ϕ_n and ϕ_p: phonon drag effect in Fermi-Dirac statistics

From Equations (2.13) and (2.14), a thermopile structure made of n-silicon/p-silicon thermocouples will result in a higher Seebeck voltage at the open ends of the thermopile, since the Seebeck coefficients of the n and p-type silicon materials are opposite in sign. This type of a thermocouple will have a relative Seebeck coefficient, $\alpha_p - \alpha_n$, which is much larger than the Seebeck coefficient of a thermocouple whose leads are both doped either n- or p-type.

(2.13) and (2.14) can be reduced to a simpler form for the range of operation of the thermopile. Here, the approximation that is evaluated by Sarro for the operation at room temperature (300 K) is be given in Equation (2.15) [28]. This formula is also used in the experimental calculations.

$$\alpha = \frac{m \cdot k}{q} \cdot ln\left(\rho/\rho_0\right) \tag{2.15}$$

Here, "m" is a constant which is about 2.6, $\rho_0 = 5x10^{-6}$ Ω.m, and ρ is the electrical resistivity of the non-degenerately doped semiconductor.

Thermal conductivity (κ) is another major parameter that determines the overall performance of a thermoelectric generator. Recalling Equation (2.1), the Seebeck voltage obtained at the open ends of a thermocouple structure depends not only on α_{AB}, i.e., the relative Seebeck coefficient of the material "A" to "B" used in the thermocouple, but also on ΔT, the temperature difference between the hot and cold ends of the thermocouple. κ on the heat flow path directly affects ΔT. ΔT is high for the materials with low κ values. For a better understanding of the concept, consider the situation shown in Figure 2.6.

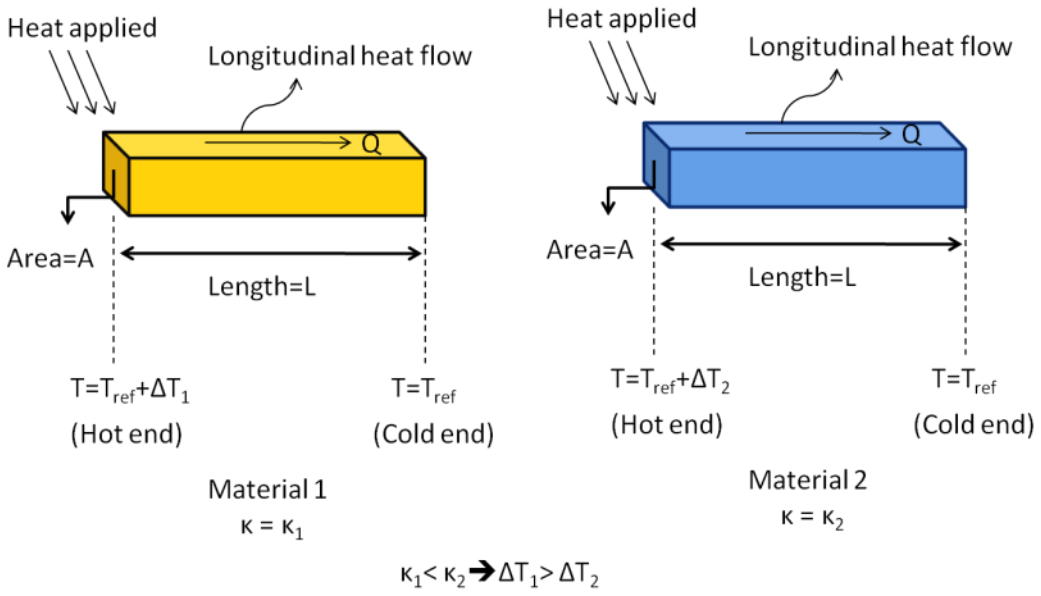

Figure 2.6. Two equally sized different materials. Same amount of heat is applied from the left sides, thus same amount of heat flow "Q" is provided for both.

Two different materials with legths "L" and cross-sectional areas "A" are heated with the same amount of heat from their left sides as shown in Figure 2.6. The heating causes a longitudinal heat flow, which is denoted by "Q", in both materials. This will lead to a temperature difference ΔT_1 and ΔT_2 between the hot and cold ends of the materials 1 and 2, respectively. Considering the electrical current, "I", flowing through a resistor as the counterpart of the heat flow "Q", and the voltage difference "V", obtained across the terminals of the resistor as the counterpart of the temperature difference ΔT, we have:

$$\Delta T = Q \cdot \frac{L}{A \cdot \kappa} \tag{2.16}$$

From Ohm's law, we know that "V/I=R", where "R" is the electrical resistance. Similar approach is applicable for the materials in Figure 2.6, yielding in a thermal resistance that is derived as follows:

$$\frac{\Delta T}{Q} = \frac{1}{\kappa} \cdot \frac{L}{A} \tag{2.17}$$

From Equation (2.17), it can be seen that ρ, the electrical resistivity is the counterpart of $1/\kappa$, the reciprocal of thermal conductivity. In other words, σ, the electrical conductivity, is the counterpart of the thermal conductivity, κ. lists the electrical equivalents for the thermal quantities.

Table 2.1. Electrical counterparts of the thermal properties

Definition	Thermal Quantity	Electrical Quantity	Definition
Temperature (K)	T	V	Voltage (V)
Heat Flow (W)	Q	I	Electrical current (A)
Thermal conductivity (W/m.K)	λ	σ	Electrical conductivity (S/m)
Thermal resistivity (m.K/W)	$1/\lambda$	ρ	Electrical resistivity (Ω.m)

For a high Seebeck voltage at the open ends of a thermocouple, ΔT should be as high as possible. This can be provided by using materials with lower thermal conductivities, which is also obvious from Equation (2.16). Evaluating the problem in heat transfer point of view, material on the left which has a lower κ in Figure Figure 2.6 is more preferable than the one on the right as the thermoelectric material. Apart from κ, Seebeck coefficient of the materials used, thermoelectric figure of merit and thermoelectric power factor are the parameters that together affect the thermoelectric performance of a material. Thermopower and thermoelectric figure of merit will be explained in the next section.

2.2.2 Thermoelectric Power Factor and Thermoelectric Figure of Merit

When efficiency is of consideration, the Carnot efficiency is the limiting factor in systems utilizing heat to generate power. The Carnot efficiency is given in Equation (2.18)

$$\eta = \frac{\Delta T}{T_H} \tag{2.18}$$

Where $\Delta T = T_H - T_C$ is the temperature difference between the hot and cold junctions of the thermoelectric material. The real efficiency of a thermoelectric generator is shown in Equation .

$$\eta = \frac{\Delta T \cdot \eta_r}{T_H} \tag{2.19}$$

Where η_r is the reduced efficiency. The thermoelectric device efficiency is generally formulated as in Equation (2.20) [29].

$$\eta = \frac{P_{out}}{Q_H} = \frac{\Delta T}{T_H} \cdot \frac{\sqrt{1+ZT}-1}{\sqrt{1+ZT}+{T_C}/{T_H}} \tag{2.20}$$

Where P_{out} is the electrical power output, Q_H is the input heating power, and ZT is defined as the thermoelectric device figure of merit. In this formulation, an ideal thermoelectric generator configuration where all the heat losses, losses from electrical interconnects, thermal and electrical contact resistances are neglected. The calculation results using this formula give good correlation results with the experimental values for commercial thermoelectric modules.

Here, thermoelectric figure of merit (ZT) is an important performance parameter determined by the Seebeck coefficient of the material (α), absolute temperature (T), electrical resistivity (ρ) and thermal conductivity (k) of the material. The figure of merit is calculated as:

$$ZT = \frac{\alpha^2 T}{\rho k} \tag{2.21}$$

The figure of merit for some thermoelectric materials is shown in Figure 2.7 [30].

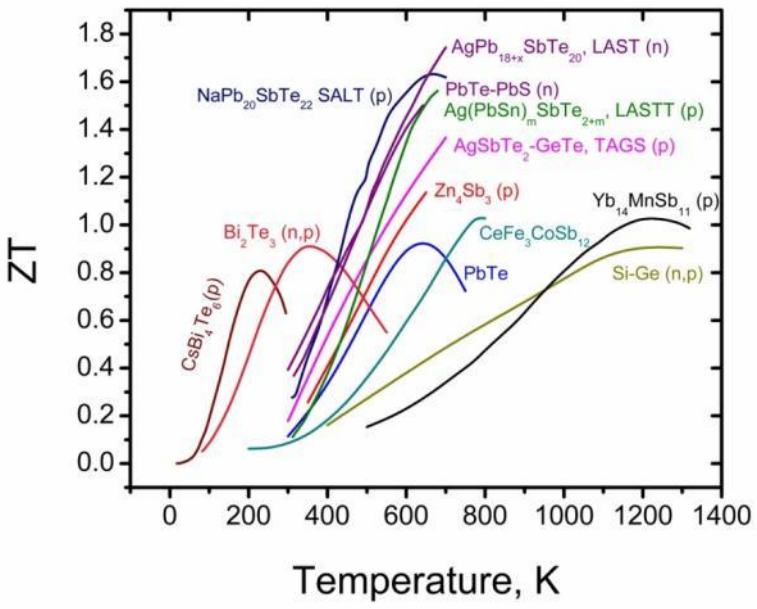

Figure 2.7. Thermoelectric figure of merit for semiconductors, semimetals and metals [30].

Equation (2.21) is valid for a single thermocouple material. The figure of merit for a thermocouple constructed with two different materials, like "A" and "B", having a relative Seebeck coefficient, α_{AB}, is defined as follows [31]:

$$z = \frac{\alpha_{AB}^2}{\left(\sqrt{\rho_A \cdot \kappa_A} + \sqrt{\rho_B \cdot \kappa_B}\right)^2} \tag{2.22}$$

Here, ρ_A: Electrical resistivity of material "A" (Ω.m)

ρ_B : Electrical resistivity of material "B" (Ω.m)

κ_A: Thermal conductivity of material "A" (W/m.K)

κ_B: Thermal conductivity of material "B" (W/m.K)

It should be noted here that it is not possible to request different doping levels and thermal conductivity values in a standard CMOS process. Rather, we can compare the different layers and choose the ones that are better to implement a thermocouple.

In another study, thermoelectric power factor is taken as the major parameter of consideration for thermoelectric refrigeration and energy generation. For common semiconductors and metals, Seebeck coefficient decreases with the increasing electrical conductivity. The cause of this behavior is explained by the nature of electronic density of states and discussed thoroughly in [32]. The thermoelectric power factor is expressed by $S^2\sigma$, where S is the Seebeck coefficient and σ is the electrical conductivity of the material. So, thermoelectric power factor is an important consideration for estimating the thermoelectric performance of conventional semiconductors and metals. Thermoelectric power factor for some materials are given in Figure 2.8 [33].

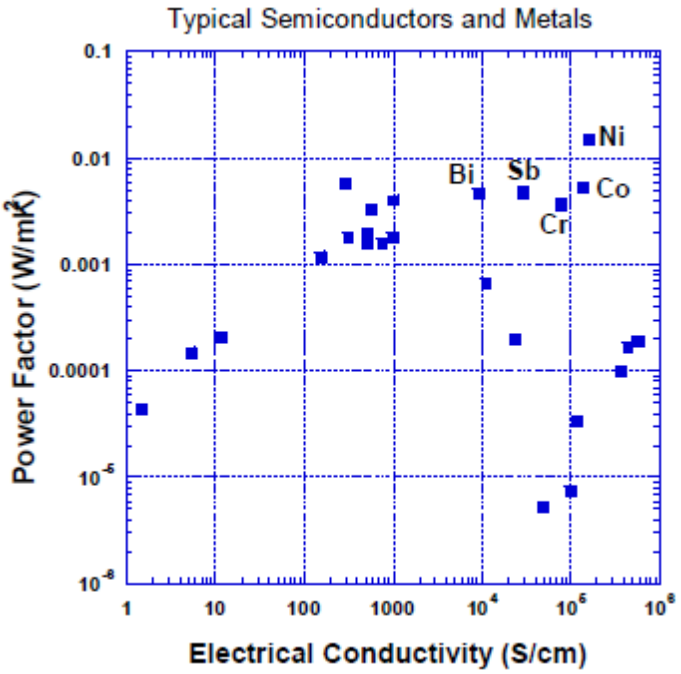

Figure 2.8. Thermoelectric power factor for some metals and semimetals [33].

Here it can be seen that Cr and Ni are the metals that have high thermoelectric power factors. In generator designs where maximum power is more important than maximum efficiency, power factor should be considered. Thus, Cr and Ni are chosen as the thermoelectric materials for the MEMS based thermoelectric energy harvesters in this study.

2.3 Performance Parameters of a Thermoelectric Generator

The performance of a thermoelectric generator is evaluated by the voltage and power level it supplies when a specified heating power is given to the generator. There are three main performance parameters for a thermopile structure: 1) Voltage generated V, 2) Power generated, P_{out}, 3) Conversion Efficiency, η, and 4) Transient response of the thermoelectric generator to heating. The following four sections explain the definitions and the formulations of these parameters, and the relations between them.

2.3.1 Generated Voltage

Generated voltage (V) gives information about the generated Seebeck voltage (V_s) at the open ends of a thermopile structure with respect to the amount of incoming heating power onto the thermopile hot junction.

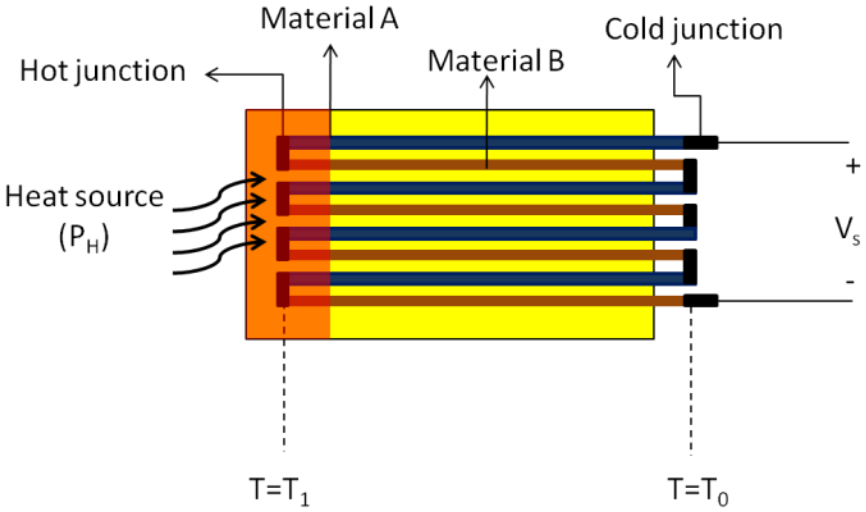

Figure 2.9. The thermopile structure with heat source on the left. A temperature difference, $\Delta T=T_1-T_0$, is generated between the hot and cold ends.

For the thermoelectric voltage calculation we have:

$$V = n\alpha\Delta T \tag{2.23}$$

For the thermopile in Figure 2.9, $V_s = N \cdot \alpha_{AB} \cdot \Delta T$, where "N" is the number of thermocouples in the thermopile, $\alpha_{AB} = \alpha_A - \alpha_B$, and $\Delta T = T_1 - T_0$. In Section

2.2.1, it was stated that ΔT can be thought as the counterpart of the electrical voltage, and "Q", the heat flow, can be thought as the counterpart of the electrical current in thermal systems. Similar approach can be applied to the thermopile structure in Figure 2.9, with a little change in heat flow notation, where "P_R" will be used instead of "Q". Defining an equivalent thermal resistance of the whole thermopile structure as $R_{th,eq}$, we obtain:

The thermal resistance of a single material was given in (2.17). The equivalent electrical network for a material with P_H applied from one end can be drawn as in Figure 2.10.

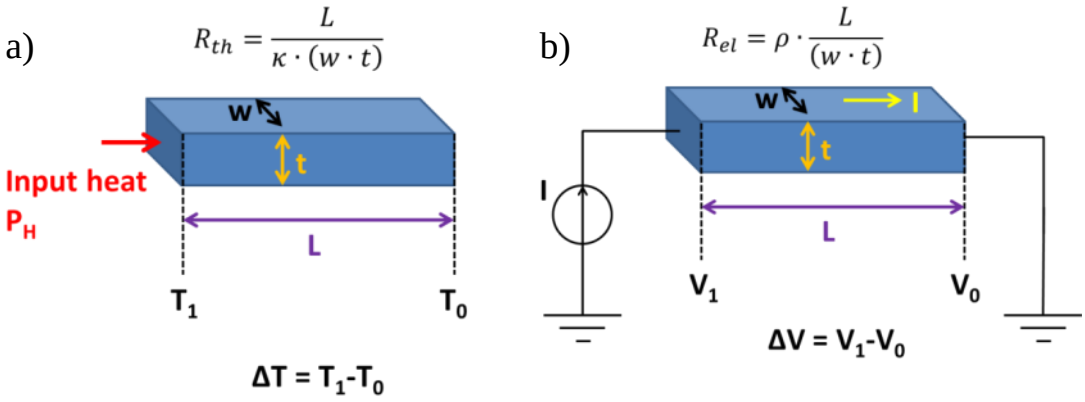

Figure 2.10. The thermal quantities for a material with heat applied from one side (a) and its electrical equivalent (b).

2.3.1.1 Thermal Resistance of Multilayer Structures

In a lateral thermoelectric energy harvester, the thermal resistance of each thin film material on the heat flow path must be taken into account for performance evaluation. Considering an electrical counterpart of the model, the thermal resistance of each layer can be considered as the parallel combination of the electrical resistances of the layers. The problem is illustrated in Figure 2.11.

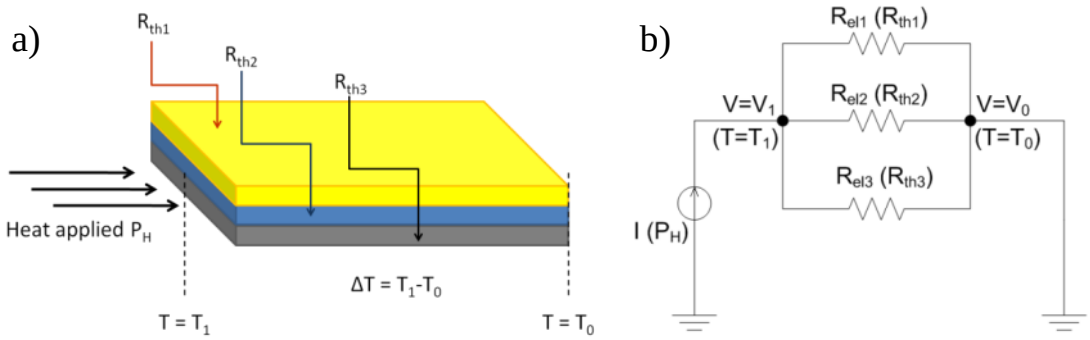

Figure 2.11. The thermal quantities for a multilayer system with heat applied from one side (a) and its electrical equivalent (b).

ΔT in Figure 2.11. (a) would be higher for the same amount of P_H, if less number of layers in the heat flow path were used. Notice the similarity in the electrical equivalent. ΔV in Figure 2.11 on the right would be higher for the same amount of current, "I", if only one or two of the resistors were connected in parallel, instead of three. Suppose that materials A and B are the materials that compose the thermocouple, and C is the insulator material carrying them. Take the number of thermocouples as N. For each of the layers, we have the following equivalent thermal resistances as shown below:

$$R_{th,A} = \frac{1}{\kappa_A} \cdot \frac{L}{w_A \cdot t_A} \cdot \frac{1}{N} \tag{2.24}$$

$$R_{th,B} = \frac{1}{\kappa_B} \cdot \frac{L}{w_B \cdot t_B} \cdot \frac{1}{N} \tag{2.25}$$

$$R_{th,C} = \frac{1}{\kappa_C} \cdot \frac{L}{w_C \cdot t_C} \tag{2.26}$$

Throughout the Equations (2.24)-(2.26), "L" is the length of the thermopile, κ_A, κ_B, and κ_C are the thermal conductivities of materials A, B and insulator C, respectively, and N is the number of thermocouples in our thermopile structure. t_A, t_B, t_C, are the thicknesses of A, B and C layers, respectively. They can be changed by varying process paramenters due to the performance requirements needed. The widths of A,

B, and C layers, w_A, w_B, w_C, respectively are chosen by the designer to satisfy a required thermal conductance value or performance parameter. Here, it is important to note that $1/N$ terms in Equations (2.24) and (2.25) are added to calculate the thermal resistance of N thermocouple structures in parallel. The more the number of thermocouples, the less the thermal resistance.

As a result, the equivalent thermal resistance ($R_{th,eq}$) of our thermopile structure is:

$$R_{th,eq} = \left(\frac{1}{R_{th,A}} + \frac{1}{R_{th,B}} + \frac{1}{R_{th,C}} \right)^{-1} \tag{2.27}$$

If metals with high thermal conductivity are chosen as thermoelectric materials, $R_{th,A}$ and $R_{th,A}$ will dominate Equation (2.27). Especially the effect of $R_{th,C}$ on the equivalent thermal resistance will be of minor importance since this value will be relatively much larger for insulator materials.

2.3.2 Generated Power

The calculation of generated voltage from a thermoelectric generator was explained in the previous section. The power obtained from a thermoelectric generator is as follows:

$$P = \frac{{V_s}^2}{2(R_{te} + R_{load})} \tag{2.28}$$

Here R_{te} is the internal thermoelectric resistance, and R_{load} is the electrical load resistance.

The load is an electrical resistance which the thermoelectric generator drives. For maximum power generation or maximum conversion efficiency, the design parameters differ. For a thermoelectric generator driving a load, the current is calculated as in Equation (2.29).

$$I = \frac{V_{OC}}{R_{total}} = \frac{N \cdot \alpha \cdot (T_H - T_C)}{R_{te} + R_{load}} \tag{2.29}$$

Where V_{OC} is the open circuit voltage, N is the number of thermocouples, α is the Seebeck coefficient, T_H and T_C are the hot and cold side temperatures, respectively.

The power generated by a thermoelectric device is shown in (2.30).

$$P_{out} = I^2 R_{load} \tag{2.30}$$

First, we take a parameter $m = {R_{load}}/{R_{te}}$. Substituting Equation (2.30) into (2.29), and using the terms related with efficiency explained in Section 2.2.2, the efficiency of a thermoelectric generator can be expressed as in Equation (2.31).

$$\eta = \eta_c \frac{m}{\frac{(m+1)^2}{ZT_H} + (m+1) - \frac{\eta_c}{2}} \tag{2.31}$$

The maximum power occurs where the thermoelectric resistance and load resistance match [34]. In this case, Equation (2.28) reduces to:

$$P = \frac{{V_s}^2}{4R_{te}} \tag{2.32}$$

When efficiency considered, the maximum efficiency occurs where the derivative of Equation (2.31) with respect to m is zero. This gives:

$$m = \frac{R_{load}}{R_{te}} = \sqrt{1 + ZT} \tag{2.33}$$

In case where efficiency is important (the heat flux is limited and the effect of heat exchangers cannot be neglected) the design should be done according to (2.33). But whenever the incoming heat is virtually unlimited, obtaining the maximum power is important. Thus, load resistance should match the internal thermopile resistance.

2.3.3 Heat Sink Effects

In thermoelectric energy harvesters, the general structure can be shown by a simple model in Figure 2.1. In most of the energy harvesters, the thermal resistance consists of the internal resistance of the thermocouples ($R_{th,TC}$) and the thermal resistance of the heat exchangers or sinks ($R_{th,HX}$). The temperature difference along the heat sink is defined in Equation (2.34).

$$\Delta T_{HX} = Q \cdot R_{th,HX} \tag{2.34}$$

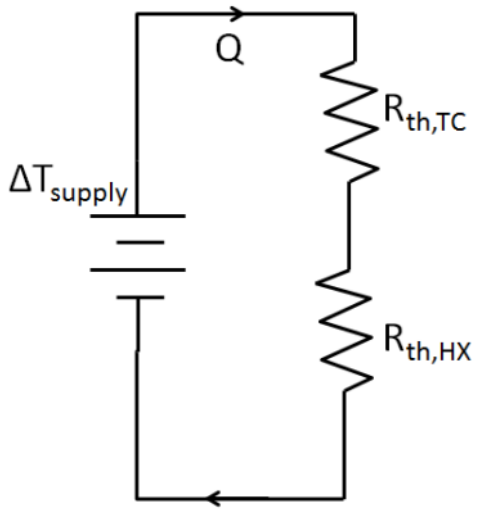

Figure 2.1. The thermal circuit of a thermoelectric energy harvester device.

In Figure 2.1, it must be noted that $R_{th,TC}$ must be optimized to obtain the maximum electrical power from the thermoelectric generator. In case where $R_{th,HX}$ dominates the thermal resistance, the temperature difference generated through the thermocouple will be minimal, resulting in very low thermoelectric voltage and power. On the other hand, if all the temperature difference is along the thermocouples, it means that $R_{th,HX} = 0$. Regarding Equation (2.34), this situation means that there is no heat flux Q through the heat exchangers, therefore no power is produced. The optimal configuration for maximum power with a fixed input heat is matched thermal resistance of thermopile and the heat sink.

2.3.4 Consideration Regarding Efficiency

The thermoelectric conversion efficiency is limited with the Carnot efficiency. However, our main concern in the design of MEMS TE energy harvesters is not maximizing efficiency. In fuel limited TE generators like pyroelectric generators, the main concern is to maximize the efficiency for economic considerations. However, the waste heat in our system is virtually unlimited. So, the main focus is to maximize the electrical power obtained in a limited area. The terms related with efficiency will be given in Section 2.2.2.

2.4 Summary of the Chapter

In this chapter the fundamental theory of thermoelectricity is explained. The physics contributing to thermoelectric effects and performance parameters were explained in detail. An overall view of the design considerations are comprehended for the initialization of the next chapter.

CHAPTER 3

DESIGN OF MEMS THERMOELECTRIC ENERGY HARVESTER

In this chapter, design, modeling and simulations of MEMS thermoelectric energy harvesters are presented. As a general understanding has been developed about thermoelectric energy conversion in the previous chapter, the analogy used for modeling will be apprehended more easily. MEMS thin film thermoelectric energy harvester utilizes the temperature difference between the hot and cold junctions along a thermopile to generate Seebeck voltage. In this chapter, a design methodology is sought to optimize the electrical power by varying the geometric properties of the materials used in the design. First, the temperature profile is analyzed for varying geometries to calculate the Seebeck voltage correctly. After this step, electrical voltage and power values are calculated. The design is made to maximize the temperature difference as well as optimizing the electrical resistance. The design points where maximum power is expected are searched by the analytical calculations. Lastly, these design parameters are summarized and comments are made on the results.

The aim of the MEMS TE energy harvesters proposed is to convert the waste heat generated in mobile systems (notebooks, netbooks etc.) to electricity by thermoelectric energy conversion. The design utilizes temperature differences along thermopiles resting on a MEMS diaphragm made of parylene C to generate electrical power. The reason for choosing this configuration is the ease of fabrication with already available metals (Cr and Ni) and possibility of integration with an electromagnetic conversion system based on a vibrating membrane carrying coils. In

this design, metal thermopiles reside on a suspended Parylene C membrane whose base is attached to a silicon rim. The thermocouples lie from the middle part of the membrane to the silicon outer rim. Significant temperature difference between the hot and cold junction can be provided due to perfect insulation characteristic of Parylene C with a thermal conductivity of 0.082 W/m.K. Here, the silicon substrate at the outer rim acts as an efficient heat sink providing heat flow to the Silicon base which is at ambient temperature and sustains the cold junction at a lower temperature. The middle part of the membrane is heated electrically for testing of the performance of the thermopile. Normally, the middle part of the membrane is planned to be thermally coupled to a heat source in a mobile system by adequate packaging to generate thermoelectric energy from waste heat. The structure of MEMS based thermoelectric energy harvester is shown in Figure 3.1.

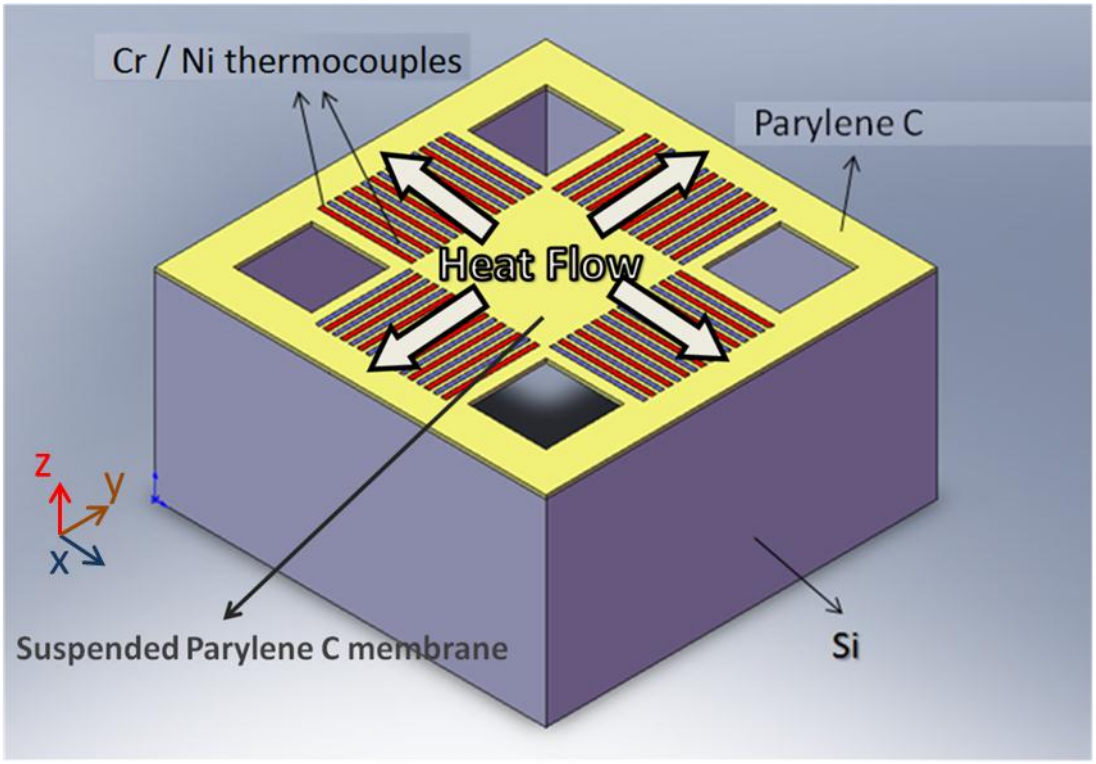

Figure 3.1. Overall structure of thin film MEMS based thermoelectric harvester.

3.1 Temperature Profile

For the performance evaluation of the thermoelectric harvester, temperature profile along the diaphragm arms is calculated for varying geometric parameters. An

analytical model is made for the calculation of the temperature profile. Later the results of this model is verified by finite element analysis in Comsol Multiphysics and a generated code in MATLAB to solve the problem in 2-D by finite difference method.

3.1.1 Calculation of Temperature Profile by Analytical Model and Finite Element Method

The temperature difference between the hot and cold junctions is one of the most important parameters that determine the overall device performance. As shown in (2.1), the voltage generated is linearly proportional to the Seebeck coefficient of the materials used and the temperature difference between the junctions. The temperature difference is directly related with the overall thermal conductance of the path of the heat flow (Equation (2.27)). The overall thermal conductance of the heat flow path is determined by the geometry, and the thermal and electrical properties of the utilized layers. Therefore, it will be most reasonable to model the temperature profile according to these layer parameters. The overall device geometry is shown in Figure 3.2.

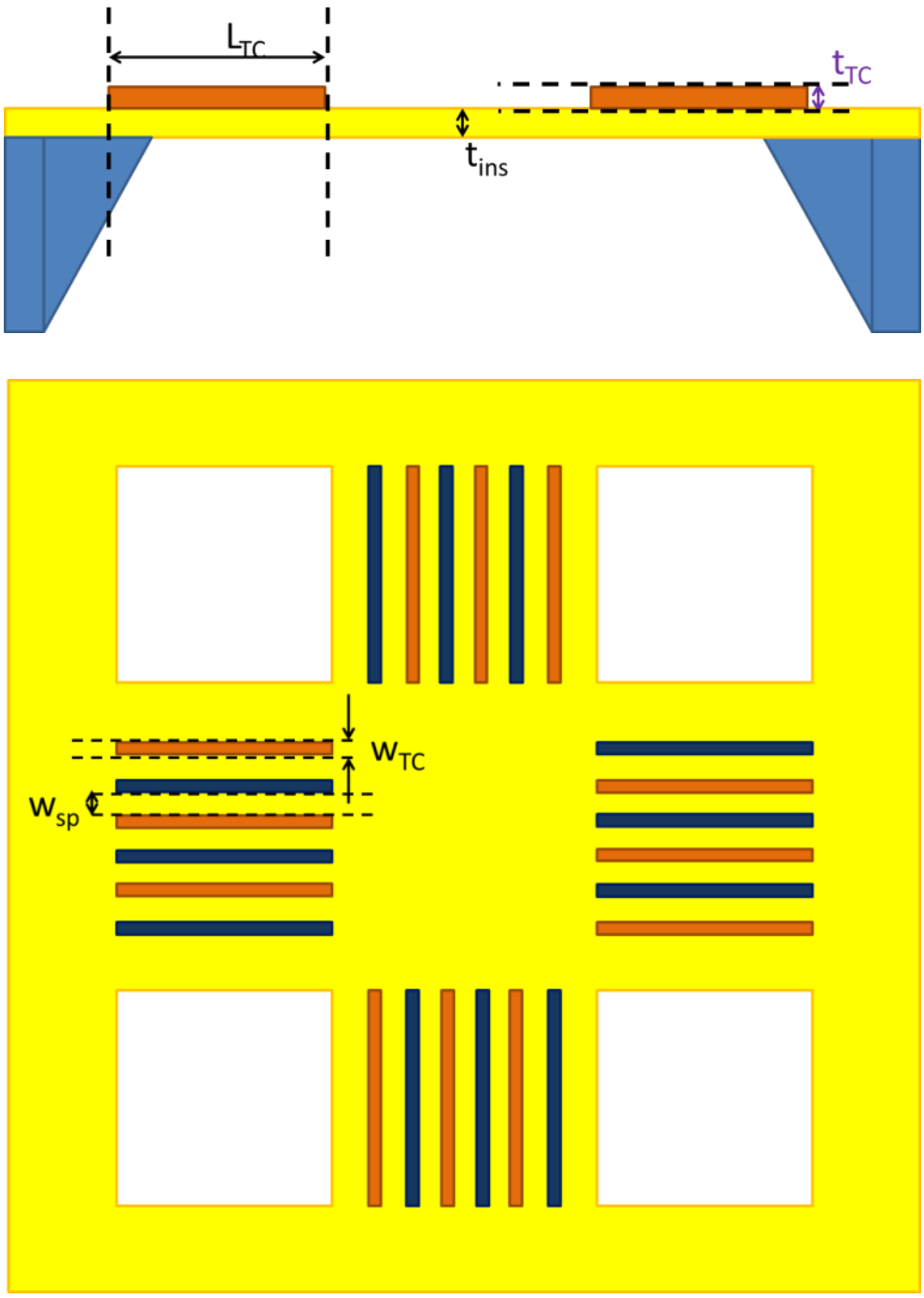

Figure 3.2. The geometric properties of the MEMS TE harvester on: a) cross section view and b) top view is shown.

As a first step, the number of thermocouples and the insulation layer thickness (t_{ins}) is fixed to derive a direct relation between thermal conductance and temperature profile along thermopiles. Once the analytical coupling is made, it can be applied to any geometry with varying thermocouple numbers (n), spacing (w_{sp}), layer thicknesses

(w_{TC}) and lengths (L_{TC}). It is important to note that the complete device size is fixed for the modeling to hold true. The calculation is model-specific in this case.

The equivalent thermal conductivity of the heat flow path is calculated as in Equation (3.2). The thickness of the Cr, Ni and parylene C layer, the area ratio of thermocouples and the thermal and electrical properties of these layers determine the equivalent thermal conductivity.

$$t_{eq}{}^{j} = \sum_{i=1}^{n} f_i^j \cdot t_i^j \tag{3.1}$$

Where $t_{eq}{}^{j}$ is the equivalent thickness of the diaphragm including thermopiles, f_i^j is the ratio of area covered by each layer to the total area, and t_i^j is the thickness of each layer in z-dimension. Equivalent thermal conductivity is:

$$k_{eq}{}^{j} = \frac{1}{t_{eq}^j} \sum_{i=1}^{n} f_i^j \cdot t_i^j \cdot k_i^j \tag{3.2}$$

The simplest way to obtain the temperature profile is to construct an equivalent electric circuit model and get the temperature at the hot and cold nodes accordingly. The equivalent electrical circuit of this system is shown in Figure 3.3.

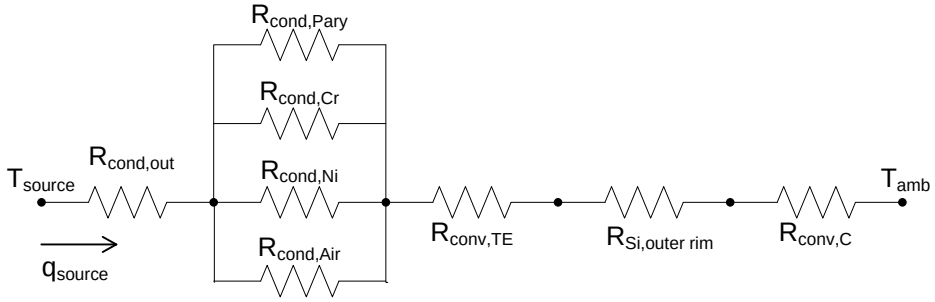

Figure 3.3. Equivalent circuit diagram of the TE harvester thermal system.

In Figure 3.3 R_{cond} terms denote the thermal conduction resistance of the parylene, Cr, Ni and air surrounding, respectively. $R_{conv,TE}$ denotes the convective thermal

resistance of thermocouples, $R_{Si,outer\ rim}$ denotes the conduction resistance of Si heat sink and $R_{conv,C}$ is the convection resistance at the cold junction. The thermal resistances are calculated with fundamental heat transfer equation (Equation (2.17)). Keeping the insulation layer thickness and number of thermocouples constant, equivalent circuit model gives varying cold side temperatures with varying thermocouple thicknesses. The number of thermocouples on one diaphragm arm is 12 and the length of the thermoelectric materials is 250 µm. When the hot junction is fixed at 310 K, the temperature profile along one thermocouple leg is shown in Figure 3.4 for different thermocouple thicknesses. The analytical calculation was performed using lumped electrical circuit model and finite element simulation was performed by parametric geometry modeling capability of Comsol Multiphysics 4.0. The details of the finite element model will be explained in the next chapter.

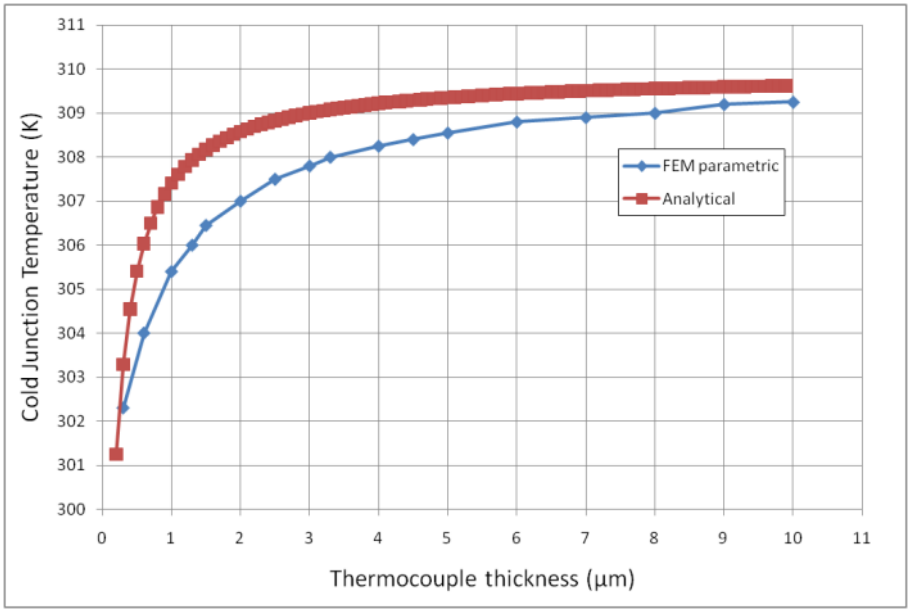

Figure 3.4. Graph of ΔT versus chromium thickness. The graph compares parametric finite element simulation results with the values calculated with lumped circuit model.

The equivalent electrical circuit model is a good approach for having an overall estimate of the temperature profile, but it is insufficient at times where a 3-D modeling of the temperature profile is needed. In an equivalent circuit model, mostly the convection effects are neglected and many simplifying assumptions are made to

obtain a mathematical result. At this stage it becomes crucial to construct an in depth thermal model of the TE microgenerator to calculate the performance more precisely in a realistic way. In a real heat transfer problem, convection effects are out of plane and a fixed temperature at ambient at the cold junction does not hold true for most of the time. For a general heat transfer problem, the heat equation is shown in Equation (3.3).

$$\rho \cdot C \cdot \frac{\partial T}{\partial t} - \nabla \cdot (k \nabla T) = Q + h(T_{ext} - T) \tag{3.3}$$

where ρ is the density of the material, C is the heat capacity, t is the time, k is the thermal conductivity, Q is the heat source, h is the convective heat transfer coefficient, T_{ext} is the ambient temperature and T is the temperature at the node where the solution will be calculated. At steady state the first term at the left side vanishes, and the elliptic version of heat transfer equation reduces to Equation (3.4).

$$-\nabla \cdot (k \nabla T) = Q + h(T_{ext} - T) \tag{3.4}$$

For heat flowing through a cross section, specifically a bridge structure, the heat transfer equation with convection is shown by Equation (3.5).

$$\frac{\partial^2 \theta(x)}{\partial x^2} - \frac{h \cdot P}{k_{eq} \cdot A_{cross}} \cdot \theta(x) = 0 \tag{3.5}$$

Where $\theta(x)$ is the temperature difference from ambient at location 'x' $(T(x) - T_{amb})$, h is the free convection coefficient from the surface to air, P is the perimeter where heat flow occurs, k_{eq} is the equivalent thermal conductivity of the heat flow path and A_{cross} is the cross sectional area of the bridge.

In order to solve this differential equation, the boundary conditions on the hot and cold ends of the thermocouple structure should be set appropriately. A 2-D representation of the heat flow path on thermoelectric membrane is shown in Figure 3.5.

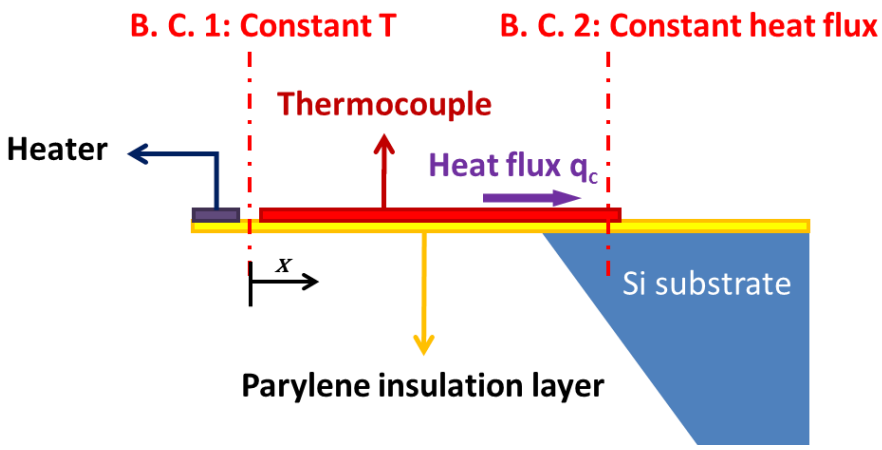

Figure 3.5. A 2-D representation of the thermocouples on parylene C.

In this heat transfer problem, the boundary conditions on the hot and cold junction are fixed temperature, and constant heat flux respectively.

Here, the first boundary condition is:

$$T_{hot} = 310\ K \tag{3.6}$$

The second boundary condition is:

$$-k \cdot \frac{\partial T(x)}{\partial x} = q_c \tag{3.7}$$

where x is the distance from the hot end, k is the equivalent thermal conductivity of the heat flow path, x is the translational length, $T(x)$ is the absolute temperature as a function of x and q_c is the heat flux from the thermopile to the silicon substrate at the cold junction.

The heat flux from the TE cold junction changes with varying thickness. There are two unknowns in the heat equation, i.e. Equation (3.3): the temperature along the nodes of the thermopile and the heat flux. Successive results for different designs were obtained through finite element analysis (FEA), and each calculated heat flux value was set as a boundary condition to construct a temperature profile formulation accordingly. The algorithm provides a model based solution. The formulation was

useful to make a realistic parametric optimization of the power obtained from the TE microgenerator.

Solving the heat transfer equation using these boundary conditions, we obtain the results shown in Figure 3.6.

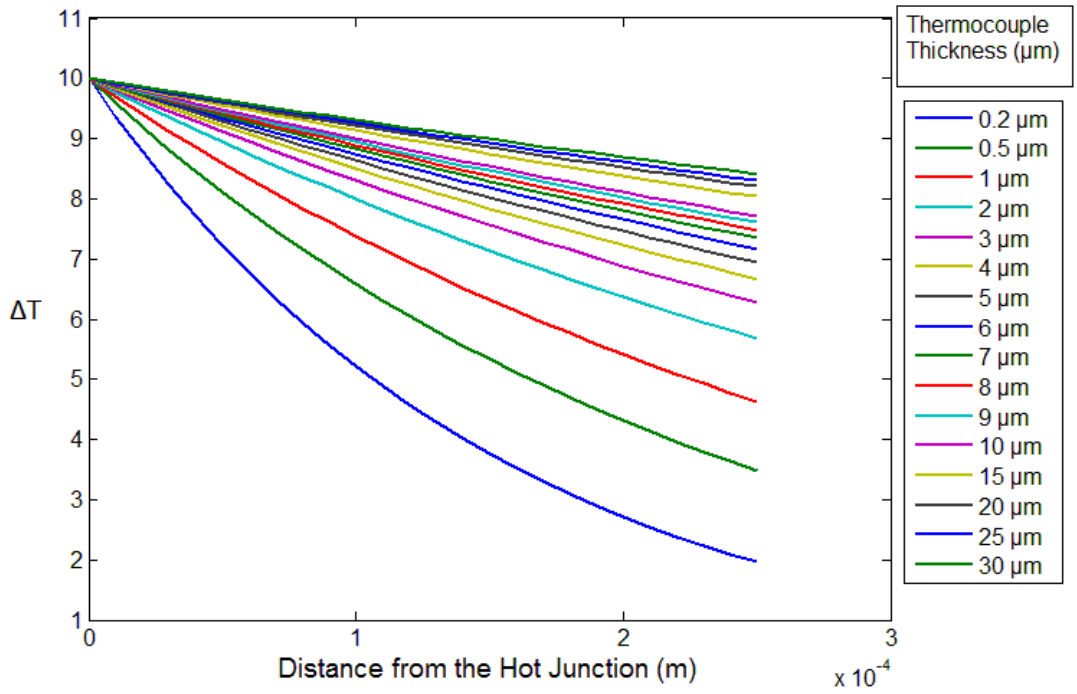

Figure 3.6. Temperature profile from analytical calculation based on boundary conditions.

To double check analytical results, finite element modeling of temperature profile was performed using Comsol Multiphysics. Geometric parametrization has been used for solving the temperature profile for varying thermocouple thicknesses. The subdomain temperature profiles for 1 µm, 2.5 µm, 5 µm and 10 µm thick thermocouples are shown in Figure 3.7.

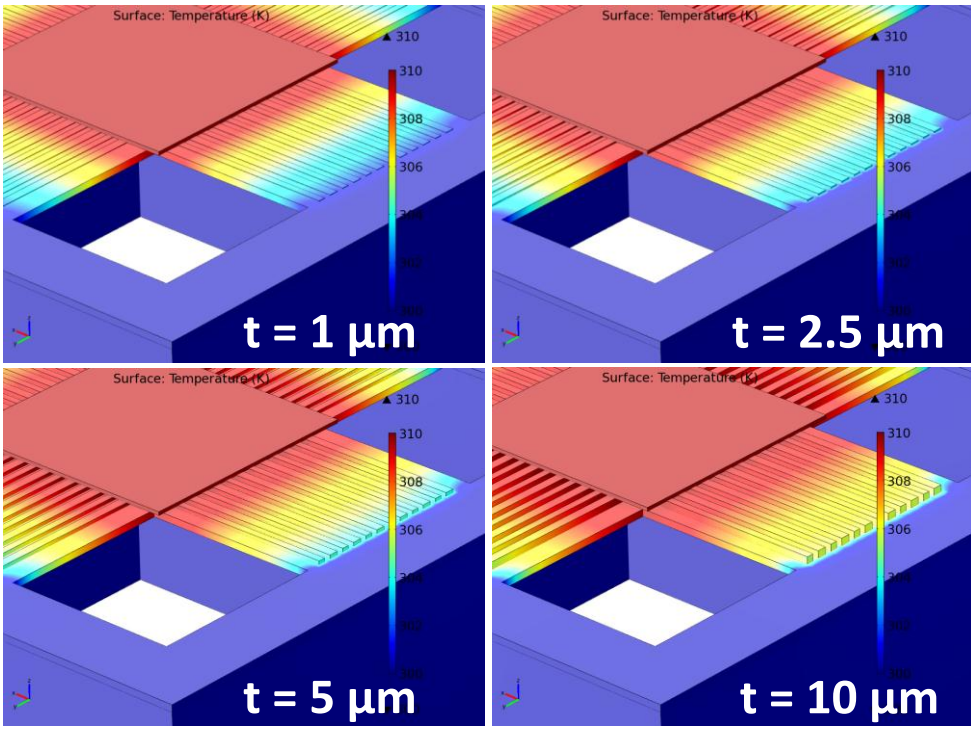

Figure 3.7. The temperature profile on the thermocouples with varying thermocouple thickness.

The cold junction temperature at a thermocouple thickness range between 0.1 and 10 µm is shown in Figure 3.8.

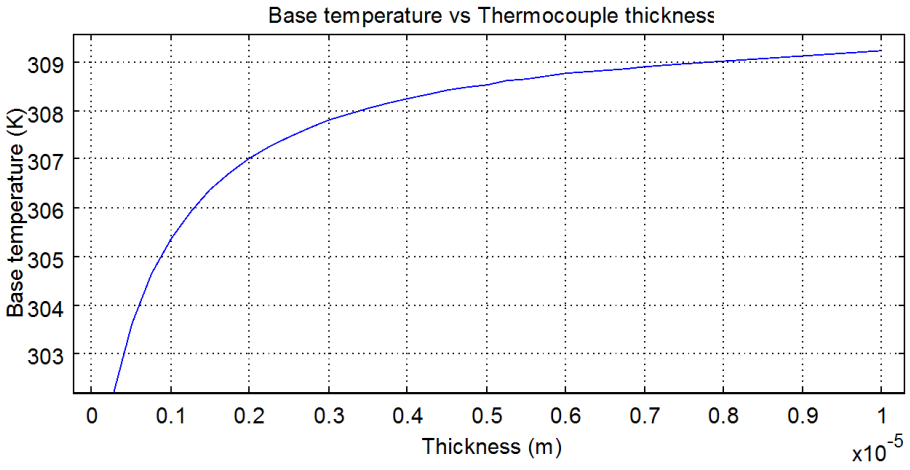

Figure 3.8. Temperature profile on the cold junction of one thermocouple versus its thickness in z-dimension.

As it can be seen from Figure 3.8, the cold side temperature converges to the temperature of the heat source as the thickness gets larger. The increase of the thickness means the decrease of the thermal resistance regarding (2.17). This result is expected if the problem is considered using heat transfer point of view.

3.1.2 Calculation of Temperature Profile by Finite Difference Method

The thermocouples for thermoelectric generation lie on the four arms of the suspended parylene diaphragm in the design. Since the performance of the thermoelectric conversion system depends on the level of temperature difference, it is essential to model the temperature profile of the diaphragm including thermocouples in a realistic way. Finite difference method is the most suitable method to implement in this kind of heat problem.

In finite difference method, the domain is discretized to many elements and dependent mathematical relations are constructed within the nodes. These nodes are the only points where dependent variables are calculated. In this method of solution of partial differential equations, the derivatives are represented by differences.

A wide range of problems including one PDE to several PDE's can be solved by finite difference method. Number of PDE's to solve means the number of conservation statements to solve. In numerical heat transfer problem like any other physical problem, there is a set of conservation statements to construct. These conservation statements can be just one to many. In heat transfer problems, mostly mass, momentum and energy conservation principles are considered. The continuum problem is discretized to many elements (control volumes) and the conservation principles are applied to these elements.

The first step to solve a PDE problem by finite difference method is discretizing the continuous domain to many elements called finite difference meshes. These meshes contain finite number of grid points. In a two-dimensional domain represented by Cartesian coordinates (x,y), the continuous function $u(x,y)$ is replaced by $u(i\Delta x,j\Delta y)$. Points in the domain are represented by grid points i and j. The finite difference

equations in one mesh therefore are constructed according to this global point and its neighbors [35]. A finite difference grid representation is shown in Figure 3.9.

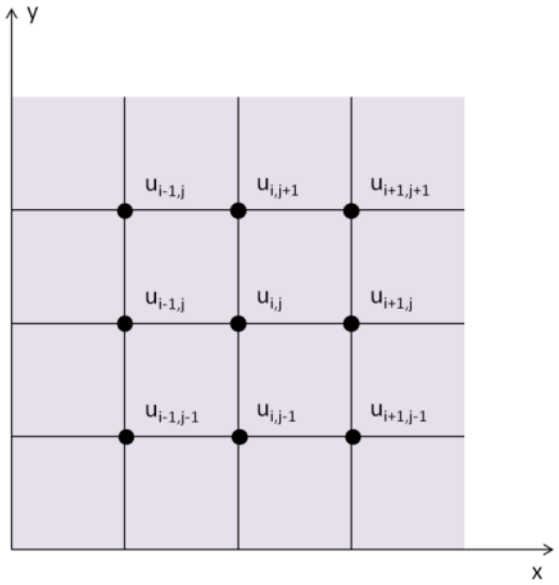

Figure 3.9. Mesh discretization for finite difference method solution.

The variable *u* in this grid is represented as in Equation (3.8).

$$u_{i+1,j} = u(x_0 + \Delta x, y_0) \qquad u_{i-1,j} = u(x_0 - \Delta x, y_0)$$
$$u_{i,j+1} = u(x_0, y_0 + \Delta y) \qquad u_{i,j-1} = u(x_0, y_0 - \Delta y) \tag{3.8}$$

The derivative of the function u(x,y) at point x_0,y_0 can be represented by Equation (3.9). Finite difference method solution is based on this representation.

$$\frac{\partial u}{\partial x} = \lim_{\Delta x \to 0} \frac{u(x_0 + \Delta x, y_0) - u(x_0, y_0)}{\Delta x} \tag{3.9}$$

As the performance of our thermoelectric generator depends on the temperature difference between the hot and cold junctions, it is important to calculate the temperature distribution along the thermocouples and the diaphragm arms that they lie on accurately. In our problem, there is both conduction and out-of-plane

convection (convection in z direction) along the arms. The adiabatic boundary condition is provided by the silicon heat sink.

Here, the temperature profile for 12 thermocouples on one arm will be calculated. The thickness of Cr and Ni are 0.63 μm and 0.5 μm, respectively. The width of the thermocouples is fixed at 10 μm and the diaphragm is 5 μm thick Parylene C. For the analytical solution, the problem would be the continuous heat transfer problem, depicted in Equation (3.3).

We can say that our problem is symmetric, since each diaphragm arm stretches in each direction from the middle of the diaphragm. So we can consider the temperature distribution just in one diaphragm arm. Considering the arm shown in Figure 3.10, there is a constant heat flow from the left. The base of the arm is overlaid on silicon substrate, which makes the right edge adiabatic. There is conduction along the arm and thermocouples, and out-of-plane convection in both z and –z directions. The problem domain and the boundary conditions are shown in detail in Figure 3.10.

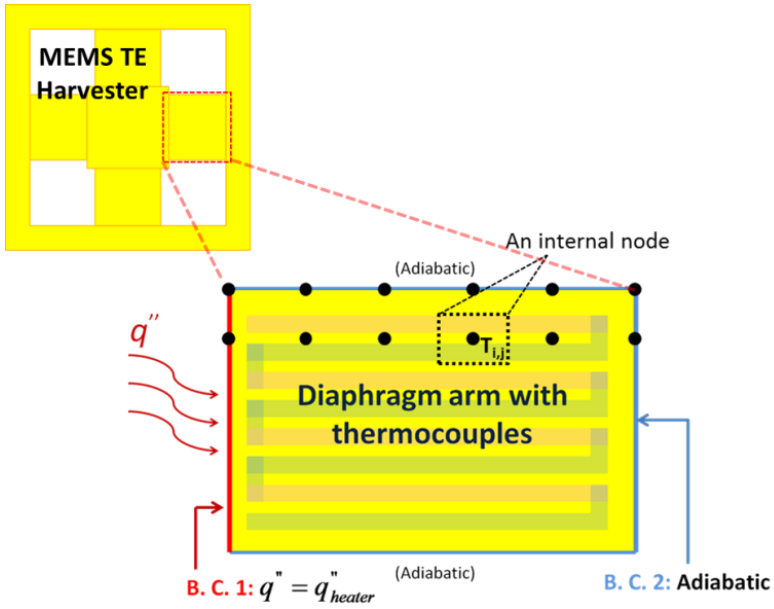

Figure 3.10. The problem domain is the diaphragm arm and thermocouples on it. The outer area sits on Silicon heat sink. A close up on the diaphragm arm with the boundary conditions is shown.

Once we discretize our problem domain to small elements (meshes), we have an energy conservation equation for each element. Although the equation alters at some locations (the edges and corners), the principal is the same. For example, the energy conservation in all internal nodes can be shown in Figure 3.11, and is expressed as in Equation (3.10).

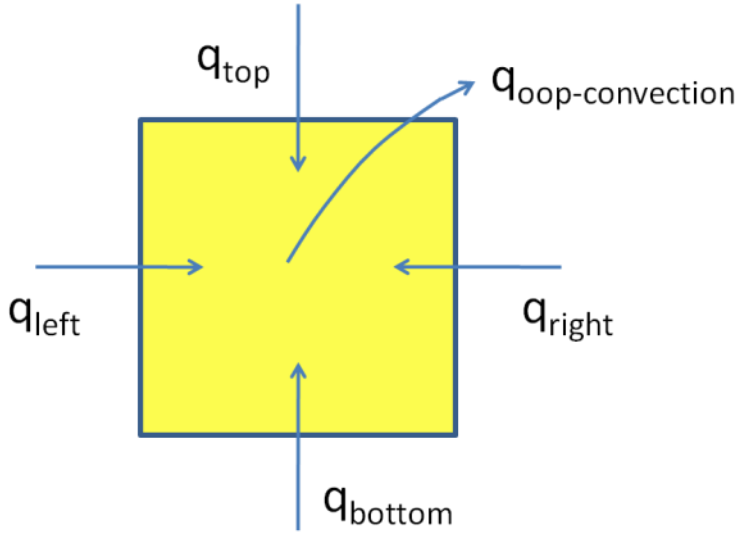

Figure 3.11. Energy conservation equation at an internal mesh of the problem domain.

$$q_{left} + q_{right} + q_{top} + q_{bottom} + q_{oop-convection} = 0 \qquad (3.10)$$

Where $q_{(direction)}$ shows the heat coming from each direction to that node and $q_{oop\text{-}convection}$ represents the heat loss due to convection out of plane (in z-direction where the problem is seen in x and y coordinates).

For instance, consider an internal node on the diaphragm illustrated in Figure 3.11. The heat coming from left to the node in question can be expressed as in Equation (3.11).

$$q_{left} = \frac{T_{i-1,j} - T_{i,j}}{\frac{\Delta x}{k \cdot \Delta y \cdot t}} \qquad (3.11)$$

Where Δx is the incremental length where heat flows, t is the thickness in z direction and $\Delta y \cdot t$ is the cross sectional area where the heat flows. To form the energy conservation on one node, all the heat coming from and flowing out at the other sboundaries (q_{right}, q_{top}, q_{bottom}, $q_{\text{oop-convection}}$) are written in the same way.

Writing down the equations for each node (same for internal nodes, different at the edges and corners) as matrices and solving them in MATLAB, the temperature profile in the diaphragm is found. The equivalent thermal conductivity is calculated considering the thermal conductivities and geometry of the insulating material and thermocouples. The inward heat flux used as the 1st boundary condition is the average heat flux through the cross section calculated by COMSOL Multiphysics. Since the power supplied by the heater spreads in every direction, it is difficult to estimate what percent of the heat is going directly in the transverse direction of the arm. The results are shown in Figure 3.12. As the number of meshes increase, the solution of the problem converges to a definite value.

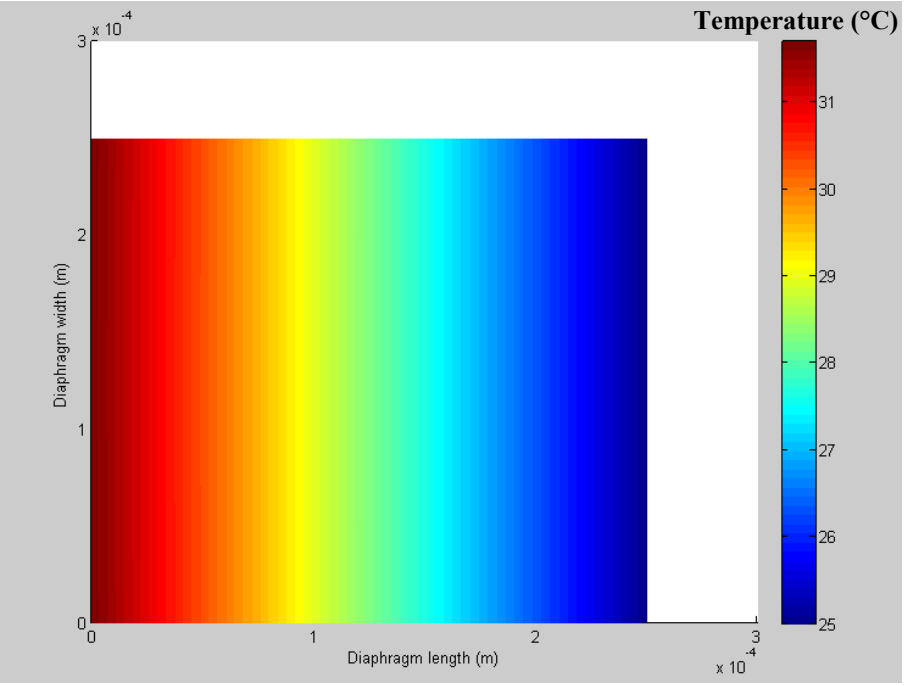

Figure 3.12. The temperature profile on one diaphragm carrying 16 thermocouples. The domain consists of 500 x 500 nodes.

The convergence of the temperature difference value is shown in Figure 3.13. It is anticipated that excessive time and processor power is spent for too many meshes.

Since the accurate enough result is reached in 3rd step, it is reasonable to do the finite difference simulations with 50x50 meshes.

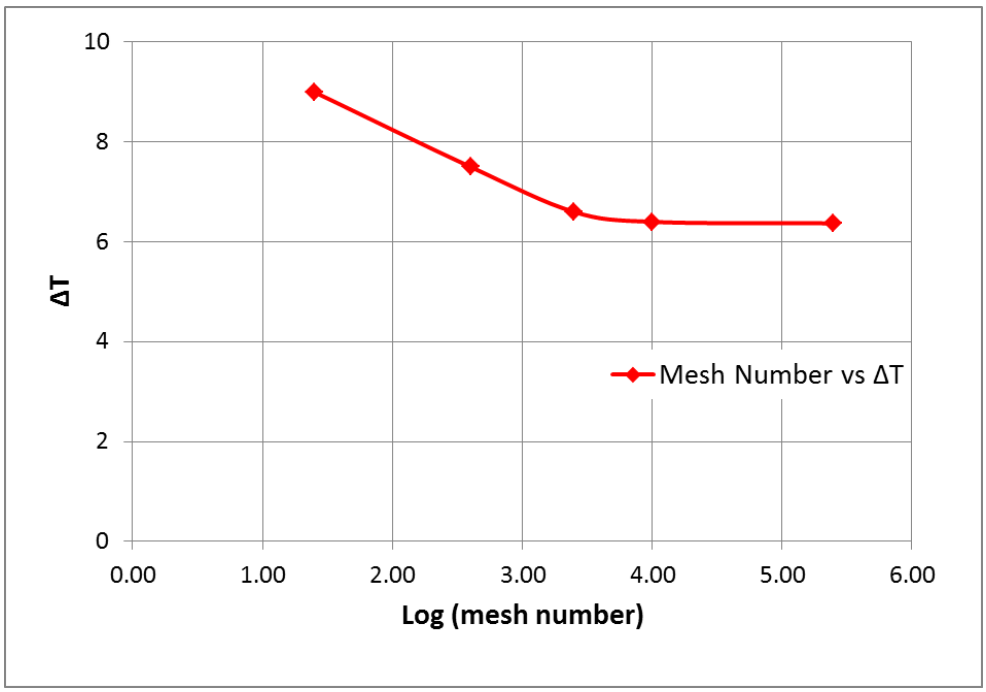

Figure 3.13. Mesh number versus the temperature difference between the hot and cold junctions (ΔT) for finite difference simulation along 1 diaphragm arm carrying 16 thermocouples.

Table 3.1 shows the comparison of analytical, FEM and finite difference calculations for the same TE harvester geometry. The number of thermocouples is 48, the diaphragm arm length is 250 µm, and the thickness of Cr and Ni layers are 0.63 µm and 0.5 µm, respectively. It can be seen from Table 3.1 that the results obtained with different methods are within %2.27 error tolerance.

Table 3.1. Comparison of temperature calculations obtained with different methods.

Method	T_H (K)	T_C (K)	ΔT
FEM	310	303.4	**6.6**
Analytical	310	303.52	**6.48**
Finite Difference	310	303.55	**6.45**

3.2 Transient Thermal Analysis

The transient thermal calculations have been performed to predict the dynamic response of thermoelectric energy harvester. The time constant to reach the structure to thermal equilibrium is shown by Equation (3.12).

$$\tau = \frac{C_{th}}{G_{th}} \tag{3.12}$$

where C_{th} is the heat capacitance and G_{th} is the thermal conductance of the structure.

In the transient model, a TE device structure having 48 thermocouples with a thickness of 0.5 μm thermoelectric material thickness is used. The thermal time constant calculated by a transient finite element analysis is shown in Figure 3.14.

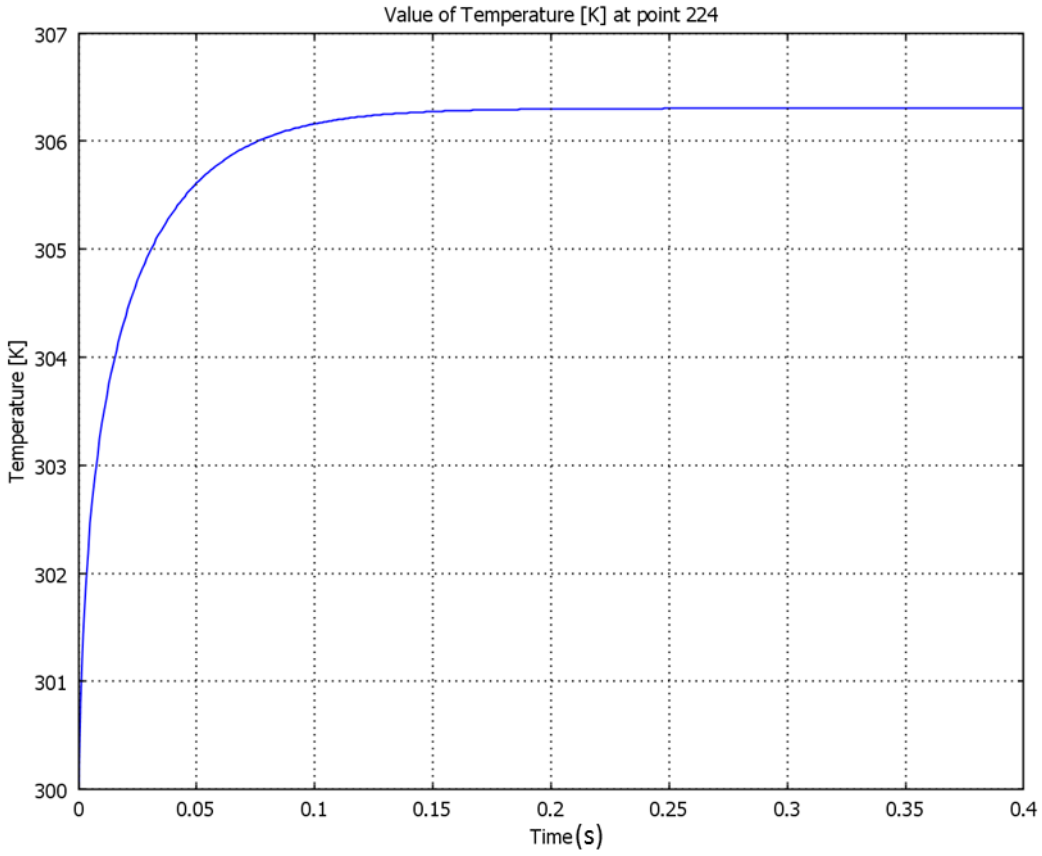

Figure 3.14. The time response of one thermoelectric leg to heating. The time

constant is 94 milliseconds.

The time constant is the time required to reach %63.2 of the steady state temperature difference. Exporting the data reveals that the time constant of the structure is 94 ms.

3.3 Heater Design

3.3.1 Heater Material Selection and Limitations

The thermoelectric heater is optimized to supply the required temperature difference. The heaters should be designed to supply enough power to heat the thermocouples for testing purposes. On the other hand, the heaters should not be burned due to excessive current flow. There is a maximum limit a wire can carry according to its material properties and geometry. The wire width and thickness are the restricting factors that limit the maximum electric current it can carry. So, a sufficient thickness of Ti heater should be deposited to carry enough amount of current density. For an accurate analysis for a microfabricated heater, self consistent design theory used for VLSI circuits was applied. The maximum temperature in a resistively heated heater is shown by (3.13) [36].

$$\Delta T_{max} = \frac{j_{rms}^2 \cdot \rho \cdot L_h^2}{k_m} \tag{3.13}$$

where ΔT_{max} is the average temperature difference supplied, j_{rms} is the rms value of the electric current density in the wire cross section, ρ is the electrical resistivity, L_h is the characteristic length, and k_m is the thermal conductivity of the metal.

Choosing Titanium for the heater material will be a good choice because with the same electrical current, the heating power for the thermocouples will be much higher. As there are many thermocouples, a large amount of heating power will be needed to supply sufficient temperature gradient through the thermocouples. Electrical currents lower than 0.5 mA are safe in terms of electrical breakdown and electromigration. When Ti is chosen as the heater material, the maximum temperature rise in the Ti heater versus the electrical current supplied is given in Figure 3.15.

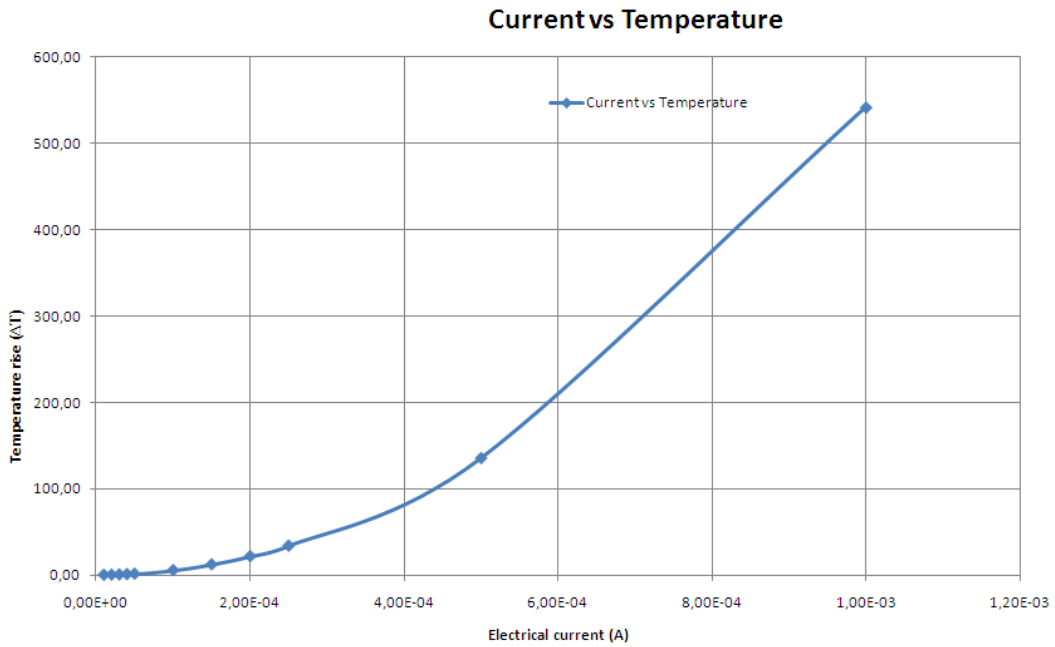

Figure 3.15. Temperature rise versus electric current supplied to titanium heater.

3.3.2 Calculation of the Heating Power

In order to calculate the heating power to cause an amount of ΔT between the junctions, the heater code was combined with the thermoelectric analytical model. The required heating power is calculated by performing a heat balance at the cold junction, which is shown by (3.14).

$$\dot{Q}_h = \alpha_{np} T_h I - \frac{1}{2} I^2 R + K(T_h - T_c) \tag{3.14}$$

Where the first term on the right hand side is the Peltier heat, the second term is the Joule heating term and the last term is heat conduction. The required heating power for varying thermoelectric geometries is shown in Figure 3.16.. Here it should be noted that, the number of heater length depends on the number of thermocouples. As the number of thermocouples increase, available diaphragm width that carries the heater increases.

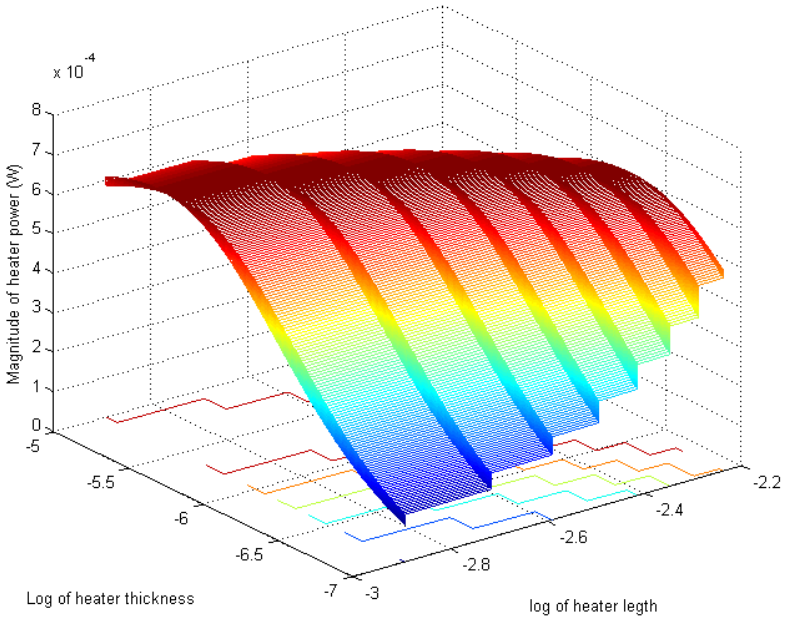

Figure 3.16. The required heating power for testing purposes of thermoelectric generator. The heater length and thickness is varied.

As it can be seen from Figure 3.16, the required heating power is between 100 and 800 μW. The heater voltage supplied to heater resistance is shown by Equation (3.15).

$$V = \frac{P_{heater}}{I_{heater}} \tag{3.15}$$

Where P_{heater} is the heating power and I_{heater} is the electric current passing through the heater resistance. Since the heater resistance can be calculated for any geometry, the required heater voltage can also be calculated. The required heater voltage for a titanium heater is shown in Figure 3.17.

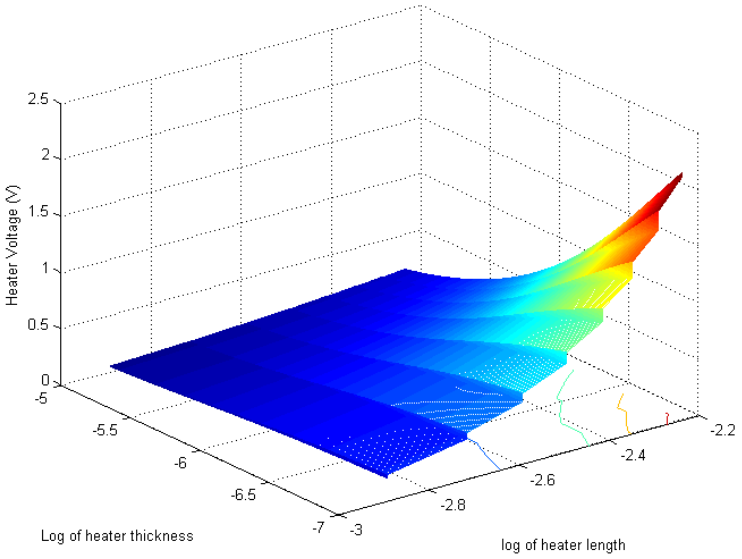

Figure 3.17. The required heater voltage given to the heater pads.

The current density in the Ti heater is seen in Figure 3.18. The geometry for the Ti heater should be chosen accordingly not to exceed maximum affordable current limit. The most important parameters that determine the maximum current that a wire can carry is the width and thickness of the heater.

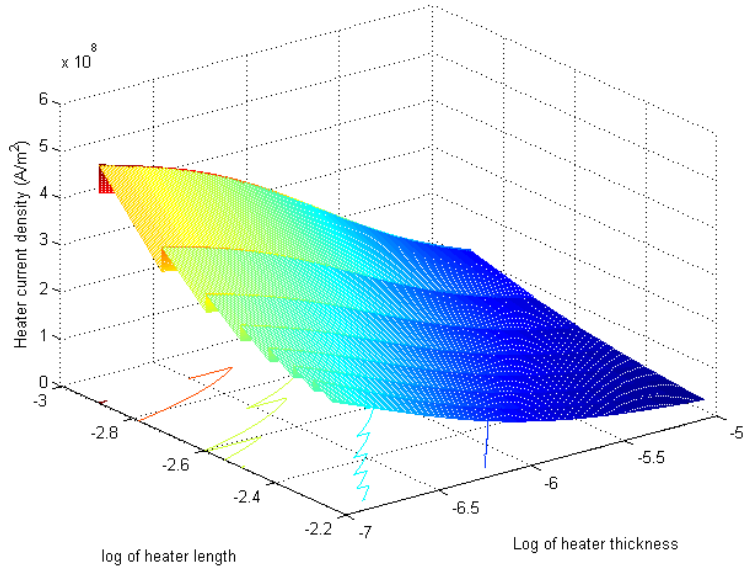

Figure 3.18. The current density of the Ti heater.

3.4 Performance Evaluation

In a thermoelectric generator, the key parameters that determine the generated voltage are the temperature difference between the hot and cold junction and the Seebeck coefficient of the material used (See Equation (2.1)). So it becomes important to maximize these two parameters. For a constant heat given to a lateral TE harvester, the temperature difference can be modified within limits. The total thermal conductance between hot and cold junctions should be made as low as possible to provide a significant thermal gradient. The available thermoelectric materials at hand are limited, so they should be selected according to their thermoelectric power factor to get high Seebeck voltage. Moreover, it is necessary to construct a geometry based performance optimization for this lateral thin film TE energy harvester. Once the model is constructed properly, it can be adapted to any thermoelectric material possible. To obtain a high thermoelectric power, the electrical resistivity should also be as low as possible to avoid high electrical resistance. The device geometry optimization is based on three major parameters:

- Thermoelectric material thickness
- Thermoelectric material length
- Number of thermocouples

The insulation layer thickness, heat sink and other factors also affect the thermoelectric performance, but their contributions are not as major.

The temperature profile with a fixed geometry was calculated in previous sub-chapter using general heat transfer equation and convenient boundary conditions. This modeling of temperature profile is based on total thermal conductance between the hot and cold junction. So, it will be reasonable to compose an analytical formula that bases the temperature distribution on total conductance whatever the number of thermopiles or the geometry is. The comparison of analytical modeling and finite element modeling has also shown that this approach in modeling thermoelectric device performance was correct. Here, it is important to note that thermocouple number is coupled to the diaphragm length. Given a constant spacing between

thermocouples, there is a limited number of thermocouples that can be fitted on a diaphragm arm. The figure that represents this relation is shown in Figure 3.19.

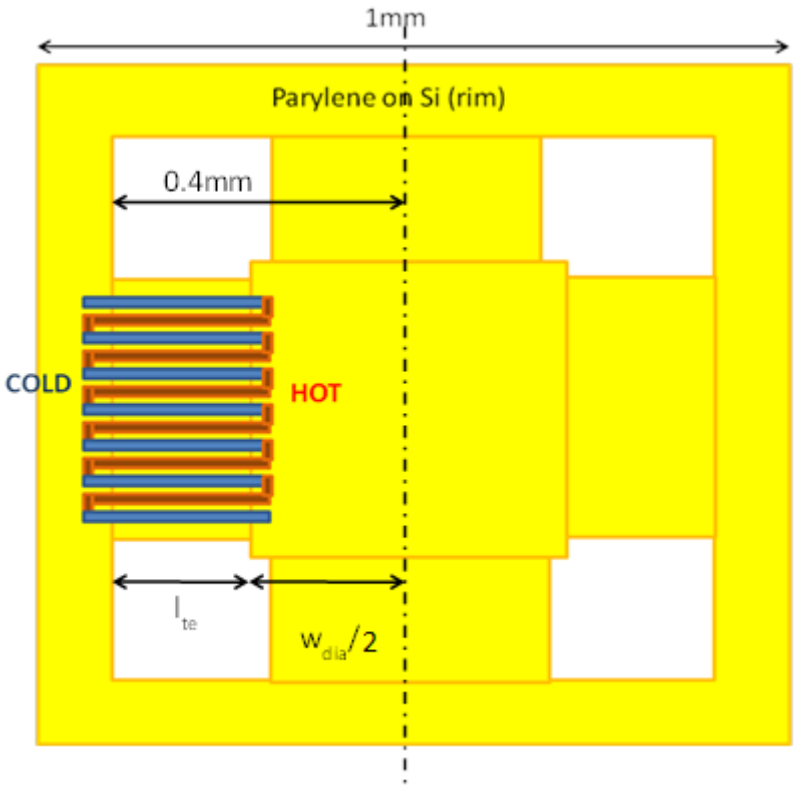

Figure 3.19. The thermoelectric device geometry.

The maximum number of thermocouples that can be fitted on one diaphragm arm is shown in Equation (3.16).

$$n = \frac{w_{diaph,arm} - (50e - 6)}{(w_{tc} + w_{sp})} \cdot \frac{1}{2} \tag{3.16}$$

The voltage extracted from a thermoelectric harvester is calculated from Equation (2.1). Since the temperature difference can be calculated including the Joule, Peltier and Thomson effects on any thermoelectric device geometry, it was possible to calculate the voltage.

In terms of voltage, the thermocouple thickness should be kept as low as possible to sustain the maximum temperature difference between the hot and cold junctions. In

this design, the equivalent thermal resistance in a constant area is the primary design parameter that determines the performance of the generator. However, decreasing the thickness thus the cross section of the thermopiles substantially increases the electrical resistance. As it can be anticipated by (3.17), the power generated decreases dramatically with the decreasing thermopile thickness.

Using Cr and Ni as the p-type and n-type thermoelectric materials, the voltage generated with varying thermocouple thickness and length is seen in Figure 3.20.

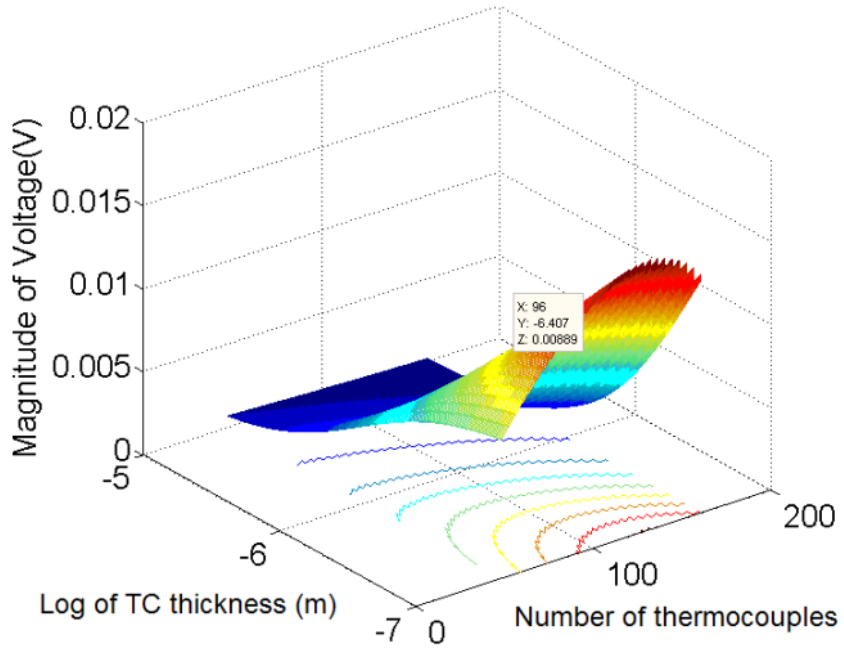

Figure 3.20. The voltage generated by MEMS thermoelectric harvester. The thermocouple thickness and total number is varied.

The electrical power assuming a matched load resistance (R_{te}=R_l) is calculated by Equation (3.17).

$$P = \frac{V^2}{4R_{te}} \tag{3.17}$$

Where V is the thermoelectric voltage, and R_{te} is the internal thermoelectric resistance.

The generated thermoelectric power from a 1mm x 1mm MEMS TE device is seen in Figure 3.21.

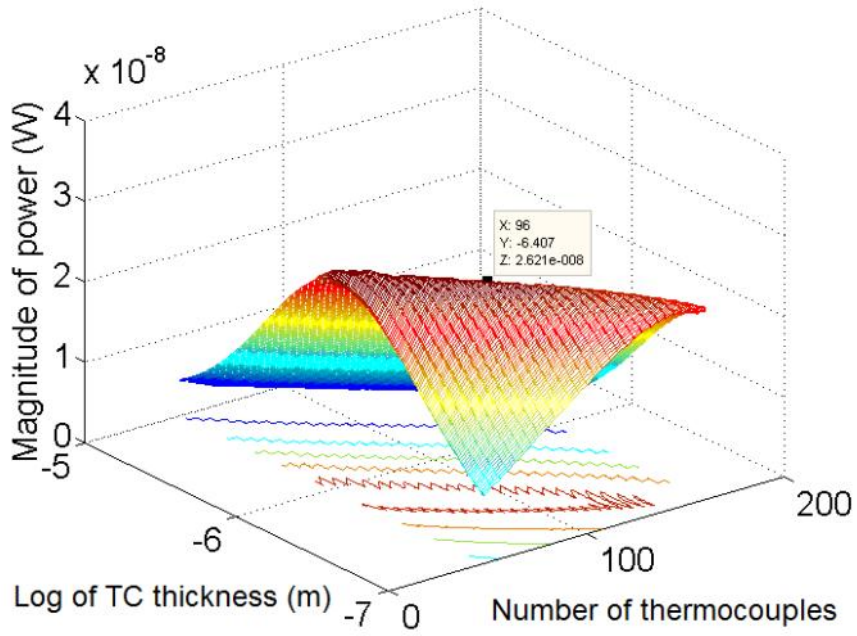

Figure 3.21. Generated thermoelectric power from 1mm x 1mm TE device with Cr-Ni thermopile.

One conclusion from the performance results is, the generated thermoelectric power does not always increase with increasing number of thermocouples. There is a maximum power limit that can be reached with a specific thermocouple number and thickness combination. Having a more detailed look on Figure 3.21, the local maximum shifts to lower number of thermocouples as the thermocouple thickness increases. The result is reasonable since it is easy to predict that the total thermal conductance will increase with increasing thermocouple thickness. So, the maximum power will occur at lower number of thermocouples, which provides a lower thermal conductance thus a higher temperature difference between hot and cold junctions.

Using n-Si and p-doped polysilicon as thermoelectric materials, the voltage and power calculated are shown in Figure 3.22 and Figure 3.23. The material properties of thermoelectric materials are adapted from [37].

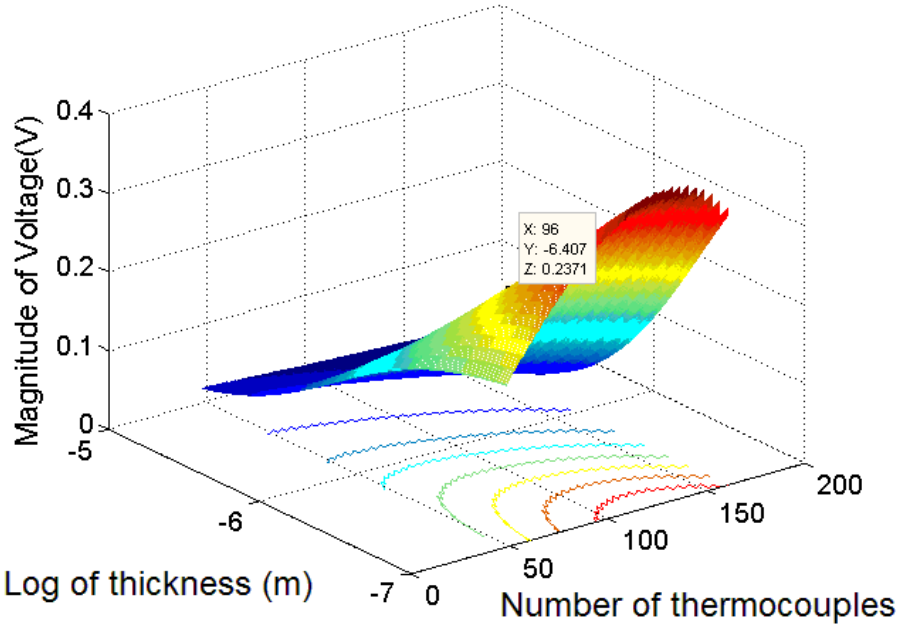

Figure 3.22. The voltage generated by MEMS thermoelectric harvester. The thermocouple thickness and total number is varied.

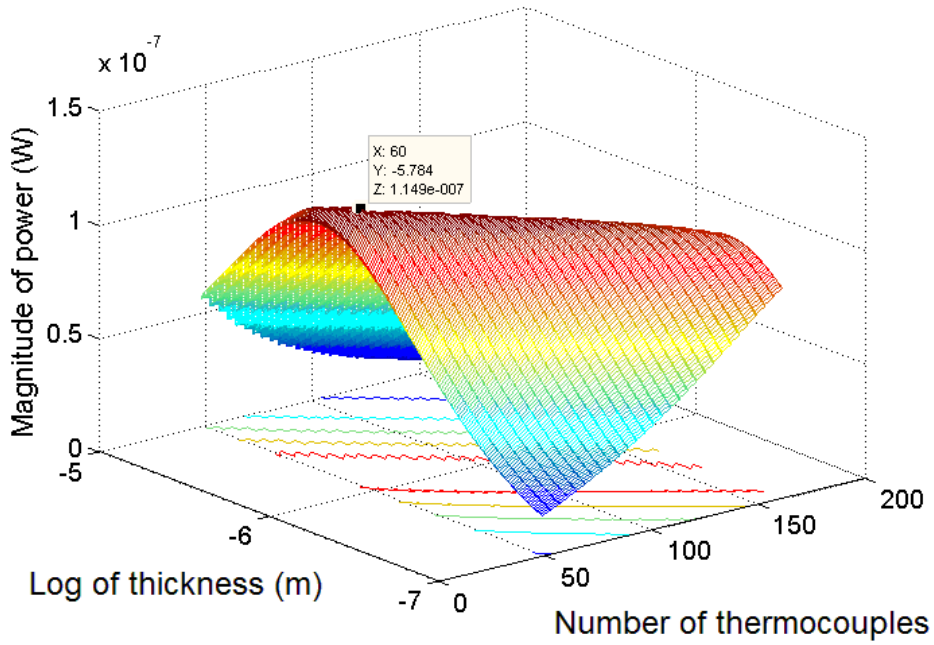

Figure 3.23. Generated thermoelectric power from 1mm x 1mm TE device with p-Si and n-polysilicon thermopiles.

As it can be concluded from Figure 3.23, using p-doped Si and n-polysilicon, the thermoelectric generators yield ~7 times more power than the Cr-Ni based thermoelectric generators.

3.5 Possible Integration of Thin Film MEMS TE Energy Harvesters in Mobile Systems

The MEMS thermoelectric energy harvesters presented here are designed to harness electrical energy from waste heat generated in mobile systems. So, the feasibility of MEMS TE energy harvesters in a notebook computer is analyzed in this section. First, the thermal profile of a Dell Alienware M17xR2 notebook computer is composed using thermocouples and thermal camera [38]. In each regions in the case of the computer, the cold and hot junction temperatures were recorded. Using these ΔT values, the performance of Cr-Ni based and p-Si and n-polysilicon based MEMS TE energy harvesters were evaluated. The simulation results are shown in Table 3.2.

Table 3.2 The electrical power estimated when MEMS TE modules are integrated to Dell Alienware M17xR2 notebook.

Analyzed Region	T_{HOT}	T_{COLD}	Region Dimensions (mm)		ΔT	Space available for TE module integration (in z)	Total Power Generated by Using Cr-Ni Thermopile (μW)	Total Power Generated by Using n-poly and p-Si thermopile (μW)
			x	y				
Processor and heat slub top (end of heat pipe)	100	74.5	34	36	25.5	1-2 mm	211.8	905.8
Heat slub top and the metal attach above it	74.5	46	34	36	28.5	3 mm	270.5	1102
Metal attach above heat pipe and surface temperature	46	40.4	22	16	5.6	4 mm	3.03	12.32
Motherboard (main PCB card) and surface temperature (top)	45.1	34.4	10	5	10.7	8 mm	1.55	6.6
Motherboard (main PCB card) and surface temperature (bottom)	45.1	32.4	10	5	12.7	7 mm	2.15	8.45
Nod on the metal layer under PCB (T5) and surface (bottom)	36.8	33.6	4	4	3.2	9 mm	0.045	0.18

3.6 Performance benchmarking of the MEMS TE Energy Harvesters

The estimated performance of the MEMS TE energy harvesters was evaluated and presented. In order to get an overall idea about the performance rating of the MEMS TE harvester, it is compared to lateral TE harvester structures in literature. The rating metric used here is $\mu W/K.cm^2$. It shows the electrical power density obtained when 1K temperature difference is created. The comparison is given in Table 3.3.

Table 3.3. Comparison of MEMS TE energy harvesters with its counterparts in literature.

Author/Year	Heat Flow Path	TC leg length (µm)	TC cross section area (μm^2)	Integration (TCs/cm^2)	TE material	Electrical resistivity(ohm.m)	TC patterning	Int. Resistance (ohm/cm^2)	Contact resistance (ohm/TC)	TE efficiency factor ($\mu W/K^2cm^2$)
Rowe et al. 89 [39]	Lateral	4500	100 x 0.4	55.6	p-Si n-Si	-	RIE	$1.74x10^5$	~2800	0.012
Glosch et al. 99 [4]	Lateral	500	7 x 1.2	6060.6	Al n-Si	- $1.4x10^{-5}$	-	$5.45x10^6$	~65	0.91
Strasser et al. 02,04 [5]	Vertical	18.5	6 x 0.4	225400	p-polySi n-polySi	$1.5x10^{-5}$ ($2.1x10^{-5}$)	RIE	29 x 10^6 (35.5x 10^6)	~0.65	0.58 (0.36)
Sordeur, Stark 97,99 [40]	Vertical	~1200	50 x 2.5	3333.3	$(Bi_{0.25}Sb_{0.75})_2Te_3$ $Bi_2(Se_{0.1}Te_{0.9})_3$	2.2 x 10^{-5} 1.7 x 10^{-5}	-	1.33 x 10^6	-	3.34
Itoigawa, Hasebe 04,05 [41]	Vertical	3000	300 x 2	~22.7	Cu Ni	-	UV-photoresist	~463	-	~7.4 x 10^{-5}
Kishi et al. 97,99 [10], [11]	Vertical	600	80 x 80	2600.0	BiTeSb Bi_2Te_3	-	With wafer saw	~2500	-	~5
Böttner et al. 04 [42]	Vertical	20	~500x 50	1070.0	$(Bi,Sb)_2Te_3$ Bi_2Te_3	1.2 x 10^{-5} 1.6 x 10^{-5}	RIE	~450	~0.0004	11.9
MEMS TE Generators	Lateral	50-350 (Variable)	10 x 0.4 (Variable)	1600	Cr Ni	1.29e-7 0.72e-7	UV-photoresist	~3700	Negligible	0.738 (SIMULATED)
MEMS TE Generators	Lateral	50-350 (Variable)	10 x 0.4 (Variable)	4000	p^+ doped Si n-polysilicon	3.7 x 10^{-5} 8.5 x 10^{-6}	UV-photoresist	~1.47 x 10^6	Negligible	4.04 (SIMULATED)

3.7 Discussion on the Results

In the simulations, it is seen that maximizing the temperature difference is a good way to maximize Seebeck voltage. However, our aim was to maximize electrical

power obtained. So, we should adjust the temperature difference such that power will not be compromised. The optimum design points are searched by varying the geometric properties of the energy harvester; namely the number, length, width and thickness of the thermocouples. By using an analytical optimization method, local maximums and minimums of the generated power are found. For an optimization to take place, a few parameters like the thermocouple width and insulation layer thickness is kept constant. The main consideration here is the thermal conductance here, which can be changed by varying the thickness, length and number of thermocouples. It was seen from Figure 3.21 and Figure 3.23 that there are many design points where the maximum power occurs, i.e. there is a range of optimum thickness for each thermocouple length and number chosen, and vice versa. So, the design of the thermoelectric harvesters have been made considering these results. Table 3.4 shows the span of acceptable design parameters for a Cr-Ni based MEMS TE energy harvester.

Table 3.4. The design parameters of the MEMS TE energy harvesters.

MEMS TE Harvester Parameters	**Values**
Device dimensions (Area)	1.5 mm x 1.5 mm
Thermocouple Number	16 – 112
Thermocouple Thickness	0.1 μm – 0.7 μm
Thermocouple width (fixed)	10 μm
Spacing between thermocouples (fixed)	10 μm
Insulation layer thickness	0.5 μm – 10 μm
Thermocouple length	80 μm – 400 μm
Heater (Ti) thickness	0.1 μm – 0.5 μm

Note that the insulation layer will also be the diaphragm material, so it should be thick enough to carry the metal thermocouples. If the insulation layer is chosen as SiO2, the thickness should not be too high to prevent high intrinsic stress in the material. Otherwise, the diaphragm will bend or crack while releasing.

The design points where maximum power is obtained are given in Table 3.5.

Table 3.5. The optimized design points of MEMS TE energy harvester at which maximum electrical power can be generated.

MEMS TE Harvester Parameters	**Values**
Device dimensions (Area)	1.5 mm x 1.5 mm
Thermocouple Number	48 – 100
Thermocouple Thickness	0.46 μm – 1.4 μm
Thermocouple width (fixed)	10 μm
Spacing between thermocouples (fixed)	10 μm
Insulation layer thickness	0.5 μm – 1.2 μm
Thermocouple length	237 μm – 390 μm
Heater (Ti) thickness	0.1 μm – 0.5 μm

Note that the thermocouple number has a larger range compared to the other parameters. The reason is that for any thermocouple number, thickness can be optimized to maximize the power.

The thermoelectric mask sets are drawn according to the optimum design parameters. The process steps are also adjusted to reach the desired film thicknesses. There are a total of 7 different designs in the masks excluding the test structures.

3.8 Summary of the Chapter

The design of the MEMS thermoelectric harvesters have been done in order to optimize the electrical power. In order to obtain a high Seebeck voltage, obtaining a significant temperature difference between the hot and cold ends was necessary. First, the temperature profile was calculated with different thermoelectric geometries analytically. Then the calculated results were verified with finite element modeling. The methodology for creating a temperature difference through the thermopile array was defined. The heaters were designed such that enough electrical power can be obtained to characterize the thermoelectric generator through a wide temperature

span. The constraints on the Ti heaters were determined in order to prevent damage to the heaters. Secondly, the Seebeck voltage generated for changing TE parameters was calculated. Lastly, the electrical power calculations have been done and design points where maximum power is generated are selected. The geometric parameters of the TE energy harvester to be fabricated were selected according to optimized parameters. Again, the masks are drawn for the TE device geometries from which the maximum thermoelectric power could be obtained.

CHAPTER 4

FABRICATION PROCESS AND PROTOTYPES

This chapter explains the fabrication process of the TE energy harvesters. The fabrication of MEMS thermoelectric energy harvesters were done using microfabrication techniques. Mostly surface micromachining is used for the processes except the last step. For the fabrication process to initiate, the masks are first drawn with Tanner L-edit. The masks drawn are used to pattern the layers to form the complete MEMS TE harvester. Several thermoelectric generator designs with test structures are included in the masks. All of the designs are made in the same mask set, so the fabrication sequence is common. In Section 4.1, the overall configuration of the thermoelectric harvester is given. In Section 4.2, the test device configuration is given. The general view of all the mask sets overlayed on each other for a full wafer is shown in Section 4.3. In Section 4.4, the fabrication flow is illustrated and all of the microfabrication steps are explained in detail. . In Section 4.5, the fabricated energy harvester structures are presented. Section 4.6 summarizes the chapter.

4.1 Cr-Ni Based Thermoelectric Generators

A sample thermoelectric device is shown in Figure 4.1. The thermoelectric generators consist of Chromium (p) and Nickel (n) metal layers overlaid on suspended diaphragms. These thermocouples are in contact in the hot (middle of the diaphragm) and cold (outer silicon rim) junctions. These thermocouples are added electrically in series to accumulate Seebeck voltage. For testing reasons, Titanium heaters near the hot junctions exist. These heaters provide controlled heating of the hot junctions, so that a known temperature difference is created between the hot and

cold ends of thermopile materials. There are various generator structures with varying thermocouple number, length and width. Specific structures for Seebeck coefficient and thermal conductivity tests are also added in the mask set. Some test structures with very large pads are also designed for testing without wire bonding.

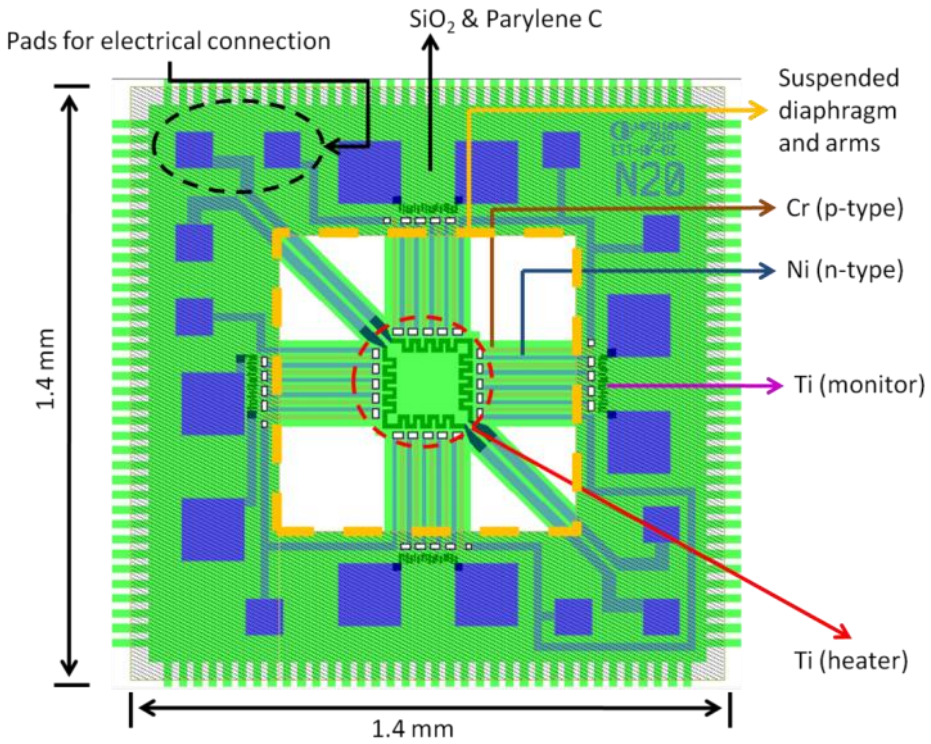

Figure 4.1. One thermoelectric harvester design with device dimensions.

4.2 Test Structures for Testing of Seebeck Coefficient and Thermal Conductivity

Figure 4.2 shows the suspended cantilever structures that are used for testing the Seebeck coefficient and the thermal conductivity of the fabricated structures. Titanium heaters seen in Figure 4.2 are used for monitoring the temperature at the hot and cold junctions accurately [43]. Once the temperature difference, resistance change and voltage are measured between the hot and cold junctions, the characterization of the thermoelectric materials can be done easily.

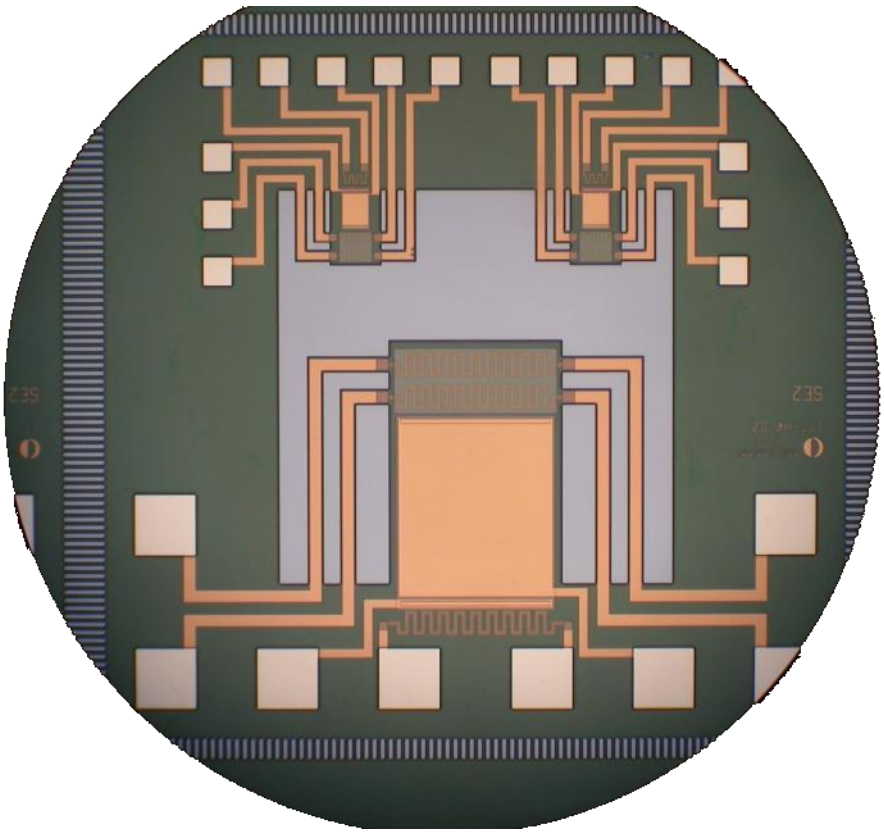

Figure 4.2. Test structures for Seebeck coefficient and thermal conductivity measurement.

4.3 Mask Set of Thermoelectric Generators

The designed mask set contains a total of 978 thermoelectric energy harvester devices and a number of test structures. In the designed TE devices, the number, width, length, and the geometry of the thermocouples are varied. The mask set includes 9 TE harvester designs, test structures and scaled up versions of the designs. The area of the TE energy harvesters vary between 1 mm^2 and 0.81 cm^2. Figure 4.3 shows the layout of the overall mask set that is used for the fabrication of the TE devices. The overall mask set is given in Appendix B.

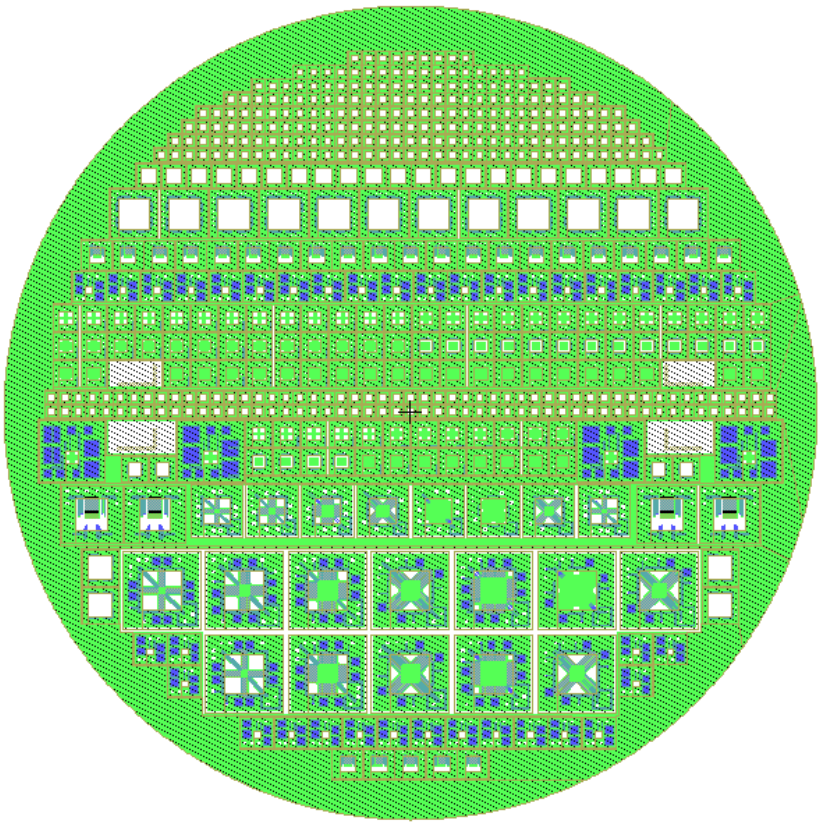

Figure 4.3. Wafer level layout of the thermoelectric generator mask set.

4.4 Fabrication Flow of the Thermoelectric Energy Harvesters

The fabrication process for the formation of MEMS TE energy harvester devices consists of patterning of metal thermocouples and heaters on an insulating layer (Si_3N_4, SiO_2 and Parylene C), patterning a a diaphragm, and a final step of backside DRIE to release the devices. Nickel and Chromium are selected as the thermocouple material, whereas the heaters are formed of Titanium. The diaphragms carrying the thermocouples and heaters are made of Si_3N_4 and/or SiO_2.

Figure 4.4 shows the schematic top view fabrication flow for one of the thermoelectric energy harvester structures. The mask set is designed to be applied on 4'' wafers. Si wafers are employed during the fabrication process due to their anisotropic etch possibility and high thermal conductivity.

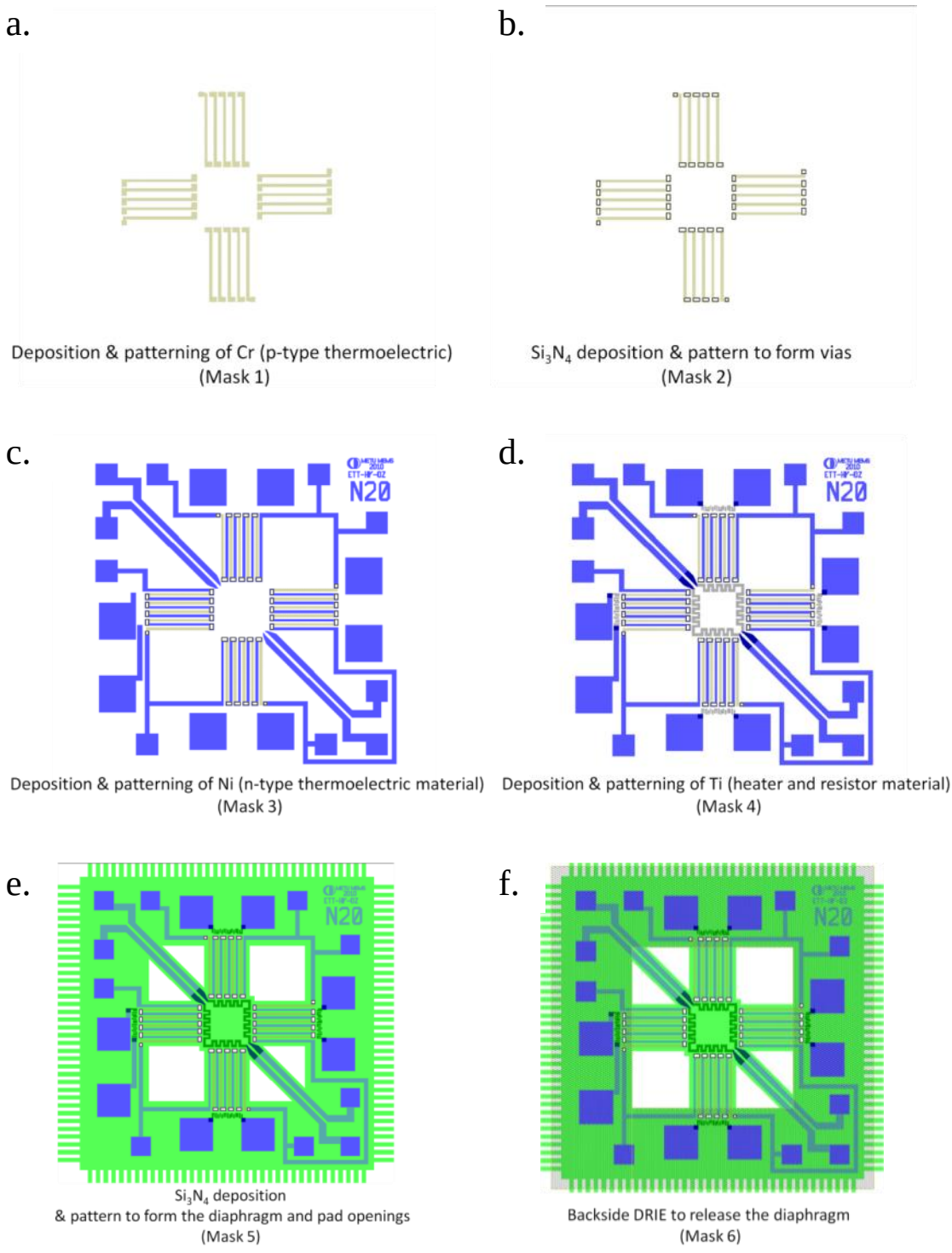

Figure 4.4. Fabrication flow and relative positions of the masks from top view.

The details of the fabrication are explained in Appendix C.

4.4.1 Parylene C as Diaphragm Material

During the design phase of the TE energy harvetsres, the thermocouples were intended to reside on Parylene C diaphragms. However, we have continuously faced an adhesion problem of chromium on Parylene C. The adhesion problem results from its hydrophobicity and chemical structure that do not allow adhesion of some metals [44]. So, surface activation is needed for the chemical modification of the Parylene C surface. Several surface activation processes and different process parameters were attempted to overcome this, but Cr layer delaminated from the parylene C surface in all of the trials. There have been few successful trials with better adhesion, but cracks on the Chromium layer were observed all over the wafer for these cases, leading to open circuit thermocouple resistances. In this section, the details of these trials will be presented.

Firstly, for the surface modification, the parylene C was exposed to 3 minute O_2 plasma descum to roughen the surface. The adhesion after deposition seemed to be good, but the Cr layer peeled off from the surface in the lithography step during the photoresist development.

After this trial, on another sample wafer, surface activation with 60 sccm O_2 flow and 10 sccm N_2 was tried in the Nanoplas O_2 plasma system [44]. After Cr+Au layer deposition, the wafer was tested in water in order to observe the adhesion quality. Again, Cr peeled off from the surface as shown in Figure 4.5.

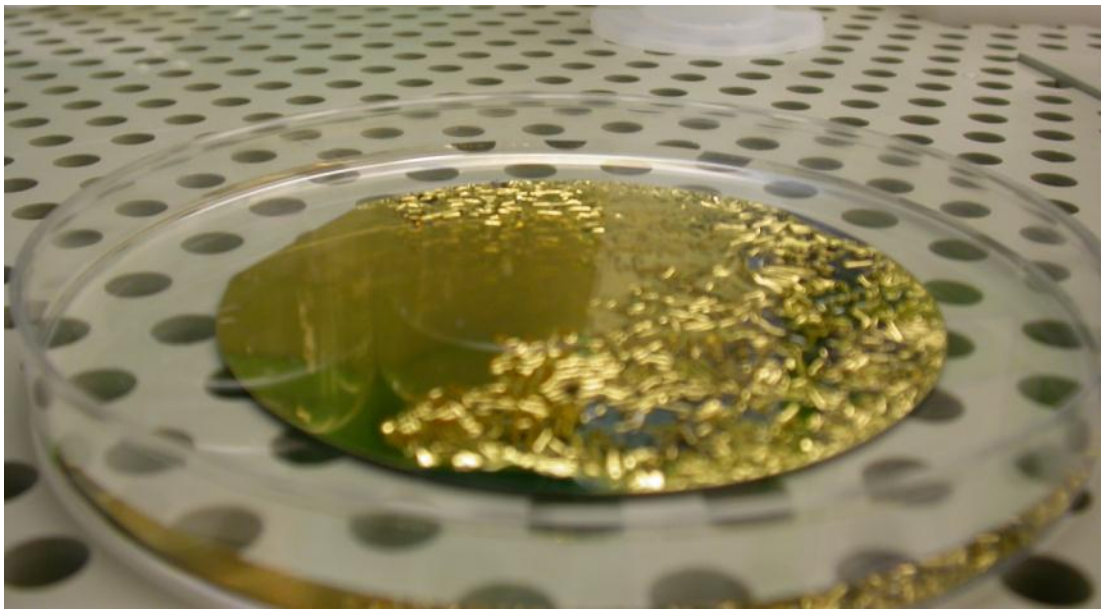

Figure 4.5. Cr+Au peeled off from parylene C surface after O2 plasma treatment.

Lastly, parylene C is annealed in oven at 120°C, as described in [45] to reduce the stress and modify the surface. The Cr was sputtered on annealed parylene C with the same process parameters as before. However, Cr had microcracks after this deposition step. After all these trials, we have decided to abandon using parylene C as the first insulation layer material.

We continued fabrication on some wafers where Cr had microcracks but no peeling-off. Most of the metal layers (Cr) cracked after etching as shown in Figure, and no electrical resistance could be measured. In MEMS fabrication, thermal expansion coefficients of the thin films play an important role as well as surface properties. Using two materials which have a large difference between thermal expansion coefficients is not preferred since this causes excessive stress in one of the layers, mostly in the layer with a lower thermal expansion coefficient [46]. One of the reasons for delamination of Cr layer is most probably the difference between the thermal expansion coefficients of Cr and Parylene C.

a)

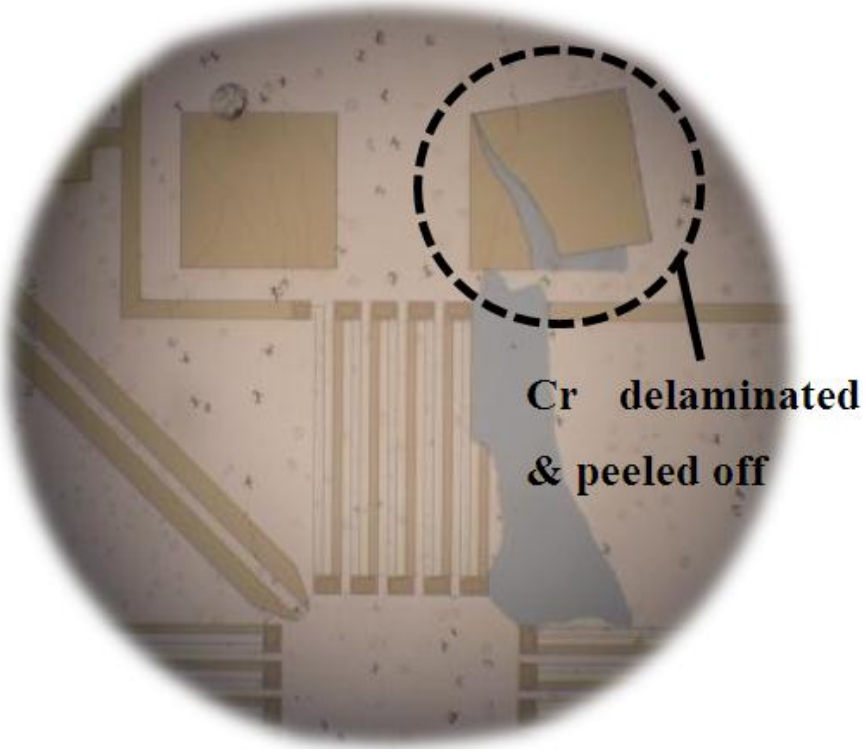

b)

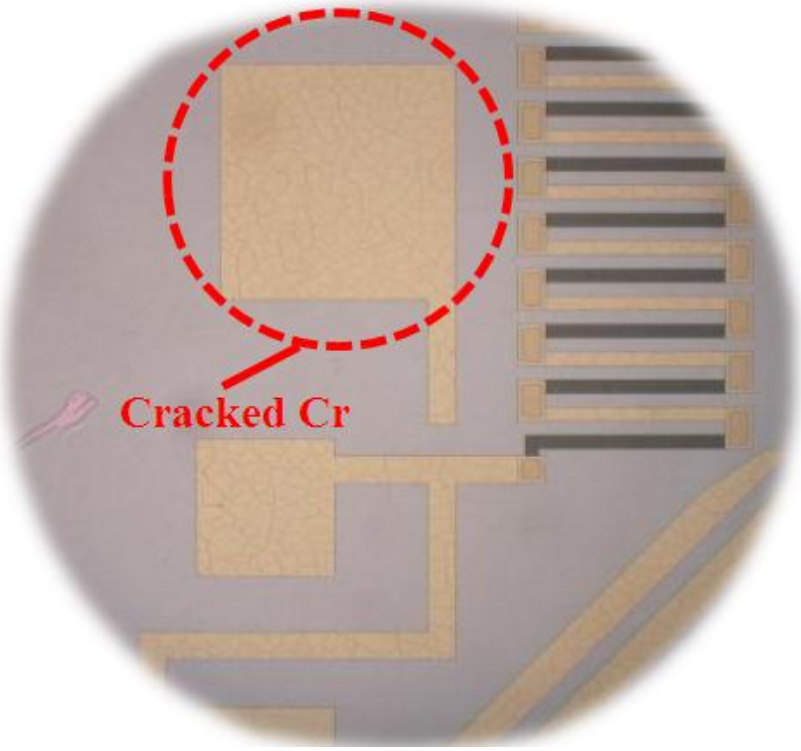

Figure 4.6. Cracked chromium layers after Cr etching. The cracks show that chromium layers delaminated from the Parylene C surface.

c)

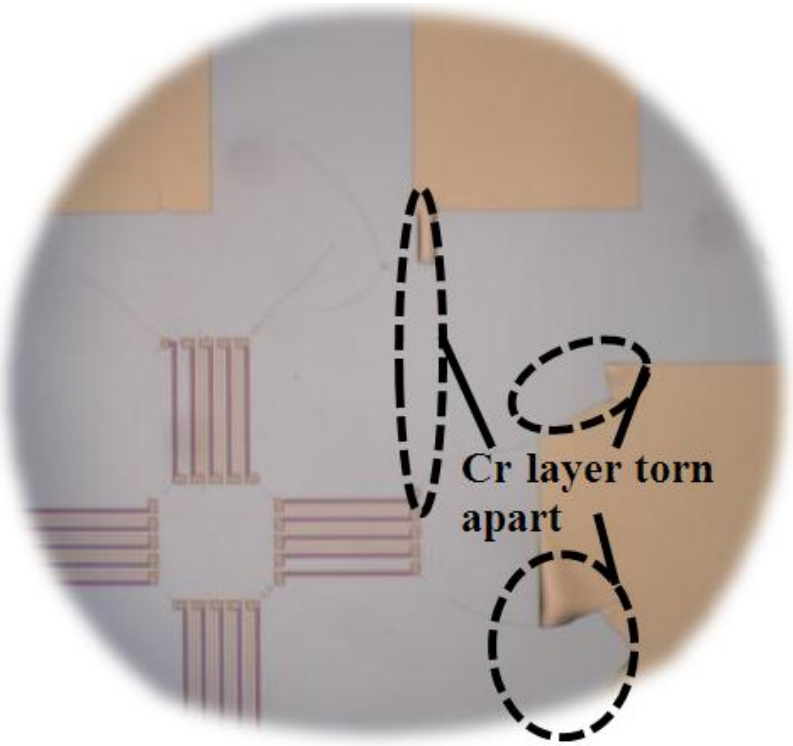

Figure 4.6 continued.

On some wafers, Cr was in a cracked state after deposition. This is due to very high compressive stress of the Cr layer and the huge difference of thermal expansion coefficients between Cr and Parylene C, and adhesion problem to the Parylene C surface. The stress state of the metals thin films was observed in [47]. Figure 4.7 shows the possible topography of the thin films due to the type and magnitude of stress. The structure of Cr film after deposition on surface treated Parylene C (3 min. O_2 descum) is shown in Figure 4.8.

In the light of this information, the stress on Cr layer is observed to be compressive.

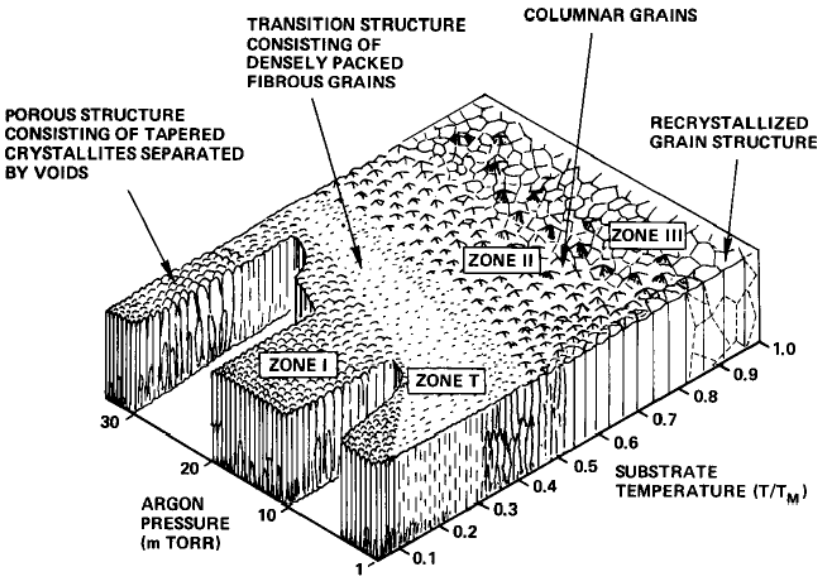

Figure 4.7. The stress state of the thin films regarding the surface morphology. As the structure approaches to 'ZONE III', the thin film structure gets more compacted and the stress is compressive [47].

The cracked grain structure of Cr film after deposition is shown in Figure 4.8.

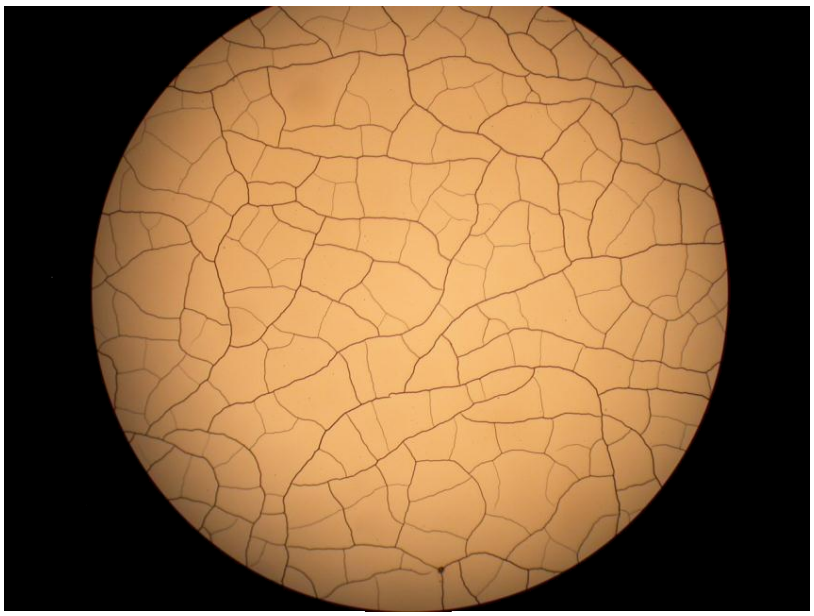

Figure 4.8. The grain structure of chromium sputtered on Parylene C surface is shown.

4.4.2 Fabrication with Si_3N_4 as the Diaphragm Material

After the summarized trials with Parylene C, it is decided to form the diaphragms with Si_3N_4 due to its similar thermal properties when compared to Parylene C. With this modification in the process flow, no cracking of the metal layers have been observed, and a stable resistance reading was achieved from the thermocouples and heaters.

On this section, the fabrication flow of the TE energy harvesters will be explained according to this modification. Table 4.1 gives the complete list of the masks that are used for the fabrication. The whole fabrication consists of 6 masks, which are all fabricated in METU MEMS Center.

Table 4.1. The masks used for the fabrication of thermoelectric energy harvesters.

Mask #	Mask Name	Layout in Figure	Mask Polarity	Layer Material	Process
1	Metal 1 (Cr)	B.1	Clear Field	Chromium	Form the p-type thermolegs
2	Via	B.2	Dark Field	Si_3N_4	Form the via openings for junctions
3	Metal 2 (Ni)	B.3	Clear Field	Nickel	Form the n-type thermolegs
4	Metal 3 (Ti)	B.4	Clear Field	Titanium	Form the heater and monitor resistors
5	Insulation 2	B.5	Clear Field	Si_3N_4	Form the diaphragms
6	Backside DRIE	B.6	Clear Field	Silicon	Release and suspend the diaphragms

The cross section of the fabrication flow is shown in Figure 4.9. Silicon wafers with 0.5 µm thermal SiO_2 were used as the substrate material in the fabrication process (Figure 4.9.a). This oxide layer will later serve as the etch stop in final DRIE etching process.

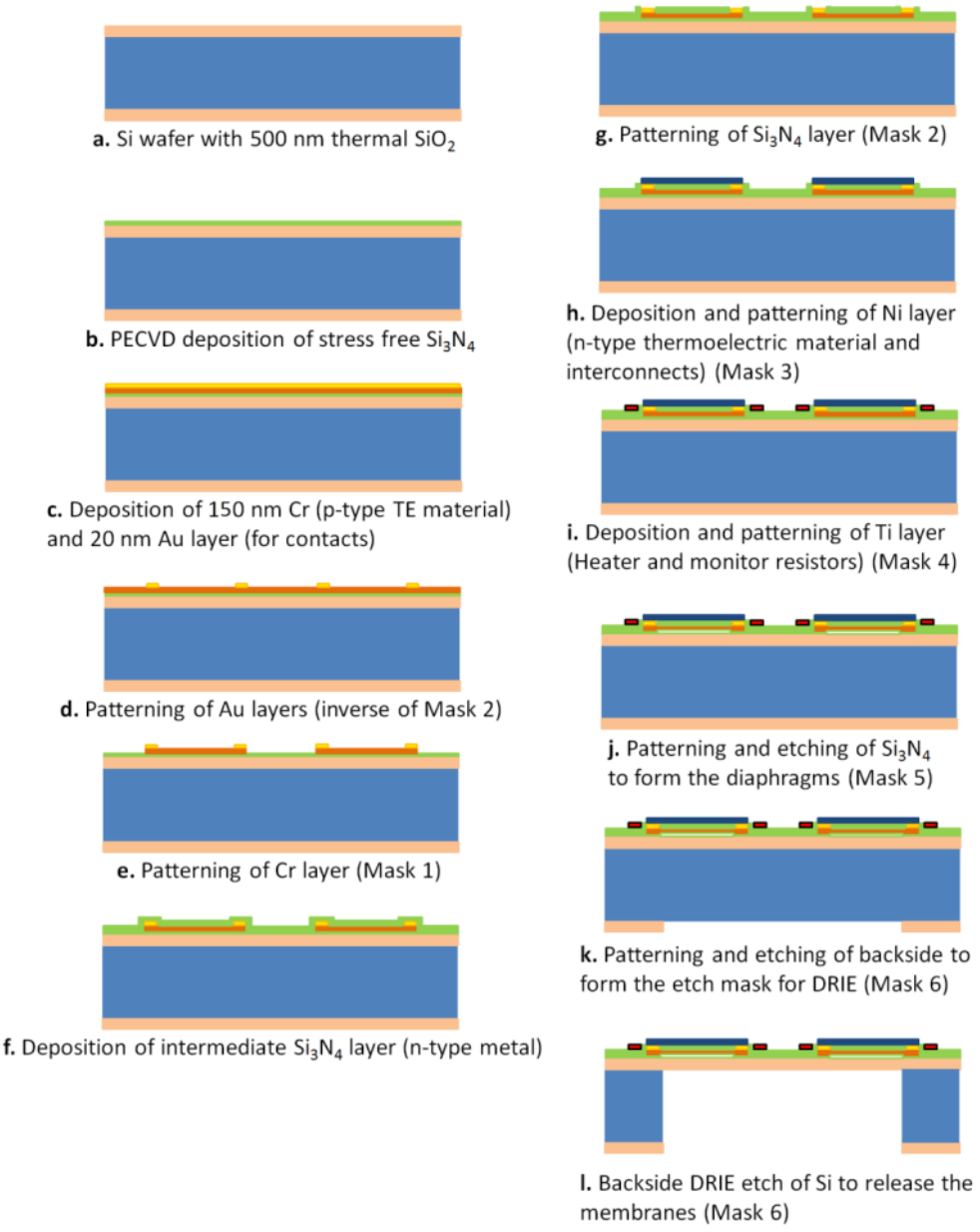

Figure 4.9. Cross section fabrication flow.

Firstly, a previously characterized, stress free Si_3N_4 layer of 0.2 µm thickness was deposited by using PECVD process on top of the SiO_2 layer on the front side of the

wafers (Figure 4.9.b). The next step is the deposition of 0.15 μm Cr layer as the p-type thermoelectric metal. At this point, it should be noted that the selection of the first metal layer is arbitrary in terms of thermoelectric properties; Ni can also be deposited as the first metal layer.

Then, a 20 nm-thick Au layer is deposited in-situ with Cr deposition (Figure 4.9.c). Au is patterned by using the 2nd mask (the via mask between two metal layers) together with an image reversal photoresist, AZ5214E, on the junction areas in order to eliminate possible oxidation problems which may lead to an electrical open circuit across the thermocouples (Figure 4.9.d). Especially for nickel, native oxide begins to form on the surface even in minutes after the deposition step. For one of the wafers, where Nickel is deposited first and Au is not deposited in this step, no metal contacts were formed due to oxidation of the nickel layer. So, it is concluded that it is necessary to use Au at the junction areas. After this Au layer is patterned, Cr is patterned to form the p-type metal of the thermocouples (Figure 4.9.e).

After these steps, another layer of 0.2 μm-thick Si_3N_4 is deposited as an intermediate insulation layer between the metals (Figure 4.9.f). The vias on contact regions are opened with the 2nd mask afterwards (Figure 4.9.g). Once the contact areas are exposed, 0.12 μm of nickel as the 2nd thermoelectric material (n-type) is deposited on top. Then nickel is patterned with Mask 3, and the thermocouples are formed (Figure 4.9.h). The Ni mask also includes the interconnect layer for the Titanium heaters and the pads. On some of the wafers, nickel and 10 nm of Au layer was deposited and patterned together for better electrical connection. The effect of Au layer to the total resistance and the effective Seebeck coefficient is negligible since the deposited thickness is very low when compared to the nickel layer thickness.

After the thermocouples are formed, 150 nm-thick Titanium heater and monitor resistors are deposited and patterned (Figure 4.9.i). The titanium resistors overlap with nickel interconnects at their edges, and outside electrical connection is provided with nickel pads. It should also be noted that no insulator layer is used before this step, hence a via opening mask is not needed due to the compatibility of the Ti etchant with Nickel and Gold. The design of the heaters was done such that resistance of Ti dominates the equivalent resistance where the measurement is done.

By providing Ti heater and monitor resistors, all of the devices can also be used as the test structures.

With these steps, all the resistances serving different purposes are formed. The remaining steps are for forming the suspended diaphragm structures. For these steps, firstly, the diaphragms are formed over the Si_3N_4 layer (5^{th} mask) (Figure 4.9.j). A wet BHF etching process is employed for this step. Underlying SiO_2 is also etched in BHF etching step using DRIE mask (Figure 4.9.k). Then, the formed diaphragms are released by a backside silicon DRIE process, finalizing the fabrication of the TE energy harvesters (Figure 4.9.l). The devices can be separated from each other after this step due to the etching streets placed at the edges of each device cell.

4.5 The Fabricated MEMS TE Energy Harvesters

Figure 4.10 shows the fabricated wafer picture and a close up view of one of the TE devices.

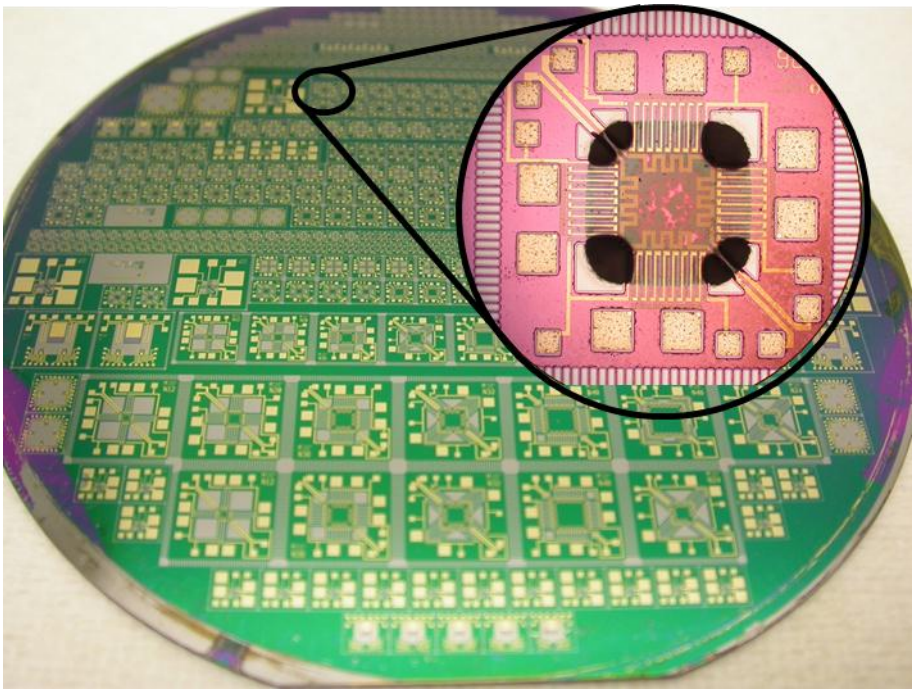

Figure 4.10. The fabricated TE energy harvester full-wafer view and close-up view on one device.

Some problems have been faced during the final step of the fabrication process, where diaphragms are released by a DRIE process, which uses high energy ions to etch silicon. Our diaphragm, made of SiO_2 is used as the etch stop layer as the selectivity of the DRIE process is very high. However, the SiO_2 diaphragm used is very thin (0.5 μm) and some device dimensions are very large (9 mm x 9 mm). So, cracking occurred on most of the diaphragms and the devices on these regions could not survive the DRIE process.

Furthermore, in some devices, the edges of the diaphragm and diaphragm arms burned. Due to high energy ions, the local temperature may be very high during the DRIE process. In some devices, it was observed that SiO_2 and Si_3N_4 could not withstand this high temperature. Especially, the thermocouples and/or the heaters at the edges of the diaphragm arms were damaged, deteriorated or cracked. This resulted in an electrical open circuit, i.e. no resistance could be measured from most of the devices. However, some of the devices survived the DRIE process successfully, and the tests were conducted on these devices. The pictures of some of the wasted devices caused by the explained problems above are presented in Figure 4.11 to Figure 4.14.

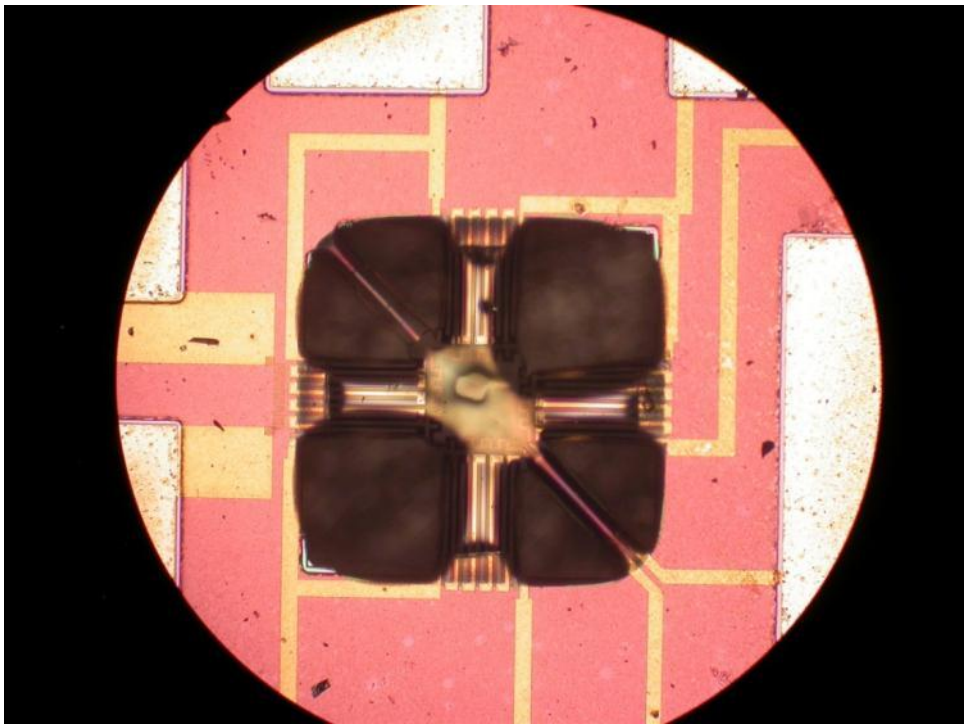

Figure 4.11. A device where thermocouples and Ti heaters are damaged in DRIE process.

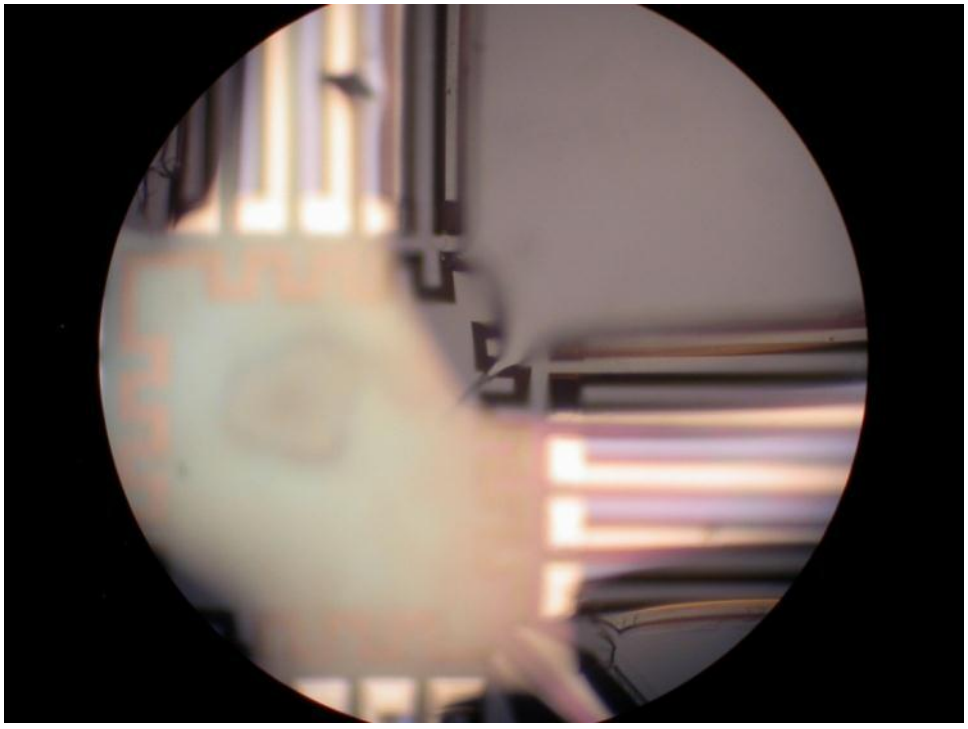

Figure 4.12. A close-up on one damaged Ti heater in DRIE process.

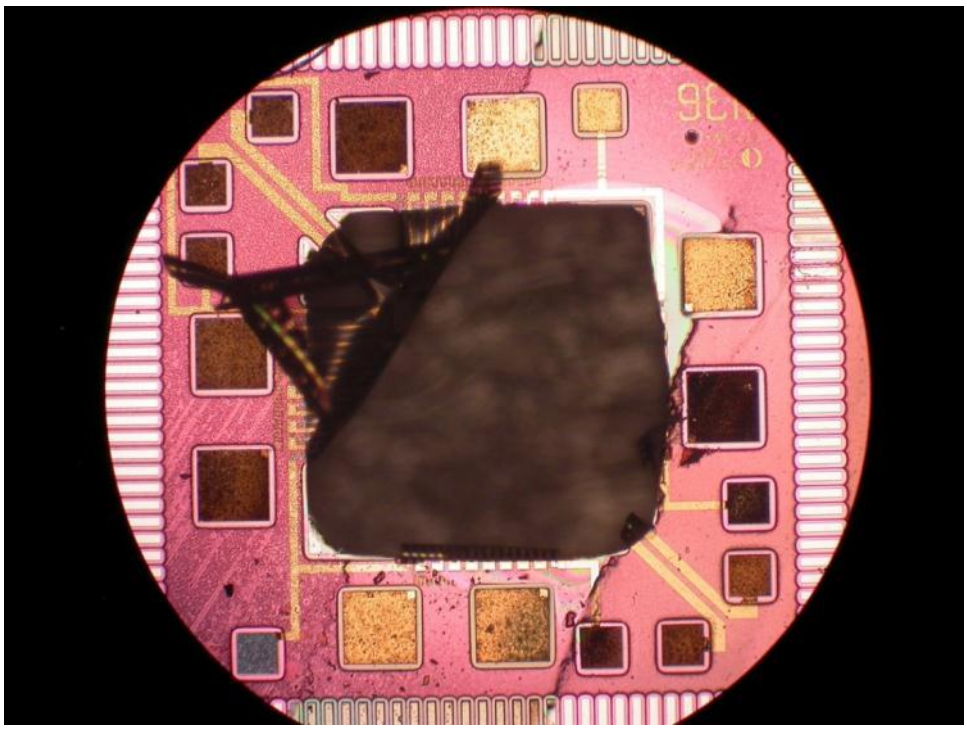

Figure 4.13. Fractured diaphragm due to residual stress on SiO_2 layer.

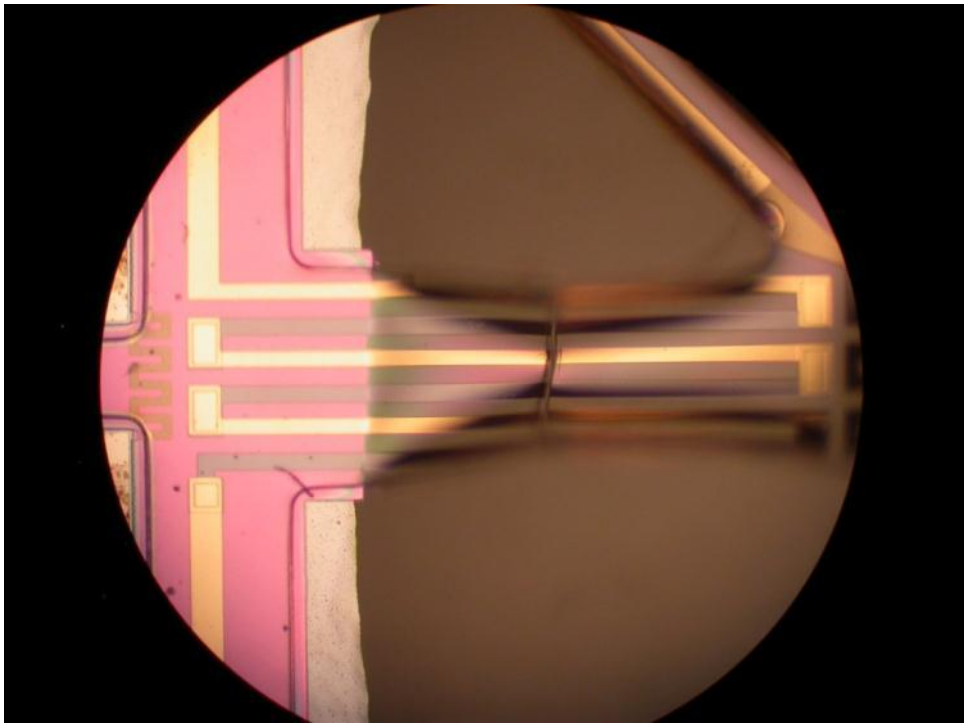

Figure 4.14. Cracked thermocouple metals.

4.6 Conclusion

The MEMS TE harvesters were fabricated using microfabrication technologies. Some problems have been encountered through the process. The initial process was designed to use Parylene C as the diaphragm material. However, an adhesion problem of metals to Parylene C is faced during the first steps. Several methods in the literature have been tried to enhance the adhesion properties, however, these trials have not led to acceptable results. Hence, the diaphragm material had to be changed, and Si_3N_4 has been decided to be used as the diaphragm material. The fabrication process flow is modified according to this selection. The fabrication process was successfully done up to the last DRIE step, where the devices are released from the Si substrates. Most of the devices could not survive this step due to their very large sizes or local overheating problems. Still, some devices have successfully been fabricated, which are suitable for testing and characterization of the structures.

Next chapter is on the testing of the fabricated TE energy harvesting devices.

CHAPTER 5

TEST RESULTS OF THE FABRICATED THERMOELECTRIC ENERGY HARVESTERS

The feasibility of MEMS thermoelectric energy harvesters were discussed in the preceding chapters. The design results with Cr-Ni thermocouples and state of the art thermoelectric materials were presented. As a proof of concept, MEMS thermoelectric energy harvesters utilizing Cr and Ni thermocouples were fabricated. In this chapter, the performance of the Cr-Ni based MEMS thermoelectric energy harvesters is measured and a correlation between the simulation and test results is made. The possible inaccuracies and miscorrelations resulting from fabrication and other factors are discussed.

First, the MEMS structures for testing are introduced. In Section 5.1.1, the necessary components for Seebeck measurements and other tests are explained, followed by the testing procedure in 5.1.2. In Section 5.1.3, the results of the Seebeck voltage and electrical power tests are presented. The MEMS thermoelectric generators were used to drive loads at varying resistances. The power delivered to loads is presented in Section 5.1.4, and part of the thermoelectric conversion theory is proved with experimental results of MEMS thermoelectric energy harvesters. Thermal conductivity derived from the structures and calculations are given in Section 5.1.6. In Section 5.2 an overall discussion of miscorrelations and test results is made and possible integration of state of the art thermoelectric materials is discussed.

5.1 MEMS Thermoelectric Harvester Tests

Fabricated MEMS thermoelectric energy harvesters were tested under the probe station. The tests include heater calibration, Seebeck voltage measurements, generated electrical power measurements and derivation of thermal conductivity through the heat flow path. The comparison of test results with the experimental values is also presented in the related sections.

5.1.1 Test Structures to Measure Seebeck Voltage

The MEMS TE generator structure was explained in Chapter 3 in detail. To test the Seebeck voltage through the thermocouples, a temperature difference should be created between the hot and cold junctions of the thermopile. To obtain a correlation between the temperature difference and Seebeck voltage, the temperature values at these junctions should be determined. Serpentine resistor structures made of Ti were used for heating and monitoring the temperature of the thermocouples. Ti was chosen because its capability to supply higher heating power due to its high resistivity, and its linear TCR behavior. The heater and monitor resistor structures are shown in Figure 5.1.

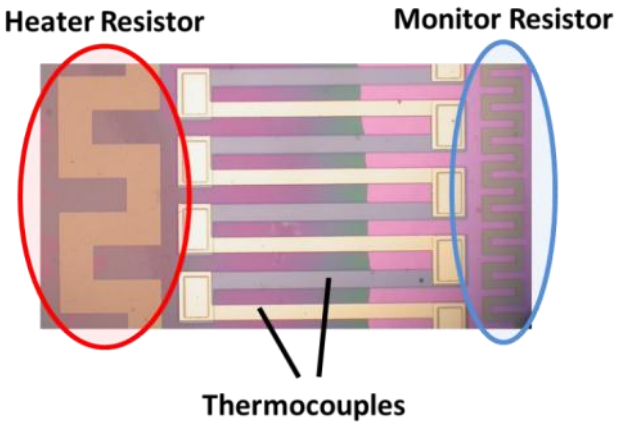

Figure 5.1. The location of Ti heater and monitor resistors are shown. The heaters are at the middle of the diaphragm with 10μm proximity to the hot junction of the thermocouples and the monitor resistors stand at the cold junction on the silicon rim.

To characterize the TCR behavior of Ti heaters, they were heated from 25°C to 110°C , and resistance increase trend was plotted due to temperature increase. Figure 5.2. shows the resistance change of the titanium resistors with varying temperature.

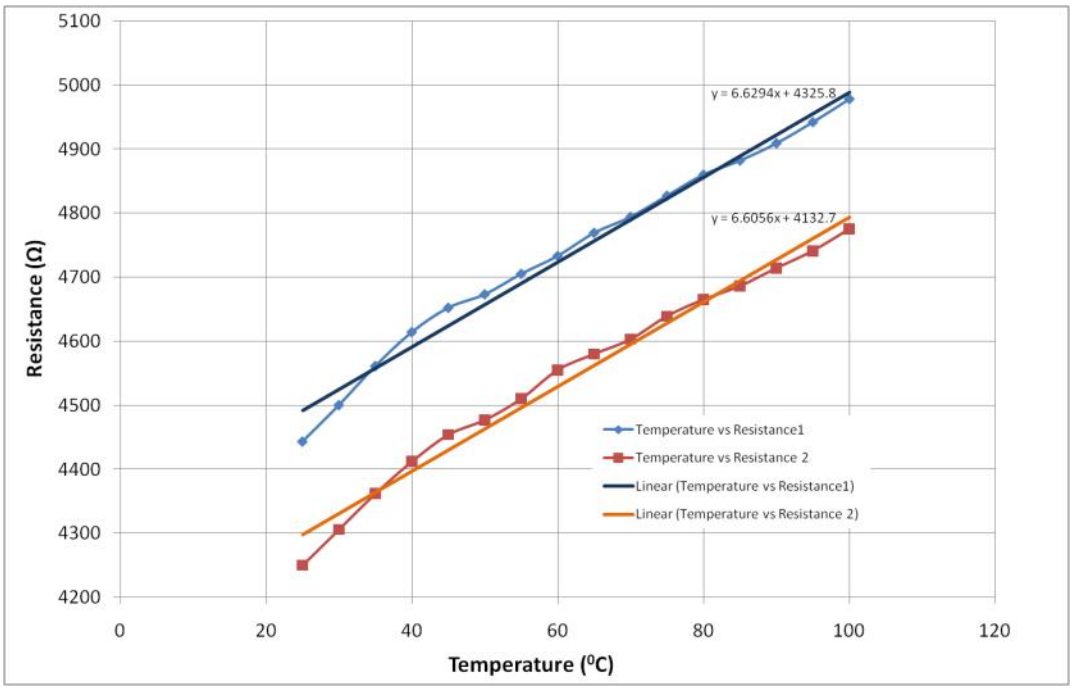

Figure 5.2. The resistance change of the titanium resistors with varying temperature.

The formulation for calculation of the temperature coefficient of resistance is shown in Equation (5.1).

$$\alpha = \frac{\frac{R_T}{R_0} - 1}{T - T_0} \tag{5.1}$$

Where R_T is the resistance measured at the specified temperature T, R_0 is the initial resistance of the resistor, T_0 is the reference temperature of the resistor, and α is the temperature coefficient of resistivity (TCR) of the resistor material. α is mostly unitless or expressed by percentage. There is not a single α value for a material used especially in thin films, because the characteristics strongly depend on the deposition conditions and parameters. Thus, the best way to determine the TCR value of the heater material used is by measuring it. The reported values of TCR for Ti vary between 0.14 and 0.26 [48], [49], which would make a lot of difference in the

temperature measurements. Using Equation (5.1) and the measurement results, the average TCR value for the titanium heaters is calculated as %0.15 ($1.5x10^{-3}$).

5.1.2 Method for Supplying Heat for Seebeck Voltage Measurement

All the tests were performed under the probe station. A current supply (Keithley) for supplying heating current to Ti resistors, two multimeters for measuring the resistance of the monitor resistor and voltage response of the thermopile on the arms were used. The current supply was also used for measuring the potential created through the pads of the heater resistor, supplying the resistance information at each electrical current value. The details of the measurement are given in the following sections. The test setup is shown in Figure 5.3.

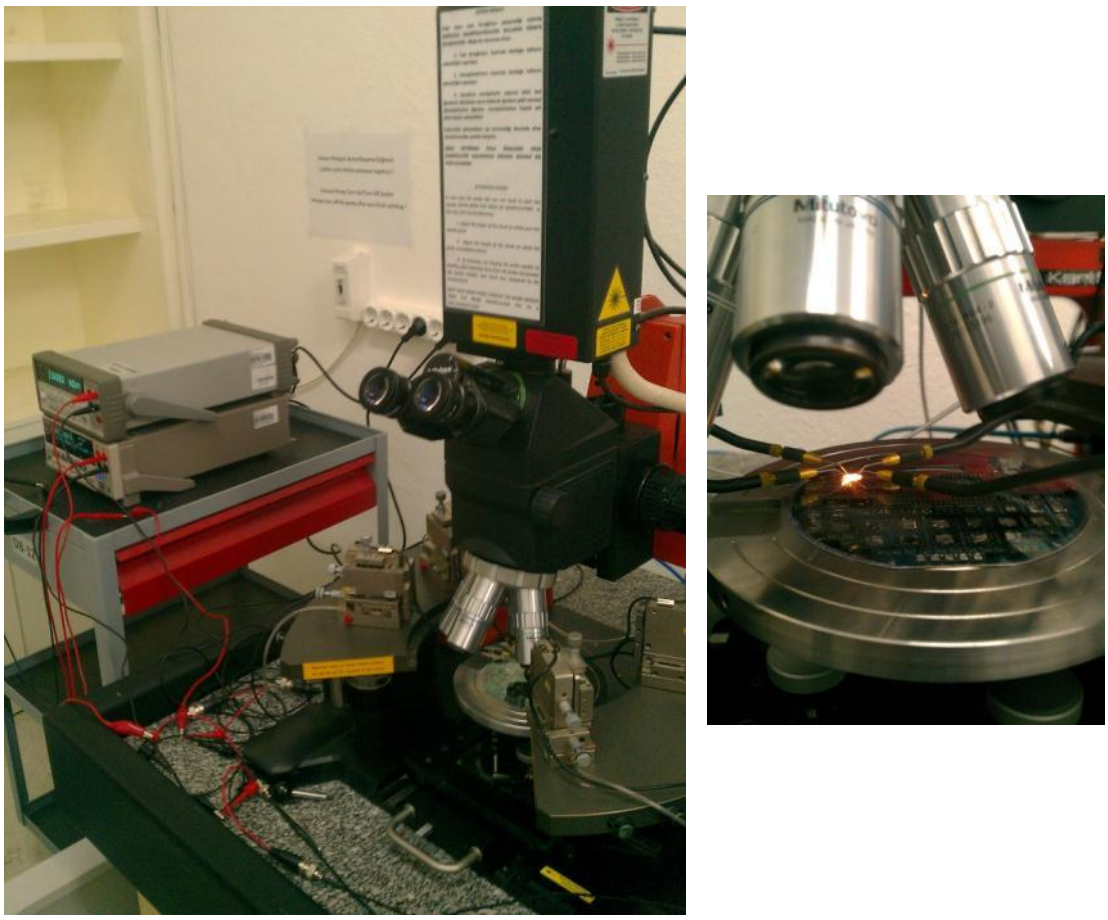

Figure 5.3. The test setup used for MEMS TE energy harvester performance measurement in steady state.

For the transient tests, an oscilloscope is also needed for measuring the transient response of the thermoelectric generator. The test setup for the transient tests is shown in Figure 5.4.

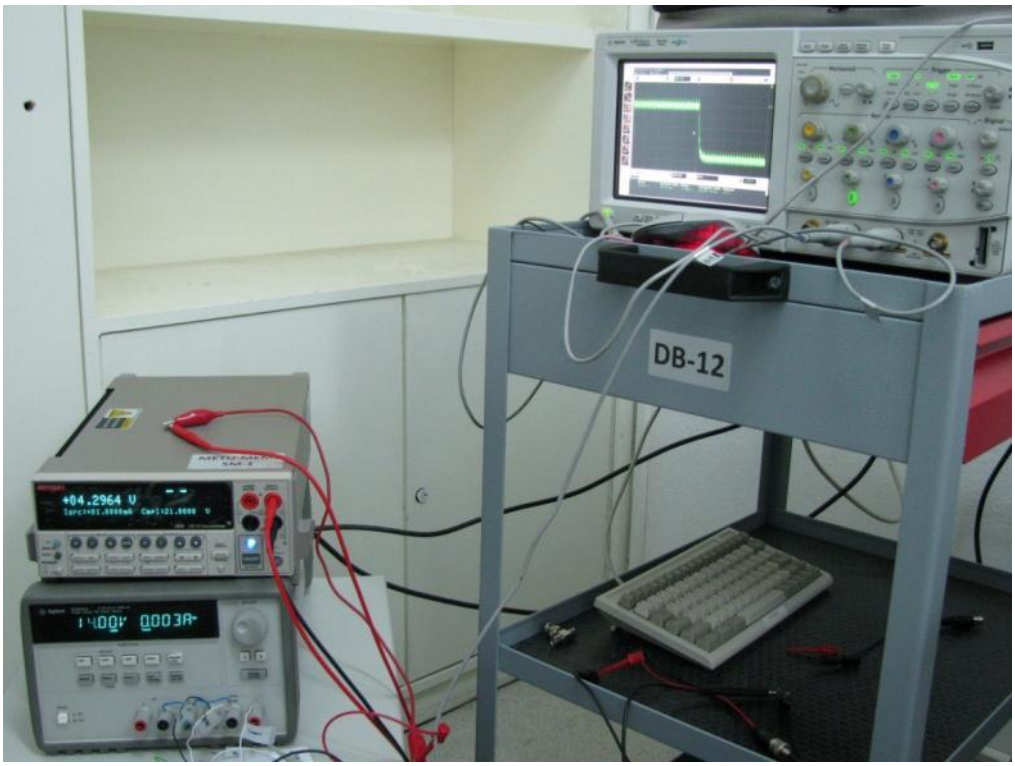

Figure 5.4. The test setup used for transient measurements of MEMS TE energy harvester.

5.1.3 Seebeck Voltage Measurements

For heating the hot junction of the Cr-Ni thermocouples, DC current was given to the heaters. The current is varied between 25 μA and 3.75 mA. At larger current values, the resistors overheat and burn eventually. The heating power supplied to the heaters is shown in Equation (5.2).

$$P_{heater} = I^2 R_{heater} \tag{5.2}$$

The thermocouples reside on the heat flow path, and 1-D heat conduction can be assumed. The heating power is delivered to the hot junction of the thermocouples. The resistance values of the heater and monitor resistors were simultaneously

measured and recorded. Using the TCR value of Ti deposited, the exact temperature increase at the hot and cold junction is recorded. By this method, the temperature gradient between the hot and cold junctions of the thermopile array can be known. The heater structure and thermopile array is seen in Figure 5.5.

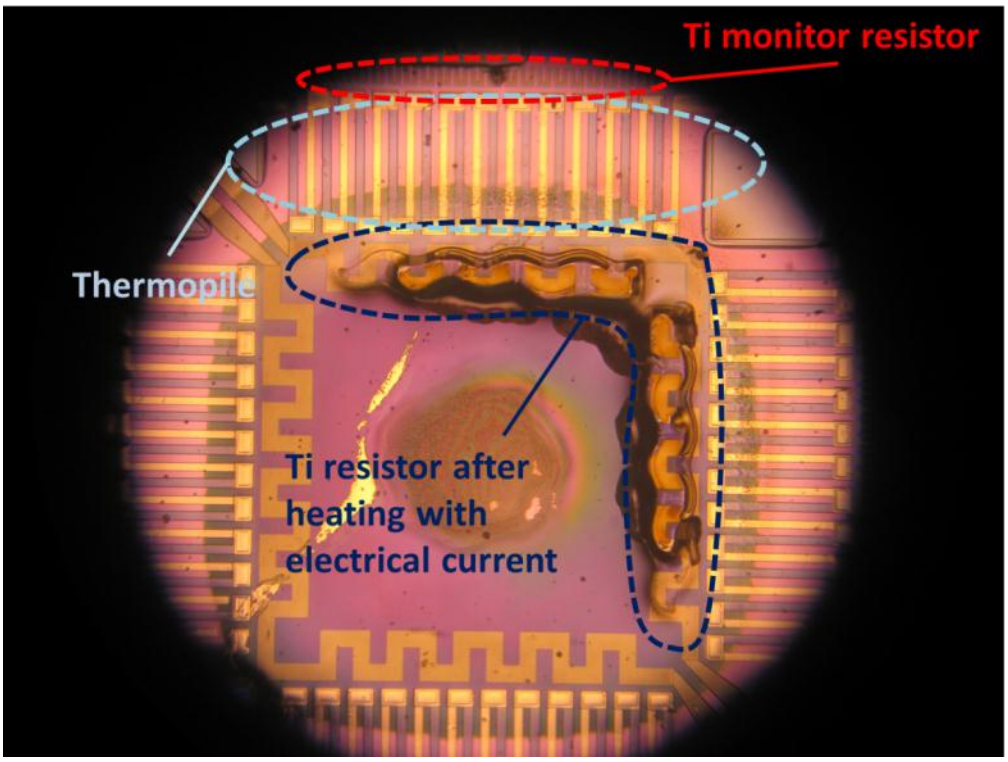

Figure 5.5. The thermally stressed heater resistor after the tests, thermopile array and monitor resistor.

As it can be seen in Figure 5.5, as the electrical current increases the heaters are thermally stressed and begin to burn.

At different DC current values, the Seebeck voltage was measured from the pads connected to thermopile array at the same time. The Seebeck voltage is shown by Equation (5.3).

$$V = n\alpha\,\Delta T \tag{5.3}$$

It was stated in Chapter 4 that few of the devices survived the DRIE release process. Most of the devices were either cracked, torn down or burnt from the diaphragm edges.

The Seebeck voltage generated from four of the devices and a comparison with the simulation results are shown in Figure 5.6 to Figure 5.9.

The operation of MEMS TE Energy harvesters will be within 25°C and 80°C range for practical applications. In real applications like energy harvesting from human body heat and energy harvesting in mobile systems, ΔT varies from a few Kelvins to 60 K [50], [51]. The voltage generation of Cr-Ni based MEMS TE energy harvesters for the ΔT range in question is shown in Figure 5.6 to Figure 5.9.

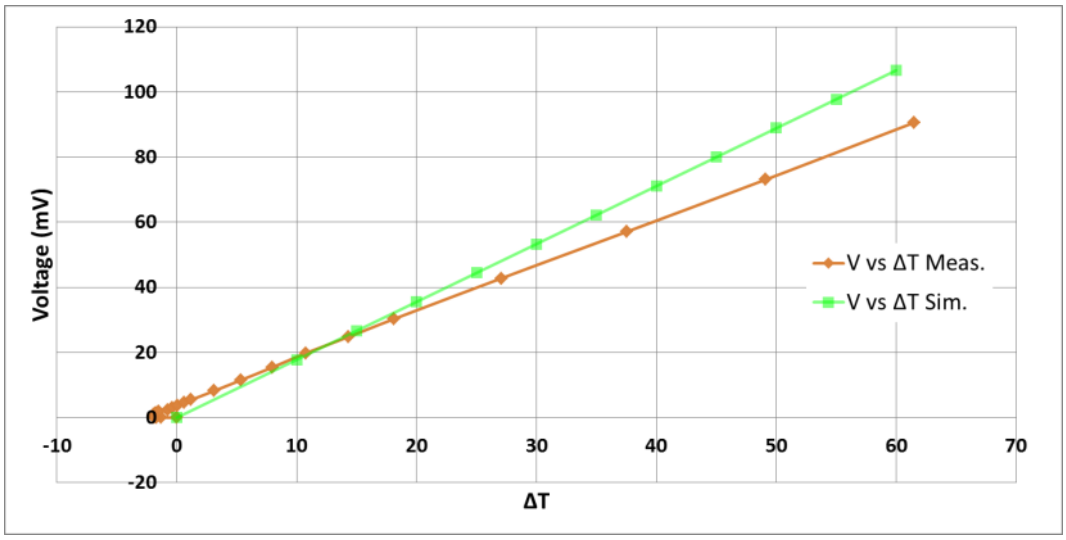

Figure 5.6. The Seebeck voltage with varying ΔT for 1st TE device.

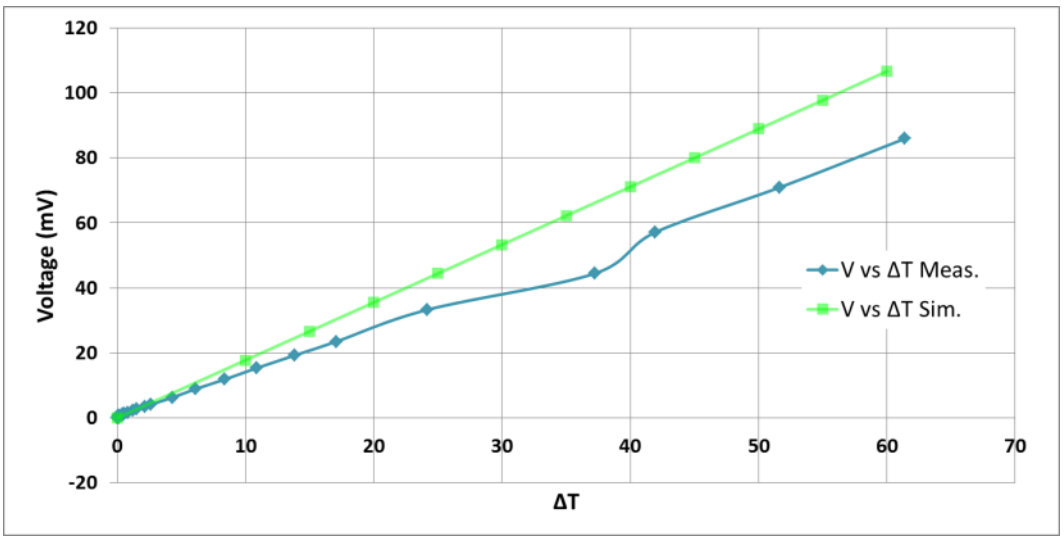

Figure 5.7. The Seebeck voltage with varying ΔT for 2nd TE device.

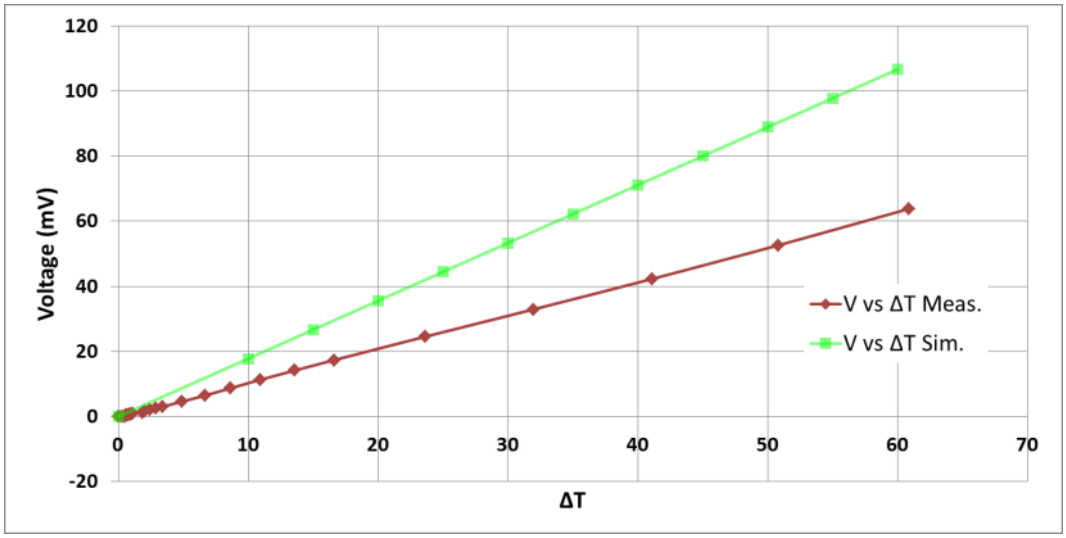

Figure 5.8. The Seebeck voltage with varying ΔT for 3rd TE device.

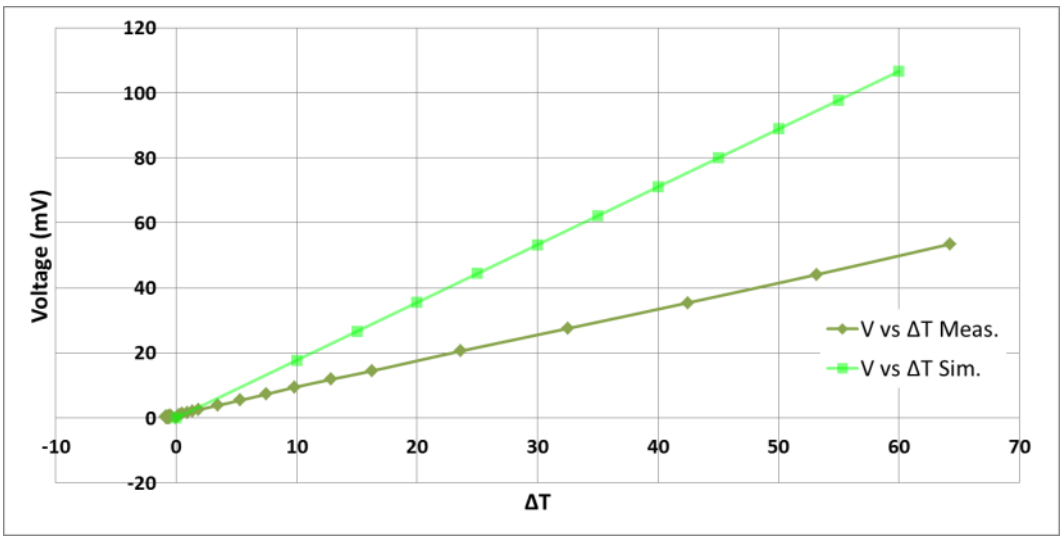

Figure 5.9. The Seebeck voltage with varying ΔT for 4th TE device.

Note that the performance of the TE devices varies dramatically. Theoretically, the identical devices should give similar amount of voltages. The major cause for the results is the DRIE etching non-uniformity. In Section 2.2.1, it was strongly expressed that the thermal conductance of the diaphragm strongly affects the ΔT generated between the hot and cold junctions. The DRIE was used to completely etch the Si underneath the SiO2 diaphragm and suspend the structure. By this way, the diaphragm would be ideally isolated. However, Si does not etch uniformly in DRIE process. The non-uniformity shows up in wafer level as well as device level. The DRIE etch starts from the perimeter of the wafer. So, backside Si is firstly etched on the devices located on the perimeter. That's why Si was not fully etched on devices located in the middle of the wafer. The etch non-uniformity is also observed in device level. For example for most of the devices, some Si remains near the cold junction region. The problem is shown on fabricated devices in Figure 5.10 to Figure 5.12. The Si remaining under the diaphragm arms greatly increases the thermal conductance through the heat flow path due to Equation (2.27). This results in a dramatic decrease in ΔT created between the hot and cold junctions of the thermopile. Apart from materials selected, the Seebeck voltage mostly depends on ΔT. Hence, Seebeck voltage decreases with a decrease in ΔT.

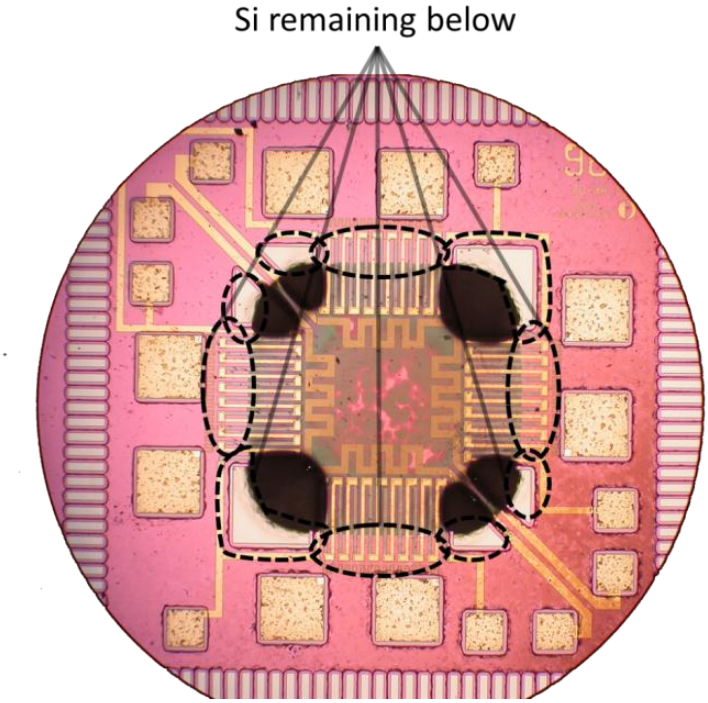

Figure 5.10. Underlying Si remaining seen from the top side of the wafer.

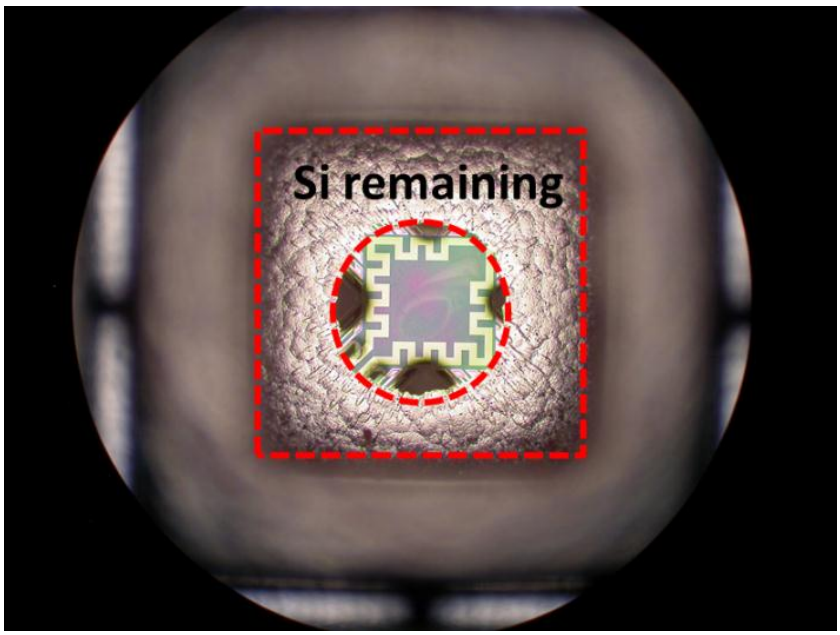

Figure 5.11. Si remaining under the arms of the membrane (Bottom view).

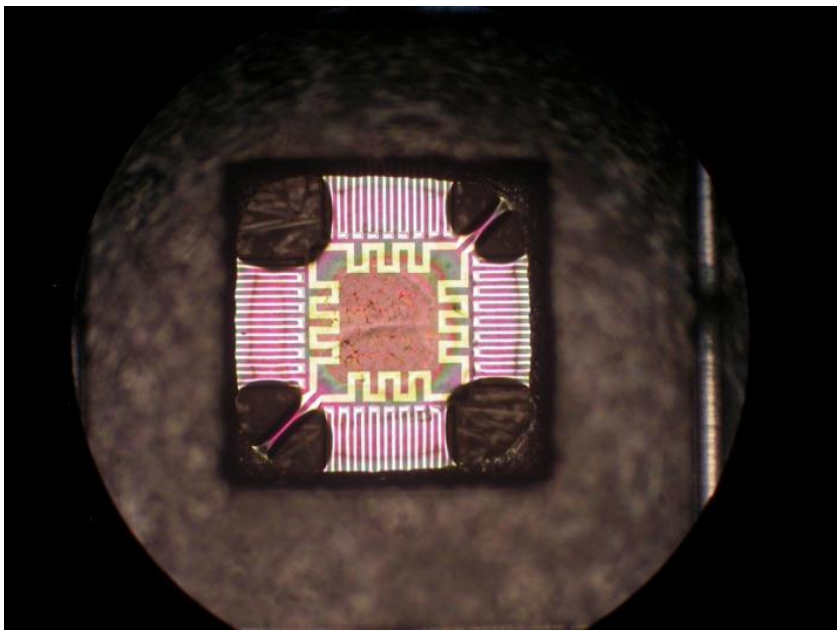

Figure 5.12. A suspended membrane where almost all of the underlying Si is etched (Bottom view).

The voltage measured varies between 9.2 and 17 mV on a 2mm x 2mm device for 10 K temperature difference supplied at the hot junction. With Cr and Ni thermocouples, 1.875 V voltage and ~20 μW power can be obtained on 1cm^2 area with a temperature difference of 50 K, which is the common ΔT on a mobile system processor. Cr and Ni are limited in terms of Seebeck coefficient. Using high Seebeck coefficient materials like doped polysilicon or silicon, much higher voltages can be generated with the same conditions. The energy conversion area can be increased by thermally coupling the hot surface to a thin heat spreader.

The silicon remaining under the diaphragms of some devices was etched in TMAH. First, native oxide on Si was removed by 5 % buffered HF solution. Then the devices were incubated in TMAH solution at 80 °C between 15-40 minutes to etch the remaining bulk silicon. Figure 5.13 shows the TE chips before and after TMAH etching. It is obvious from the figures that a great amount of Si was removed and the area of suspended regions was significantly increased. However, because of residual stress after etching, no resistance could be measured from the thermocouples. SiO2 diaphragms were deformed partially, breaking the thermocouples and leading to open circuit.

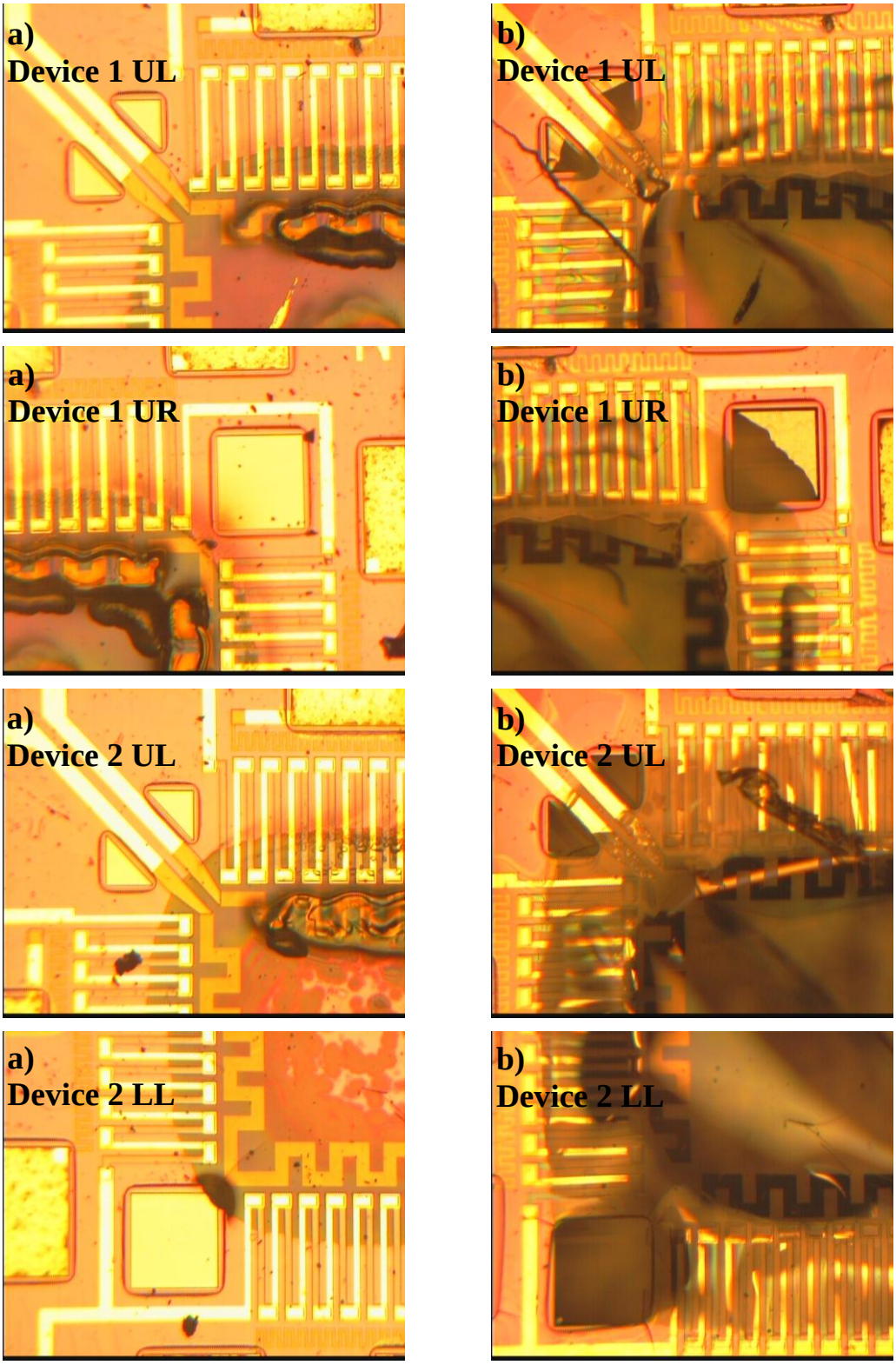

Figure 5.13. The thermoelectric chips a) before b) after TMAH etching. The regions of the devices seen are depicted by abbreviations UL: upper-left, UR: upper-right, LL: lower left.

The average Seebeck coefficient for one Cr-Ni thermocouple is extracted from the voltage measurements. At low heating values, the error can be very large. So, the calculations are done in regions where the measurements are in a steady regime. For the first two devices, the average Seebeck coefficients are shown in Figure 5.14 and Figure 5.15.

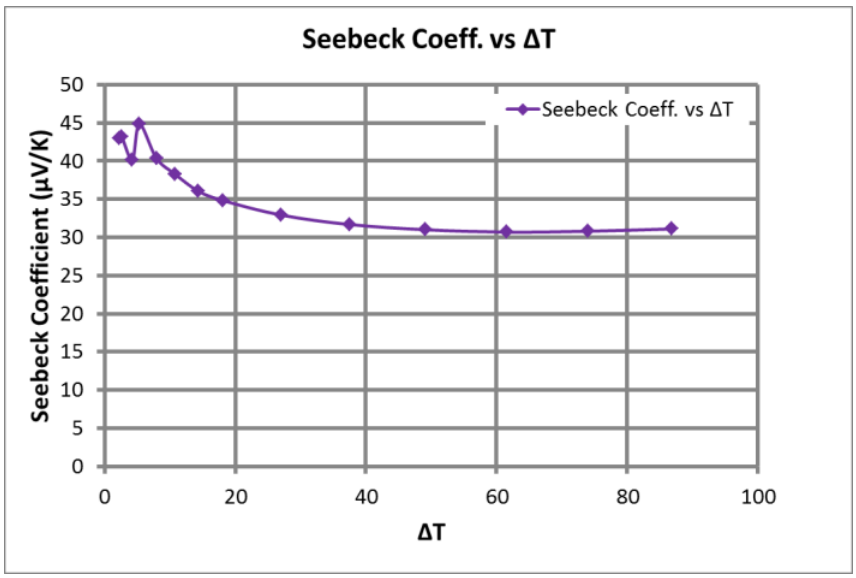

Figure 5.14. The variation of Seebeck coefficient of one thermocouple with ΔT for the 1st device.

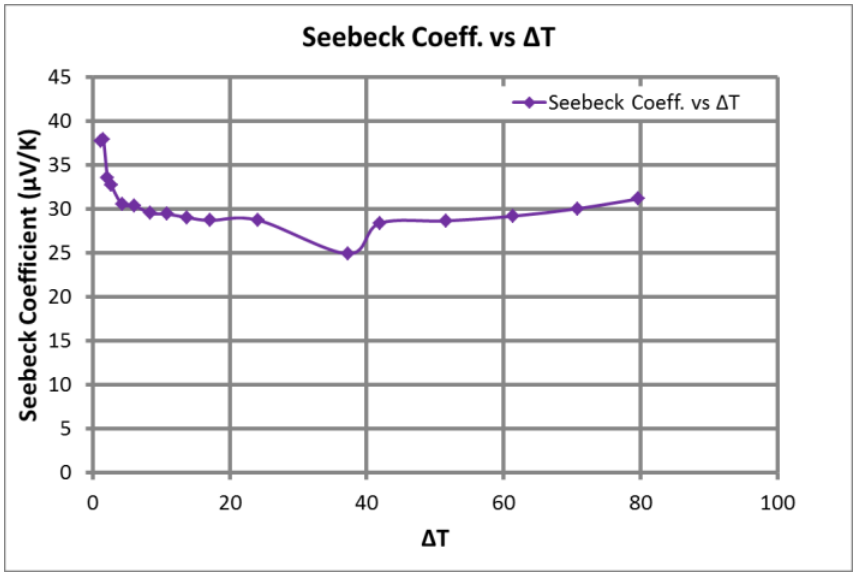

Figure 5.15. The variation of Seebeck coefficient of one thermocouple with ΔT for the 2nd device.

As it can be understood from the following figures, the average Seebeck coefficient of one thermocouple is between 30 and 35 μV/K. The expected value for one thermocouple was 40.5 μV/K. The measured values are very close to the estimated ones.

5.1.4 Generated Electrical Power

The energy input to MEMS TE generator will be the waste heat created in mobile systems. Since there is not a limitation on the input material used (like in combustion thermoelectric generators) it is safe to assume that the input power is virtually unlimited. For this case, we should design our system for maximum power. Theoretically, the maximum power is generated when the resistance of the electrical load driven is equal to the thermoelectric device internal resistance. The power in this case is shown in Equation (5.4).

$$P_{load} = I_{load}^2 \cdot R_{load} \tag{5.4}$$

When load resistance R_{load} is equal to the thermocouple resistance R_{TC}, the current resulting from Seebeck voltage will be divided into two and the maximum power delivered to the load is expressed by Equation (5.5).

$$P_{load} = \frac{V_{load}^2}{R_{load}} = \frac{V_{OC}^2}{4R_{load}} \tag{5.5}$$

Where V_{load} is the voltage on the load resistance, and V_{OC} is the open circuit Seebeck voltage.

Assuming a matched load resistance with the thermocouples, power generated from different devices are shown in Figure 5.16 to Figure 5.19.

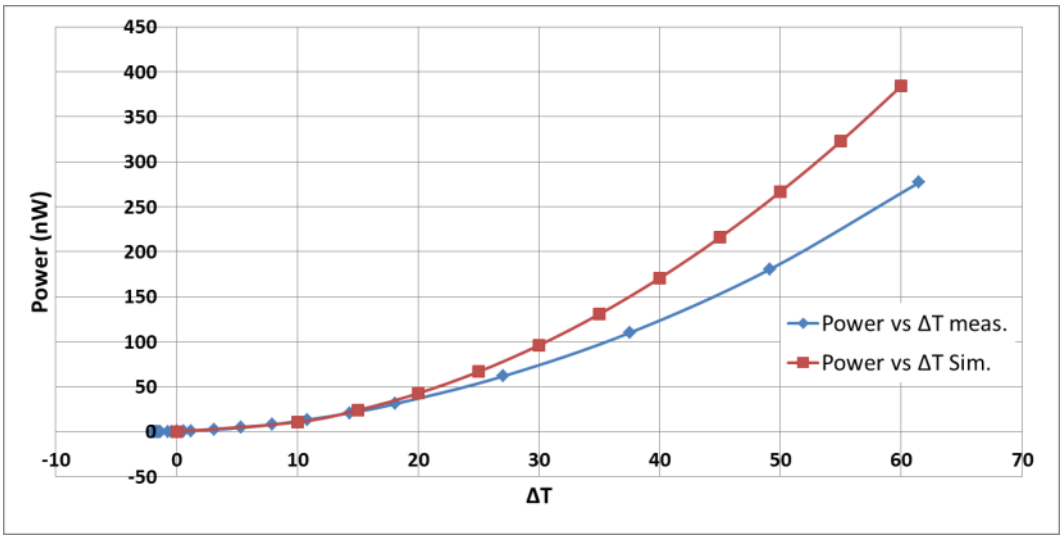

Figure 5.16. The electrical power with varying ΔT for 1st TE device.

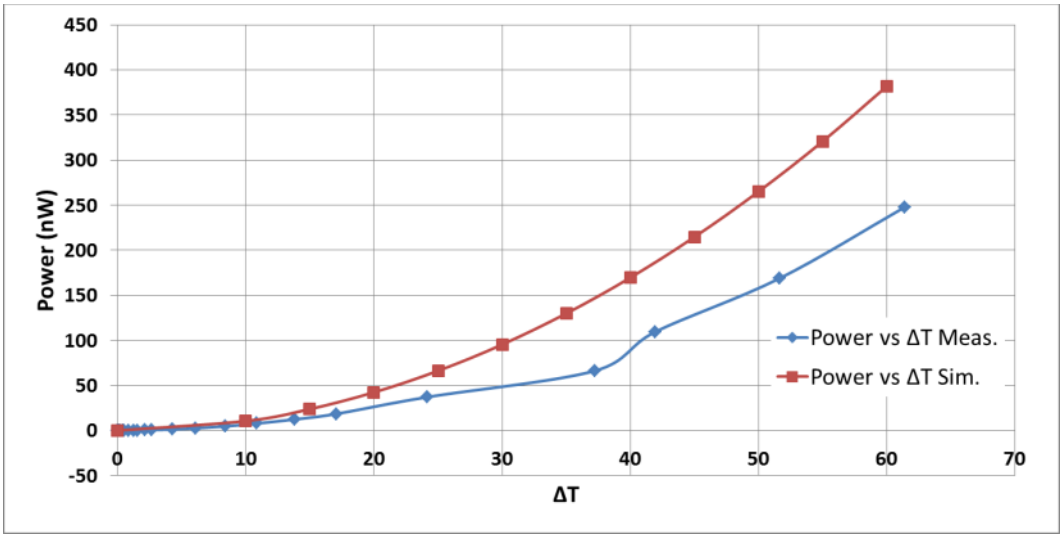

Figure 5.17. The electrical power with varying ΔT for 2nd TE device.

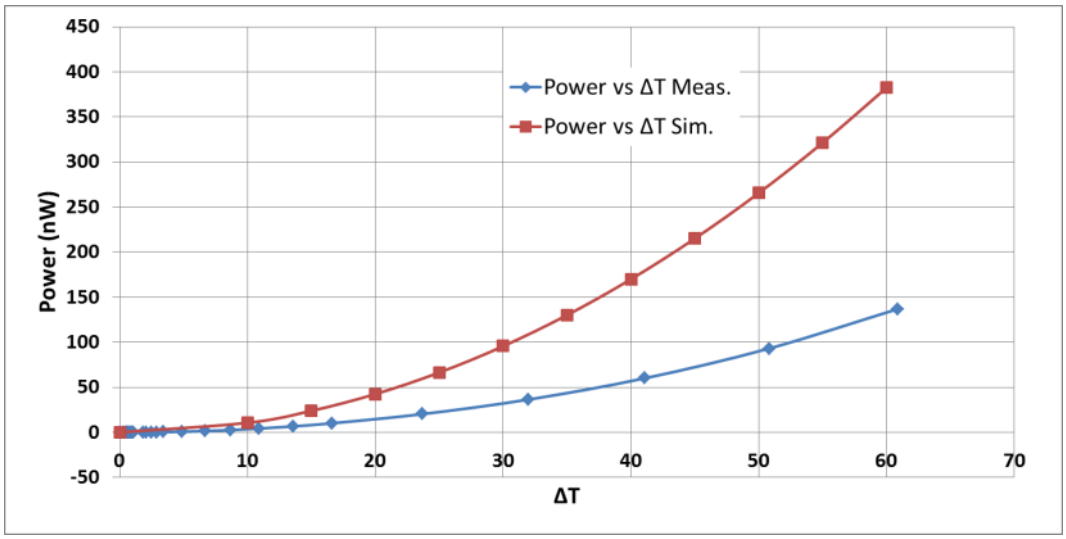

Figure 5.18. The electrical power with varying ΔT for 3rd TE device.

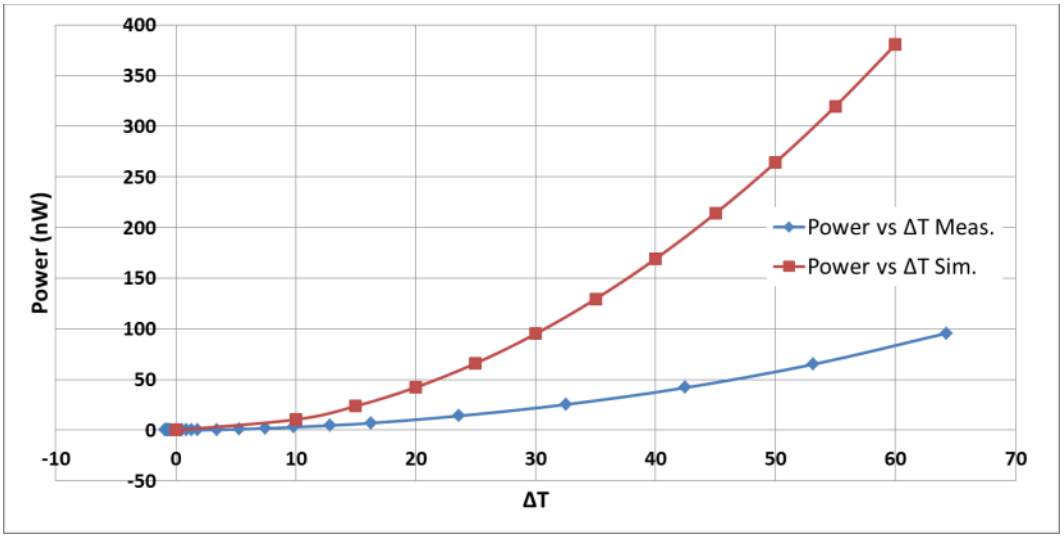

Figure 5.19. The electrical power with varying ΔT for 4th TE device.

To verify the maximum power generation at matched load resistance, different electrical loads were driven with the devices. The result for one device having 48 thermocouples and 3735 ohm electrical resistance is presented. Where ΔT is 13K, the power rating measured with varying load is plotted in Figure 5.20.

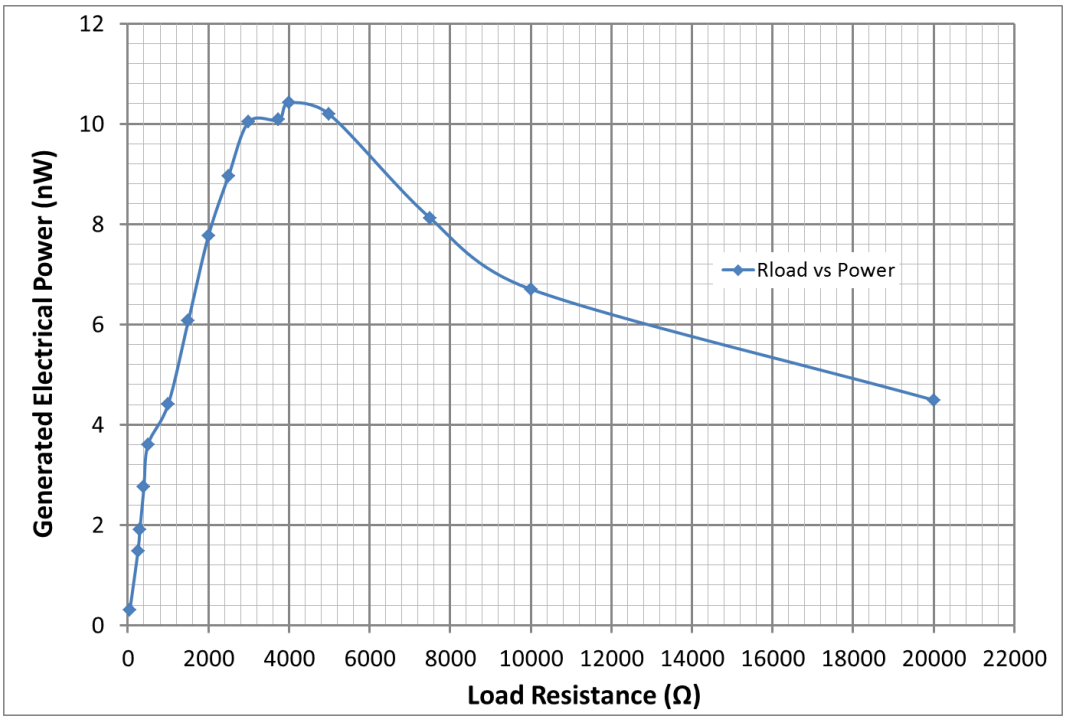

Figure 5.20. The electrical power generated with electrical loads having different resistances.

The conducted tests show that maximum electrical power is generated at load levels equal to or around the thermoelectric internal resistance value. Ideally, the maximum power is expected to be seen at load resistance equal to internal thermopile resistance (Recall (2.28)). However, there is a small deviation from the exact thermocouple resistance where maximum power occurs. In heat sink limited thermoelectric harvesters, the actual current through the thermopiles is somewhat lower than the ideal case. Similarly, the actual load resistance where the maximum power obtained is slightly higher than the ideal case [52]. In reality, there are heat losses, losses from electrical interconnects, thermal and electrical contact resistances that cause the optimum load resistance higher than the ideal case. Another conclusion can be made that driving larger resistances is more preferable since the power generated decreases dramatically at lower load resistances. The load resistance was increased up to 6 times the internal resistance, but the electrical power decreased around 50%. However, power delivered to loads below 500 Ω is below %40 of the maximum deliverable power. In the 2500 ohms – 7500 ohms range the power delivered is nearly %90 of the maximum power.

5.1.5 MEMS TE Harvester Transient Tests

The transient tests for MEMS TE generators have been conducted to evaluate the time response to heating. For the tests, a current source, an amplifier (with 500 gain) and Agilent Infinium scope was used. There was a significant 50 Hz noise in the setup, but it could be reduced to a degree by refining the setup. At low heating values, the thermopile voltage is in the range of microvolts and overwhelmed by noise. For low Seebeck voltages, post-processing and averaging of the data was applied in MATLAB. At significant ΔT values, the Seebeck voltage overwhelmed the noise and the response could be easily seen from the plots. The time response of the structures to heating is between 57 and 75 ms. The transient response of one thermoelectric device to heating is shown in Figure 5.21.

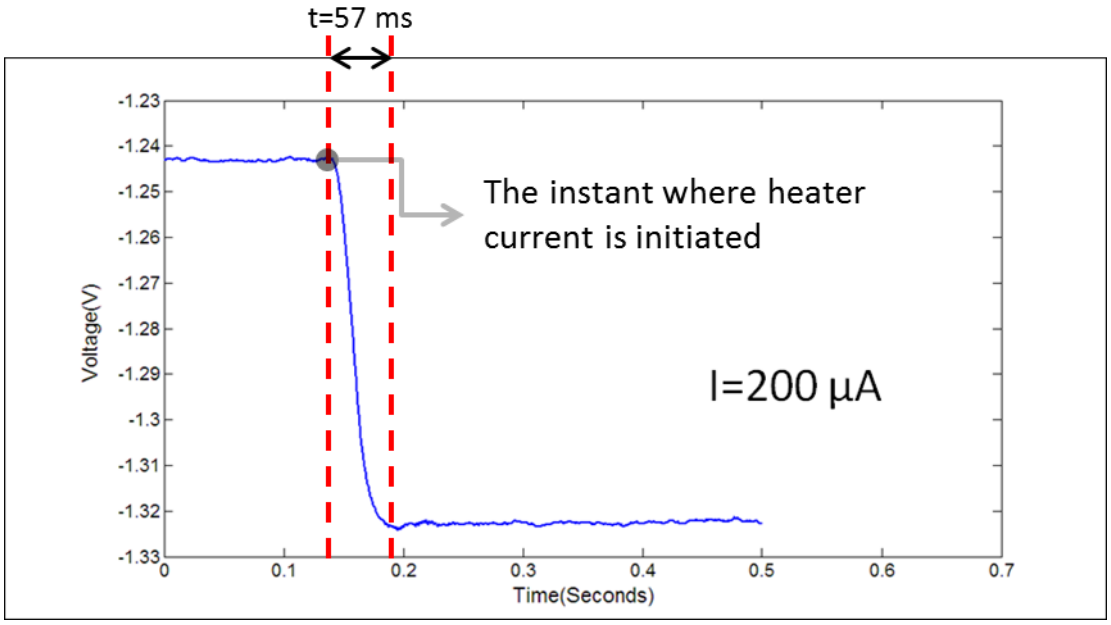

Figure 5.21. Transient voltage response of the thermocouples when heater current 'I' is supplied to the hot junction. An amplifier with a gain of 500 is used.

Being lower at low heating values (around 55 ms) there is no linear behavior of transient response. However, the transient response is observed to be higher at higher heating currents. As the heating power increases, there is a delay in the system response to reach a steady state temperature. The change in the resistance & voltage is not as fast as heating power, so the response time increases. The results for

some heating currents, the corresponding ΔT and voltage responses are presented in Table 5.1.

Table 5.1. The transient voltage response of MEMS TE energy harvester at different heater current values.

Heater Current (mA)	Thermopile Voltage (mV)	Response Time (ms)
0.2	0.1618	57
0.225	0.202	58.6
0.25	0.252	57.2
0.275	0.304	60.1
0.3	0.362	61
0.35	0.492	63.3
0.4	0.644	65.7
0.45	0.816	64.2
0.5	1.01	68.5
0.63	1.604	66.4
0.75	2.274	67.1
0.88	3.138	68.6
1	4.05	70
1.13	5.19	71.5
1.25	6.376	70.6
1.5	9.238	72.7
1.75	12.682	73.1
2	16.69	73.9
2.25	21.35	73.6
2.5	24	74.5

At higher heater current magnitude, the voltage fluctuation becomes higher. When the current is high the thermocouple cannot respond to the frequency of the given current, resulting in relatively high fluctuations in the measured Seebeck voltage.

The time constant of the TE structure cannot match to the current supply, so it takes time for the thermopile to reach a steady state temperature.

5.1.6 Thermal Conductivity Calculation

The equivalent thermal conductivity of the thermocouple materials is calculated by measuring the heat given to the heaters and ΔT along the heat transmission path. The thermocouple material in question is patterned on a cantilever beam. On the tip of the cantilever beam, there is a heater and a monitor resistor. The heat transfer is assumed 1-D from the tip to the base of the cantilever. The thermal conductivity and thickness of the insulating materials (SiO_2, Si_3N_4 and Parylene C) are known. So the thermal conductivity values of the metals were extracted from G_{eq} in Equation (5.6).

$$P_{heater} = I_{heater}^2 R_{heater} = G_{eq} \Delta T \tag{5.6}$$

Where P_{heater}, I_{heater} and R_{heater} are the heater heating power, electrical current given and the electrical resistance of the heater, G_{eq} is the equivalent thermal conductance of the heat transmission path, and ΔT is the temperature difference between hot and cold junctions. The tests were performed on the test structures where there is no or minimal Silicon remaining under. The thermal conductivity of one thermocouple is found to be 110 W/m.K. An average thermal conductivity of 92 W/m.K was expected using the values in literature. The measured thermal conductivity value is acceptable because in MEMS fabrication, the characteristics of the thin films can change with deposition conditions, chemical content and other factors. Also in thin films, grain structure changes with scaling down. This also affects the physical, electrical and chemical properties of the materials.

5.2 Conclusion and Comments on Test Results

The tests were performed to measure the performance characteristics of the MEMS TE structures. The performance characteristics are the voltage and power calculated. Besides, thermal and electrical properties of the thin film materials used were measured by specially designed test structures. The simulation and test results were

correlated. The simulated and measured performance results for some of the devices are shown in Table 5.2.

Table 5.2. Performance of some MEMS TE energy harvesters.

Device #	Area	# of TC's	ΔT_{supp}	V_{OC} (Meas.)	V_{OC} (Sim.)	P_{gen} (Meas.)	P_{gen} (Sim.)
1	2mm x 2mm	48	10 K	17.1 mV	18.2 mV	10.32 nW	10.67 nW
2	2mm x 2mm	48	10 K	13.9 mV	18.2 mV	6.28 nW	10.6 nW
3	2mm x 2mm	48	10 K	10.0 mV	18.2 mV	3.36 nW	10.62 nW
4	2mm x 2mm	48	10 K	9.44 mV	18.2 mV	2.98 nW	10.57 nW

For some devices, the simulation and test results show good agreement. However, there are major differences in performance of the devices. Since the DRIE step of the fabrication is not completed optimally, some Si remains under the suspended structures. The silicon remaining increases thermal conductance and decreases the ΔT generated between the hot and cold junctions of the thermocouples. As a result, the performance of the thermoelectric generator is greatly reduced. Despite the reduced performance caused from high resistivity of the materials and non-ideal fabrication, a power density of 1.1 $\mu W/cm^2$ power density at ΔT=10 K can be obtained from MEMS TE generators using Cr and Ni thermocouples. In case state of the art thermoelectric materials with a high Seebeck coefficient are used, the power generated will increase up to 14 $\mu W/cm^2$ at ΔT=10 K. It is important to note that, we are restricted with electrical resistance in lateral thermoelectric configurations. Vertical generator designs provide remarkably more electrical power than the lateral designs due to much lower electrical resistances. Hence, the possible design and implementation of a vertical TE harvester configuration is given in the next chapter.

CHAPTER 6

SIMULATION AND POSSIBLE FABRICATION OF VERTICAL TE GENERATORS

The feasibility of thermoelectric energy harvesting in mobile systems was shown. Lateral MEMS TE energy harvesters having Cr and Ni thermocouples were fabricated as a proof of concept for thermoelectric energy harvesting. The simulations and measurements of the system were completed to characterize the energy conversion performance. The use of materials having high Seebeck coefficient were analyzed and simulation results were presented. The test results for Cr-Ni thermocouples proved the simulation results are acceptable. Considering the reliability of the simulations, it is estimated that state of the art materials will supply more performance (around ~7-8 times) than Cr-Ni based thermoelectric energy harvesters.

However, lateral MEMS designs have a limitation on the power due to low film thickness and high electrical resistance. When TE energy generation is considered, vertical designs are capable of supplying observably more power than lateral designs. In vertical TE energy harvesters the ΔT created in an identical area is mostly lower than lateral designs, but the electrical resistance can be much lower (1/1000) of thin film designs. This increases the generated power in vertical TE designs.

As a future work, vertical thermoelectric generators utilizing n-Si and p-Si as thermoelectric material are considered. For this purpose, vertical TE generator designs with varying thermoleg thickness were simulated by finite element method. Two different models: a generator using air convection and a generator model using a water cooled system is constructed. A possible fabrication flow for producing

these energy harvesters is also introduced. In Section 6.1, the analogy used in performance calculation of vertical TE energy harvester is shown. In Section 6.2, the verification of the simulation results is accomplished using the test results of commercial TE modules. Section 6.3 includes the performance results of the designed vertical thermoelectric generators. In Section 6.4, a possible fabrication flow for vertical TE harvesters is proposed. Lastly in Section 6.5, the conclusions based on results have been made.

6.1 Analogy used in Thermoelectric Voltage Calculation

In Chapter 2 the phenomena taking place in thermoelectric materials were explained in detail. The main physics dominating the thermoelectric generation was the Seebeck effect, accompanied by Thomson and Peltier effects. Moreover, there is Joule heating in the thermoelectric material caused by electrical current flowing due to the Seebeck effect. All Thomson, Peltier and Joule heating effects contribute to inefficiency of energy conversion in thermoelectric energy harvesting. The simulation methodology counts for these losses, and is constituted adapting the analogy used in [53], [54]. In Comsol Multiphysics, a PDE based model including all of the thermoelectric and Joule heating effects in material matrices was formed. The Heat Transfer Module and Coefficient Form PDE module were coupled together in order to calculate the temperature distribution and electrical characteristics of this coupled physics problem. The equations expressing the physics involved in thermoelectric energy generation are the heat flow equation (6.1) and continuity of electric charge (6.2).

$$\nabla \cdot (-k\nabla T) = Q + q_s T - \rho C_p u \cdot \nabla T \tag{6.1}$$

$$\partial \cdot \left(J + \frac{\partial D}{\partial t} \right) = 0 \tag{6.2}$$

In Equation (6.1), the term on the left is the conduction term, k being the thermal conductivity of the material. Q is the heat source, q_s is the production/absorption coefficient, T is the temperature, ρ is the mass density of the medium, C_p is the heat

capacity and u is the flow field. In Equation (6.2), J is the electric current density vector and D is the electric flux density vector.

The heat transfer equation and the electric charge continuity equation are coupled by Equations (6.3)-(6.5) depicting the Seebeck, Peltier, Thomson and Joule heating effects.

$$q = [\Pi] \cdot J - [\lambda] \cdot \nabla T \tag{6.3}$$

$$J = [\sigma] \cdot (E - [\alpha] \cdot \nabla T) \tag{6.4}$$

$$D = [\varepsilon] \cdot E \tag{6.5}$$

Here, q: heat flux vector, W/m^2

T: absolute temperature, K

$[\Pi]$: Peltier coefficient matrix, V

J: electric current density vector, A/m^2

$[\lambda]$: thermal conductivity matrix,

$[\sigma]$: electrical conductivity matrix, S/m

E: electric field density vector, V/m

$[\alpha]$: Seebeck coefficient matrix, V/K

$[\varepsilon]$: dielectric permittivity matrix, F/m

The equations (6.3)-(6.5) are substituted in (6.1) and (6.2) to give the coupled equations of thermoelectricity (6.6) and (6.7).

$$\rho C \frac{\partial T}{\partial t} + \nabla \cdot ([\Pi] \cdot J) - \nabla \cdot ([\lambda] \cdot \nabla T) = \dot{q} \tag{6.6}$$

$$\nabla \cdot \left([\varepsilon] \cdot \nabla \frac{\partial \varphi}{\partial t} \right) + \nabla \cdot ([\sigma] \cdot [\alpha] \cdot \nabla T) + \nabla \cdot ([\sigma] \cdot \nabla \varphi) = 0 \tag{6.7}$$

Where φ is the potential difference and $E = -\nabla \varphi$. The heat generation $\dot{q}$ term can be expressed by Equation (6.8) [55].

$$\dot{q} = \nabla \cdot ([\lambda] \cdot \nabla T) + E \cdot J + J \cdot \nabla \cdot ([\alpha] \cdot T) \tag{6.8}$$

Here, it is clearly seen from (6.8) that the constitutive thermoelectric equations (6.6) and (6.7) also include the Joule heating term $E \cdot J$.

Substituting these values to material matrices in Coefficient Form PDE Module in Comsol Multiphysics, the properties of the problem domain has been built.

6.2 Verification of the Model with Commercial TE Generator Modules

To verify the finite element model, the calculations are made for commercial thermoelectric modules, MicroTec TE-17-0.6-1.0P and FerroTec 9500/018/012 M P. The characterization of these modules was performed by Reha Denker [38]. The top of the module was heated by a heat source and the bottom was cooled by a water cooled heat sink. The test setup used is shown in Figure 6.1.

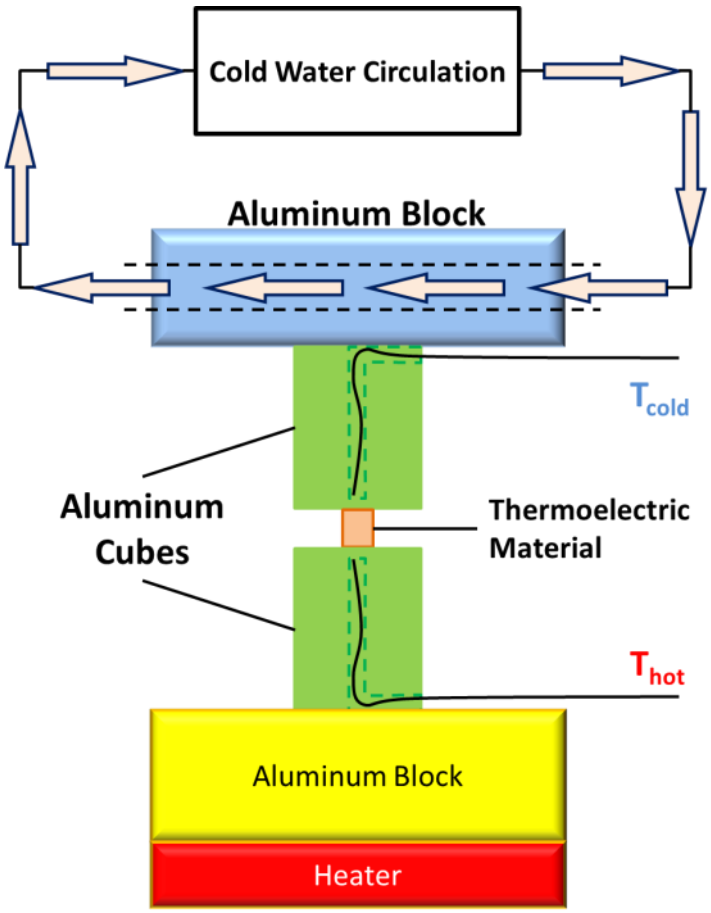

Figure 6.1. The test setup used for testing commercial TE modules.

For the simulations, the exact geometry, material properties of the modules and boundary conditions applied in the tests were used. The comparison between the measurement and simulation results for the Seebeck voltage is shown in Figure 6.2 and Figure 6.3 for two separate commercial modules.

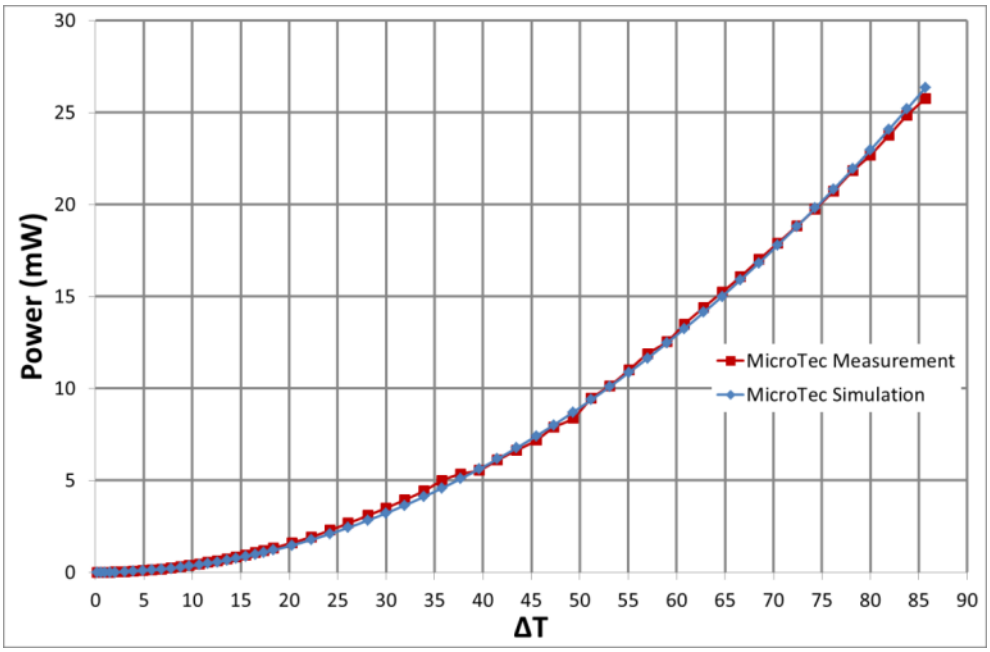

Figure 6.2. The simulation and measurement results of generated power from MicroTec TE-17-0.6-1.0P.

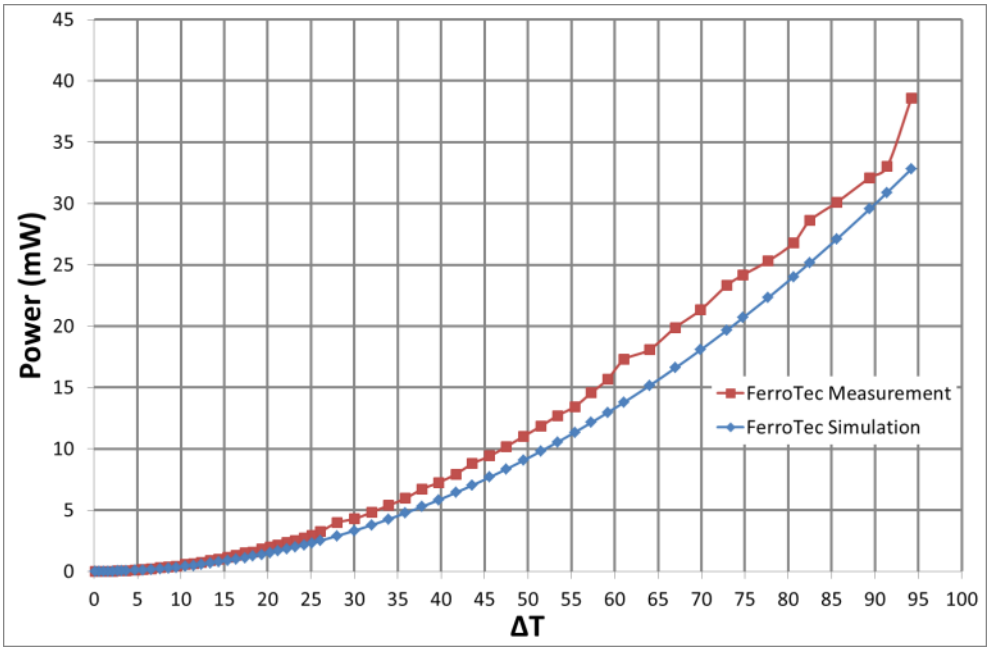

Figure 6.3. The simulation and measurement results of generated power from FerroTec 9500/018/012 M P.

For MicroTec, all the material properties and geometry was supplied by the manufacturer. The simulations are within %1 of the measurement values. In

FerroTec modules, new technology TE materials (Bi_2Te_3 fabricated with a new technology) were used. The exact material properties and geometry details were not given by the company because of confidentiality concerns. So, the material properties (Seebeck coefficient and thermal conductivity of the material) were estimated and the module was measured to obtain the geometric properties. For FerroTec module, the voltage calculations match with the measurements within %20 error range. The error is acceptable because a lot of assumptions have been made in the modeling of the module.

These results show that the analogy and modeling constructed to evaluate the performance of vertical TE energy harvesters is accurate. The same flow of modeling and analysis can be used for any geometry or material selection of vertical TE generator configurations.

6.3 p-Si and n-Si based Vertical TE Generator Modules and Their Performance Characterization

The vertical TE generators comprise of p-Si and n-Si thermolegs having a 50μm x 50μm square cross section. The thickness is varied between 5μm and 100μm. The thermolegs have 50 μm spacing between them and interconnect material is gold. There is a total numver of 4050 thermocouples in $1cm^2$ area. The heat sink and source can be made any material, preferably silicon or ceramic. For fabrication considerations, the heat sink is Si and the heat source is alumina substrate. The thickness of the heat sink and source are 500 μm and 100 μm, respectively. The vertical TE configuration is shown in Figure 6.4. Note that the scaling of the layers is arbitrary.

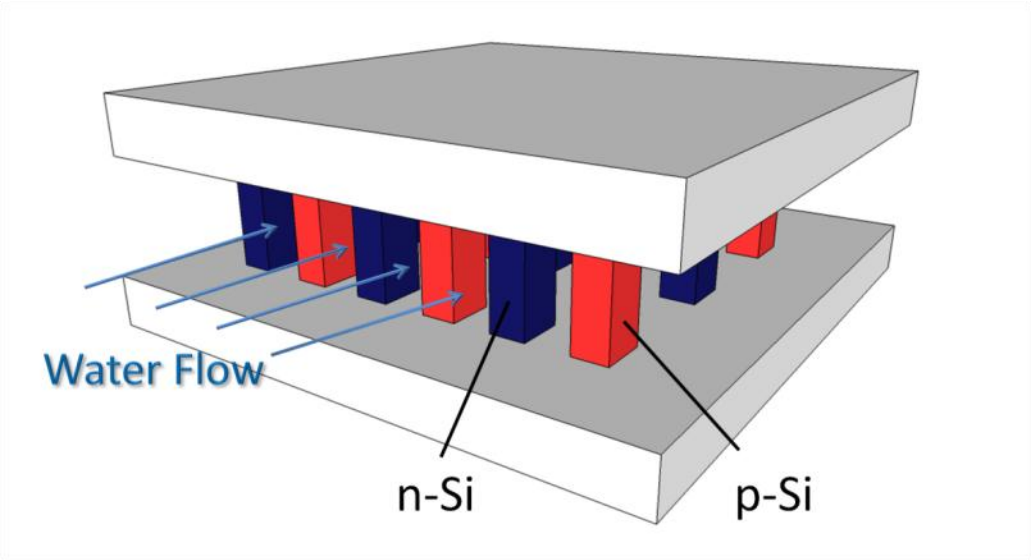

Figure 6.4. Vertical TE generator configuration having p-Si and n-Si as thermoelectric material.

Two designs for vertical thermoelectric generator are made. In the first design, the thermocouples are cooled by natural convection of air. The ΔT generated between the hot and cold junctions is limited with heat source and sink conditions and thermal conductance. When the heat source is heated to 310 K, the temperature distribution for the first design is shown in Figure 6.5. A temperature difference of 3.04 K is obtained in the configuration where only natural convection of air is considered. The voltage generated is 6.57 mV in $1mm^2$ area, which is shown in Figure 6.6.

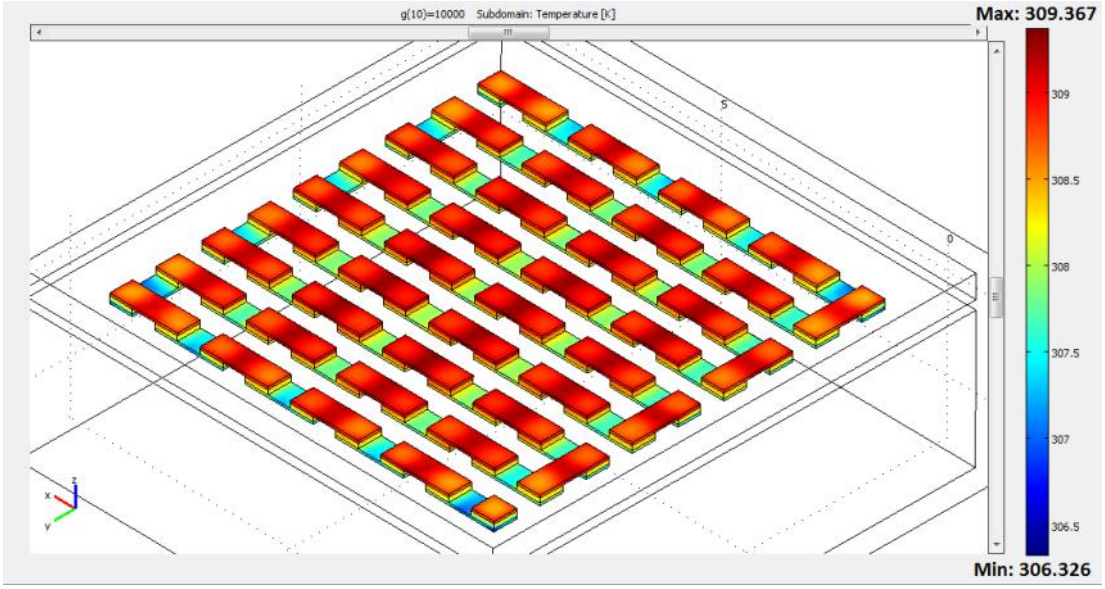

Figure 6.5. The temperature profile of vertical TE generator having a thermocouple height of 10 µm. Heat source is fixed at 310 K. The device seen here is 1mm x 1mm.

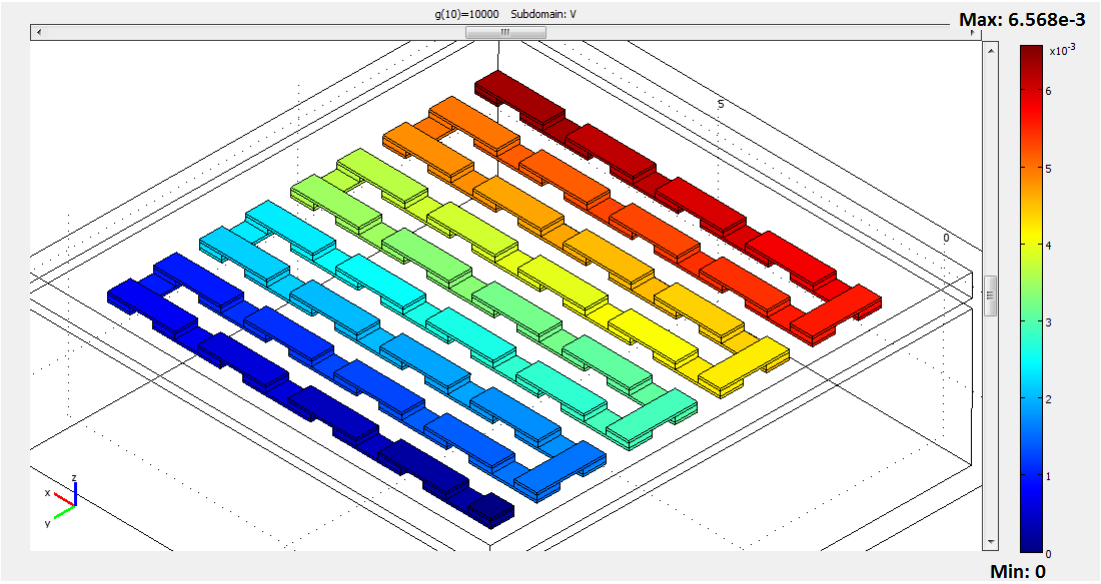

Figure 6.6. The voltage generated from vertical TE generator having a thermocouple height of 10 µm. Heat source is fixed at 310 K. The device seen here is 1mm x 1mm.

The second configuration involves fluid flow between the thermolegs. The thermocouples are assumed to be electrically insulated by deposition of an insulating material to prevent short circuit. The fluid is water, which is can be used in conventional CPU water cooled systems. The water flow rate is taken as 2 m/s. In water cooled systems, 7 l/min is the minimum flow rate attainable with a relatively cheap water cooling system. This means that 2 m/s flow rate is easily attainable by a conventional cooling pump. Navier-Stokes Module is coupled to the existing system to simulate the water flow and cooling rate. The temperature distribution on the vertical TE generator for a water cooled configuration is shown in Figure 6.7. The ΔT generated by water cooling reaches to 5.26 K, which is shown in Figure 6.7. The Seebeck voltage calculated in this case is 14 mV in $1mm^2$ area, as shown in Figure 6.8.

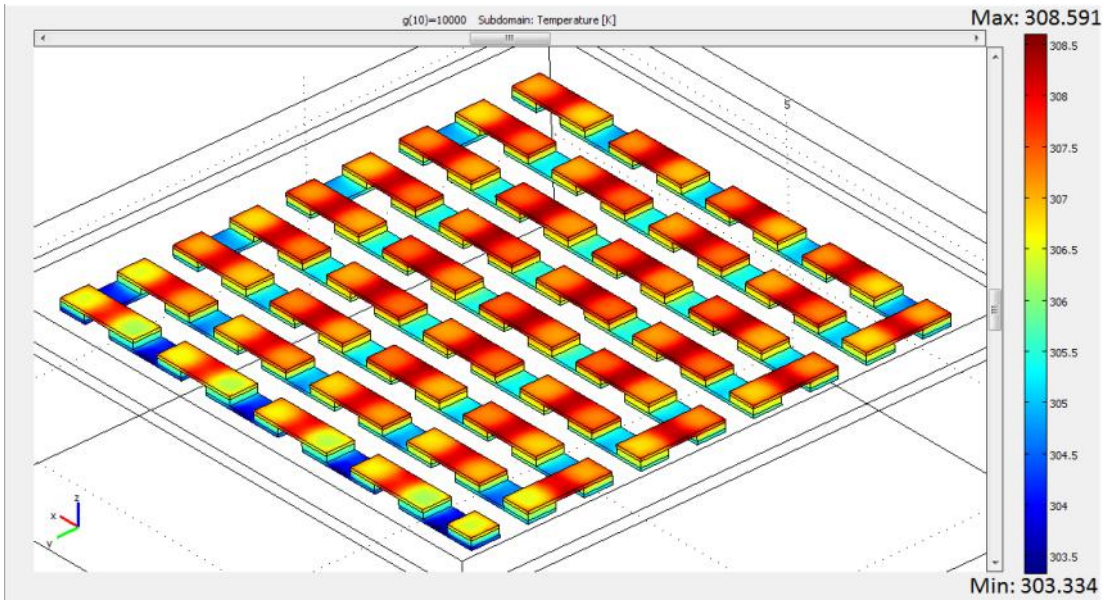

Figure 6.7. The temperature profile of water cooled vertical TE generator having a thermocouple height of 10 μm. Heat source is fixed at 310 K, the inlet water flow velocity is 2 m/s. The device seen here is 1mm x 1mm.

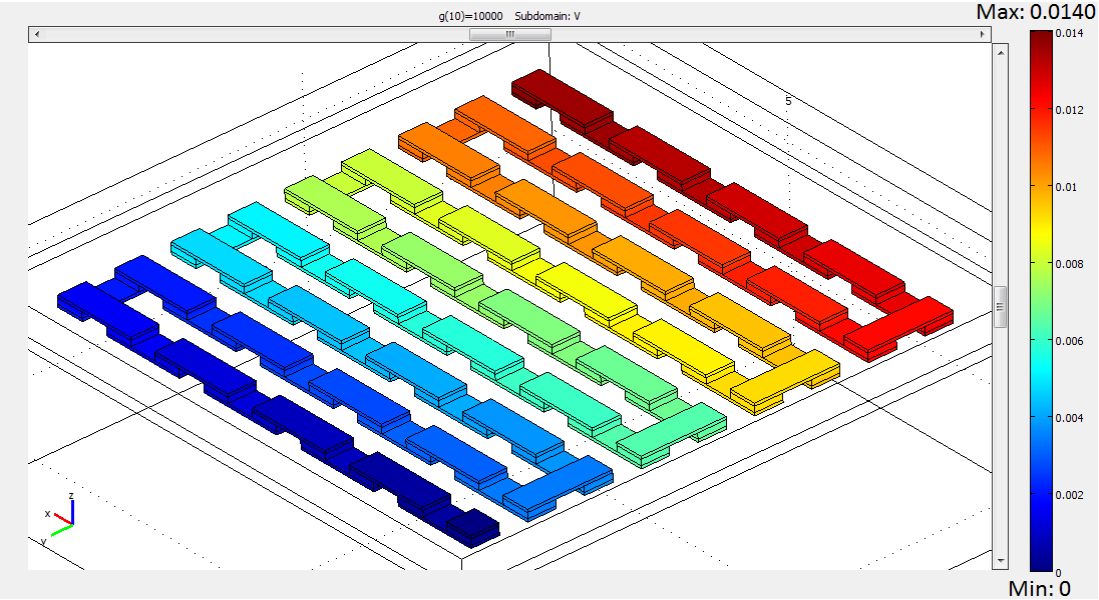

Figure 6.8. The voltage generated from water cooled vertical TE generator having a thermocouple height of 10 µm. Heat source is fixed at 310 K, the inlet water flow velocity is 2 m/s. The device seen here is 1mm x 1mm.

Comparing Figure 6.6 and Figure 6.8, higher voltage is created when water flow is utilized between the thermocouples. A comparison of the electrical power generated for an air cooled and water cooled system is shown in Figure 6.9.

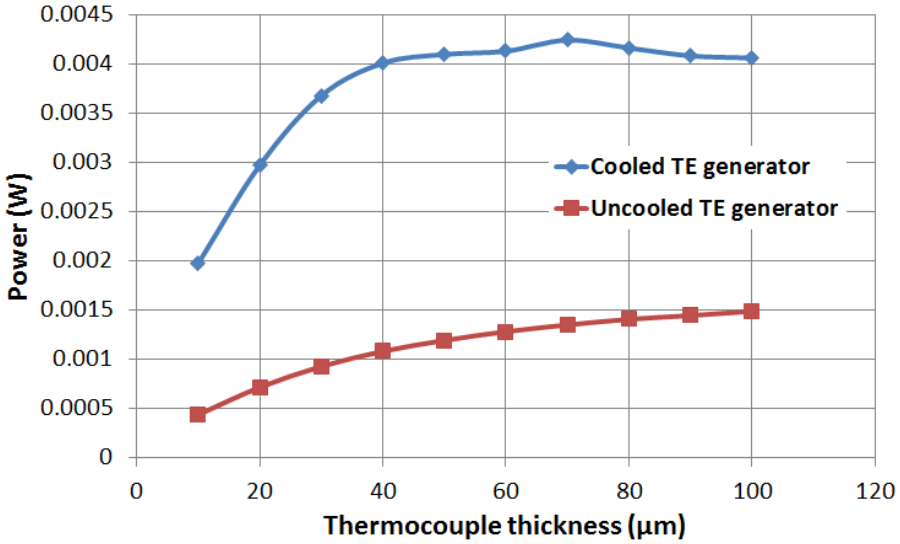

Figure 6.9. The comparison of uncooled and water cooled vertical TE generator configurations having the same geometric properties.

According to Figure 6.9, for a water cooled system, the power generated reaches %350 of an air cooled system. The hot junction being at 310K, electrical power density is 0.46 mW/cm^2 for an air cooled system and 1.9 mW/cm^2 for a water cooled TE generator having 10 μm thermoelectric leg height. With optimized leg height, this power density reaches up to 4.2 mW/cm^2. When the CPU temperature reaches 70°C , which is the average operating core temperatures at high processor load, the power density reaches up to 14.9 mW/cm^2 for a water cooled vertical TE generator. The pumping power is also another consideration here in terms of power management, but its analysis is out of the scope of this thesis. Note that, this system can be implemented in computers where water cooling is available at hand, without requiring extra load on the power supplied.

The comparison of the proposed vertical TE generator design with the other vertical TE designs in literature is made in Table 6.1. Neglecting the electrical contact resistance between the thermocouples and interconnects, the proposed water cooled design provides the highest power density through its counterparts.

Table 6.1. Comparison of the water cooled vertical TE generator with the best performance TE generators reported in literature.

	Dimensions	TC material		# of TC's per cm^2	ΔT (K)	Resistance (Ohm)	Power	Power Density (mW/cm^2)
Kishi et al. [3]	5x5x1.3 mm^3	p-type	BiTeSb	2600	1	2500	22.5 μW	0.09
		n-type	Bi_2Te_3					
Stordeur & Stark [4]	9x7.5x2.8 mm^3	p-type	$(Bi_{0.25}Sb_{0.75})_2Te_3$	3333	80	1.33 x 10^6	363 μW	0.538
		n-type	$Bi_2(Se_{0.1}Te_{0.9})_3$					
Böttner et al. [5]	0.65x0.55x0.43 mm^3	p-type	$(Bi,Sb)_2Te_3$	1070	9	450	3.5 μW	0.979
		n-type	Bi_2Te_3					
Glosh et al. [6]	11x1.5x0.5 mm^3	p-type	Al	6060	10	5.45 x 10^6	1.5 μW	0.0091
		n-type	n-Si					
Strasser et al. [7]	3.2x2.2x0.5 mm^3	p-type	p-polySi	225400	5	29 x 10^6	1 μW	0.014
		n-type	n-polySi					
Cooled vertical TE generator (Simulated)	10x10x0.65 mm^3	p-type	p-Si	4000	10	1755	**4.2 mW**	**4.2**
		n-type	n-Si					

6.4 Possible Fabrication of the Vertical TE harvesters

The fabrication of proposed vertical thermoelectric energy harvesters can be done by doping or using SOI wafers.

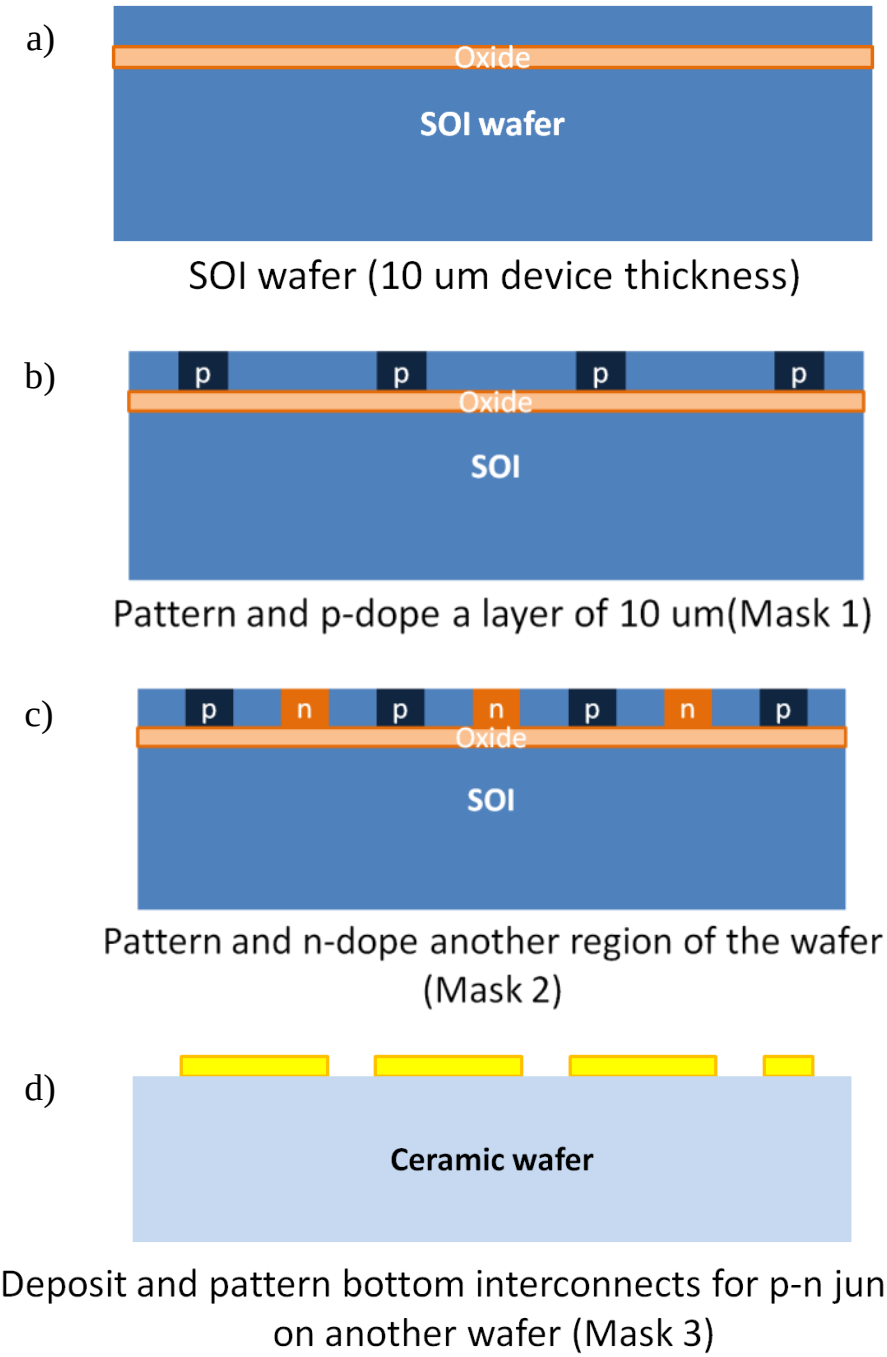

Figure 6.10. Possible fabrication of vertical TE generator.

e)

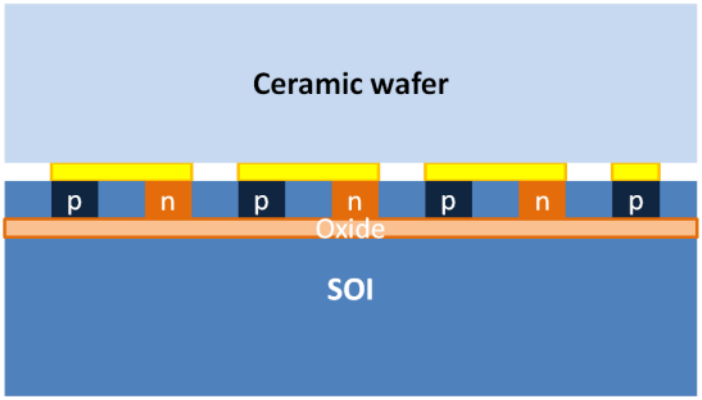

Alignment and soldering the metal layer to form the junctions and bond two wafers together

f)

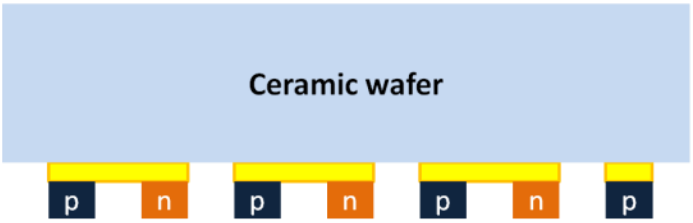

Thinning and etching the Si in DRIE and etching oxide in BHF

g)

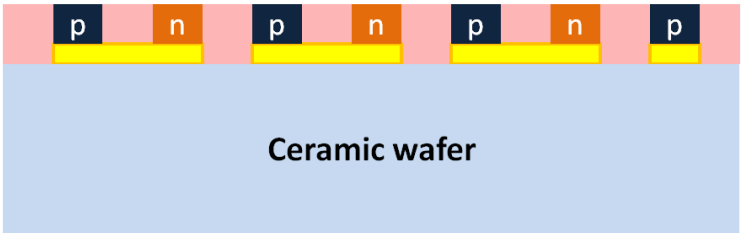

Cover with sacrificial photoresist layer

h)

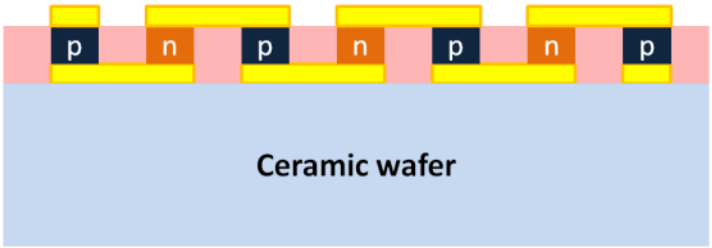

Deposit and pattern top interconnect layer (Mask 4)

Figure 6.10 continued.

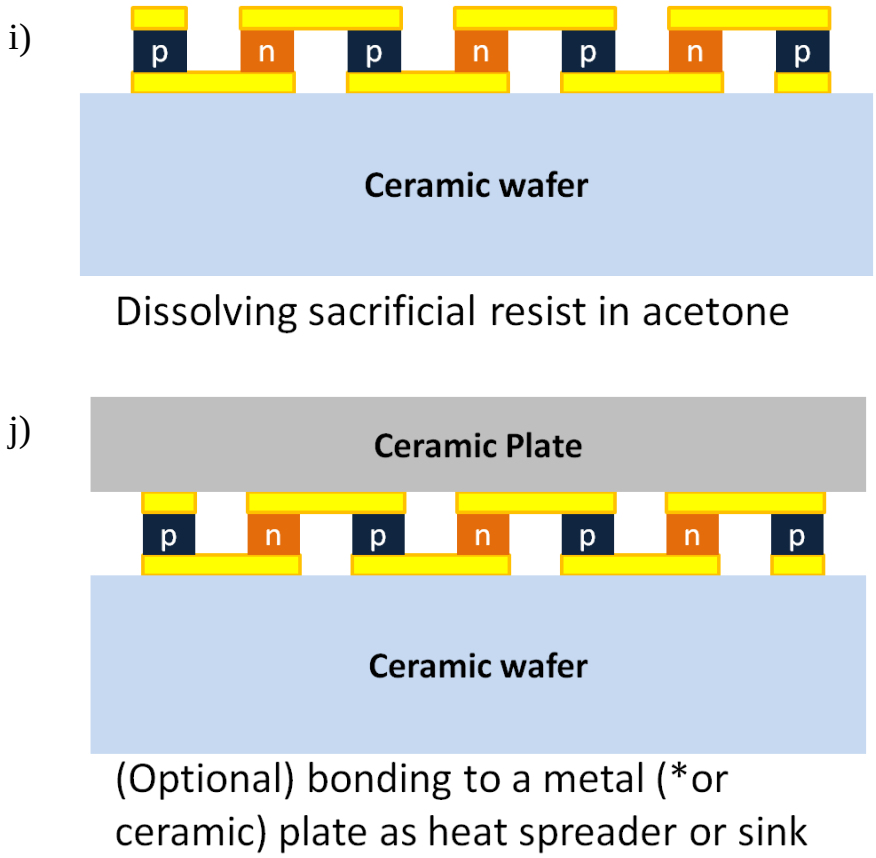

Figure 6.10 continued.

The doping depth in the above figure is limited with the doping technology available at hand (~11 μm). For increasing the device layer thickness to increase ΔT, SOI wafers having doped device layers can be used for the fabrication. A possible fabrication of vertical TE generator using SOI is given in Appendix C.

For water cooling, Parylene C or other insulating material can be deposited and patterned over the thermolegs to prevent short circuit during the water flow.

6.5 Conclusion and Comments on Results

The feasibility of the thick film energy harvesters for implementation in mobile systems was discussed. In thermoelectric energy harvesting, decreasing the electrical resistance and using state of the art thermoelectric materials that have high Seebeck coefficient are important to harness high amount of electrical power from heat. For this purpose, two vertical TE energy harvester designs were proposed. One is a

conventional design with natural air convection and the second is a design with fluid flow between the thermopile arrays. The finite element simulations for performance have been made in Comsol Multiphysics with a modeling technique based on the mathematics of thermoelectricity. The validation of the modeling was done by comparison of the simulation and measurement results using commercial thermoelectric modules. It is shown that power levels in the range of few milliwatts per cm^2 are attainable with low ΔT (10 K), and application of vertical TE generator designs to notebook or desktop computers is feasible.

CHAPTER 7

CONCLUSIONS AND FUTURE RESEARCH

In this thesis, a new MEMS thermoelectric energy harvester utilizing Cr and Ni thermocouples is presented. The proposed design has the advantage of being easily fabricated, low cost, and compatible with MEMS technology. The energy density obtained from MEMS thermoelectric energy harvester is comparable with its counterparts in literature. Moreover, the design can be adapted to vibrational energy scavengers fabricated in METU MEMS Center to realize multi-mode energy harvesting.

The tasks completed in this thesis can be summarized as follows:

- The design and optimization of performance of MEMS TE energy harvesters were done in order to obtain the best power attainable. The performance calculations were done analytically and by finite element method.
- Test structures were designed to characterize the MEMS TE energy harvesters thermally and electrically.
- The masks were drawn taking into account optimized configurations and test structures.
- The fabrication of MEMS TE energy harvesters was completed using standard MEMS fabrication techniques.
- The testing of lateral MEMS TE harvester structures was done in order to complete the performance characterization. The simulation results and test results were correlated. The MEMS TE energy harvesters proposed in this study can generate 1.1 $\mu W/cm^2$ power and 1.71 V/cm^2 open circuit voltage

for a temperature difference of 10 K applied to the hot junction. On a notebook CPU, 6.9μW/cm^2 and 4.28 V/cm^2 can be obtained with a temperature difference of 25 K supplied between the hot and cold regions.

- Finally, vertical thermoelectric generator designs using p-Si and n-Si as thermocouples were proposed for increased generated electrical power density. The detailed simulation was conducted using finite element method, and a possible fabrication flow is proposed. The simulation methodology was verified by comparing the simulation and test results of commercial thermoelectric modules. The power density of vertical TE energy harvesters was calculated as 4.2mW/cm^2 for a heat source at 310 K. This estimated power density is the highest among the other thermoelectric generator configurations reported in literature.

Although proof-of-concept Cr-Ni based MEMS thermoelectric generator prototypes are proved to function as they were designed, there are still many developments that should be made for energy harvesting from heat. Some of the future work includes:

- Implementation of state-of-the-art thermoelectric materials to MEMS thermoelectric harvesters proposed should be considered. The use of high Seebeck coefficient materials will yield at least ~7-8 times or more power than the Cr-Ni thermopiles.
- Surface modification techniques should be studied in order to use Parylene C with thin film thermoelectric materials to develop a more reliable process flow. This will provide a robust and repeatable fabrication process to integrate state-of-the-art thermoelectric materials to Parylene C fabrication.
- In the fabricated MEMS thermoelectric energy harvesters, DRIE process was not fully optimized. The silicon remaining under the diaphragms increases the thermal conductivity and inhibits the maximum power extraction from the devices. Thus, DRIE process should be optimized to get fully suspended structures. By this way, performance characterization will be done more accurately.
- Most important of all, vertical thermoelectric harvester designs should be considered to obtain enough power to run electronic components. In the

simulations, it was shown that power density in the range of 4.2 mW/cm^2 (three orders of magnitude higher power than that of the lateral MEMS designs) and more can be obtained with vertical thermoelectric generator designs when the height of the legs is optimized. This shows a great potential for integration of vertical TE energy harvesters to mobile electronic systems. The vertical TE designs should be investigated in detail and a more detailed fabrication method should be developed.

REFERENCES

[1] J. A. Paradiso and T. Starner, "Energy scavenging for mobile and wireless electronics," *Pervasive Computing, IEEE*, vol. 4, no. 1, pp. 18-27, 2005.

[2] F. Yildiz, "Potential Ambient Energy-Harvesting Sources and Techniques," *Journal of Technology Studies*, vol. 35, no. 1, p. 9, 2009.

[3] S. W. Angrist, *Direct Energy Conversion*, 4th ed. Allyn & Bacon, 1982.

[4] H. Glosch, M. Ashauer, U. Pfeiffer, and W. Lang, "A thermoelectric converter for energy supply," *Sensors and Actuators A: Physical*, vol. 74, no. 1-3, pp. 246-250, Apr. 1999.

[5] M. Strasser, R. Aigner, C. Lauterbach, T. F. Sturm, M. Franosch, and G. Wachutka, "Micromachined CMOS thermoelectric generators as on-chip power supply," *Sensors and Actuators A: Physical*, vol. 114, no. 2-3, pp. 362–370, 2004.

[6] W. Wang, F. Jia, Q. Huang, and J. Zhang, "A new type of low power thermoelectric micro-generator fabricated by nanowire array thermoelectric material," *Microelectronic Engineering*, vol. 77, no. 3-4, pp. 223-229, Apr. 2005.

[7] J. Weber, K. Potje-Kamloth, F. Haase, P. Detemple, F. Völklein, and T. Doll, "Coin-size coiled-up polymer foil thermoelectric power generator for wearable electronics," *Sensors and Actuators A: Physical*, vol. 132, no. 1, pp. 325-330, Nov. 2006.

[8] G. J. Snyder, J. R. Lim, C.-K. Huang, and J.-P. Fleurial, "Thermoelectric microdevice fabricated by a MEMS-like electrochemical process," *Nat Mater*, vol. 2, no. 8, pp. 528-531, print 2003.

[9] J.-F. Li, S. Tanaka, T. Umeki, S. Sugimoto, M. Esashi, and R. Watanabe, "Microfabrication of thermoelectric materials by silicon molding process," *Sensors and Actuators A: Physical*, vol. 108, no. 1-3, pp. 97-102, Nov. 2003.

[10] M. Kishi et al., "Micro thermoelectric modules and their application to wristwatches as an energy source," in *Thermoelectrics, 1999. Eighteenth International Conference on*, 1999, pp. 301-307.

[11] M. Kishi et al., "Fabrication of a miniature thermoelectric module with elements composed of sintered Bi-Te compounds," in *Thermoelectrics, 1997. Proceedings ICT '97. XVI International Conference on*, 1997, pp. 653-656.

[12] K. Miyazaki, T. Lida, and H. Tsukamoto, "Micro-fabrication of Bi2Te3 by using micro-jet," in *Thermoelectrics, 2003 Twenty-Second International Conference on - ICT*, 2003, pp. 641-643.

[13] G. Savelli, M. Plissonnier, V. Remondiere, C. Salvi, and J. M. Fournier, "Development of 3D thermoelectric generators using Bi and Sb elements," in *Thermoelectrics, 2007. ICT 2007. 26th International Conference on*, 2007, pp. 310-313.

[14] G. Savelli, M. Plissonnier, J. Bablet, C. Salvi, and J. M. Fournier, "Realization and optimization of thermoelectric devices using bismuth and antimony materials," in *25th International Conference on Thermoelectrics, 2006. ICT '06*, 2006, pp. 394-398.

[15] S. V. Garimella et al., "Thermal Challenges in Next-Generation Electronic Systems," *IEEE Transactions on Components and Packaging Technologies*, vol. 31, no. 4, pp. 801-815, Dec. 2008.

[16] K. Yazawa and A. Bar-Cohen, "Energy efficient cooling of notebook computers," in *The Eighth Intersociety Conference on Thermal and Thermomechanical Phenomena in Electronic Systems, 2002. ITHERM 2002*, 2002, pp. 785- 791.

[17] M. Ma, S. H. Gunther, B. Greiner, N. Wolff, C. Deutschle, and T. Arabi, "Enhanced thermal management for future processors," in *2003 Symposium on VLSI Circuits, 2003. Digest of Technical Papers*, 2003, pp. 201- 204.

[18] A. Bar-Cohen, "Thermal management of microelectronics in the 21st century," in *Electronic Packaging Technology Conference, 1997. Proceedings of the 1997 1st*, 1997, pp. 29-33.

[19] M. Iyengar and A. Bar-Cohen, "Least-energy optimization of forced convection plate-fin heat sinks," in *The Eighth Intersociety Conference on Thermal and Thermomechanical Phenomena in Electronic Systems, 2002. ITHERM 2002*, 2002, pp. 792- 799.

[20] G. L. Solbrekken, K. Yazawa, and A. Bar-Cohen, "Chip level refrigeration of portable electronic equipment using thermoelectric devices," in *Proceedings of InterPack*, 2003, pp. 6–11.

[21] P. E. Phelan, V. Chiriac, and T.-Y. . Lee, "Current and future miniature refrigeration cooling technologies forhigh power microelectronics," in *Semiconductor Thermal Measurement and Management, 2001. Seventeenth Annual IEEE Symposium*, 2001, pp. 158-167.

[22] G. L. Solbrekken, K. Yazawa, and A. Bar-Cohen, "Thermal management of portable electronic equipment using thermoelectric energy conversion," in *The Ninth Intersociety Conference on Thermal and Thermomechanical Phenomena in Electronic Systems, 2004. ITHERM '04*, 2004, pp. 276- 283 Vol.1.

[23] "Method and apparatus for recovering power from semiconductor circuit using thermoelectric device - US Patent 5419780 Abstract." [Online]. Available: http://www.patentstorm.us/patents/5419780.html. [Accessed: 24-Aug-2011].

[24] A. Oliver, *A bulk-micromachined uncooled infrared imager for use in semiconductor process control applications.* 1997.

[25] S. Kasap, *Principles of Electronic Materials and Devices*, 3rd ed. McGraw-Hill Science/Engineering/Math, 2005.

[26] A. Miele, R. Fletcher, E. Zaremba, Y. Feng, C. T. Foxon, and J. J. Harris, "Phonon-drag thermopower and weak localization," *Physical Review B*, vol. 58, no. 19, p. 13181, Nov. 1998.

[27] A. W. Van Herwaarden, "The seebeck effect in silicon ICs," *Sensors and Actuators*, vol. 6, no. 4, pp. 245-254, Dec. 1984.

[28] A. W. van Herwaarden, D. C. van Duyn, B. W. van Oudheusden, and P. M. Sarro, "Integrated thermopile sensors," *Sensors and Actuators A: Physical*, vol. 22, no. 1-3, pp. 621-630, Jun. 1989.

[29] S. Priya and D. J. Inman, Eds., *Energy Harvesting Technologies*. Boston, MA: Springer US, 2009.

[30] "BestZTs.jpg (JPEG grafiği, 1355x1094 piksel)." [Online]. Available: http://chemgroups.northwestern.edu/kanatzidis/resources/BestZTs.jpg. [Accessed: 24-Aug-2011].

[31] Volklein, "Review of the thermoelectric efficiency of bulk and thin-film materials," *Sensors and Materials*, vol. 8, no. 6, pp. 389-408, 1996.

[32] A. Shakouri and C. LaBounty, "Material optimization for heterostructure integrated thermioniccoolers," in *Eighteenth International Conference on Thermoelectrics, 1999*, 1999, pp. 35-39.

[33] A. Shakouri and Suquan Li, "Thermoelectric power factor for electrically conductive polymers," in *Eighteenth International Conference on Thermoelectrics, 1999*, 1999, pp. 402-406.

[34] D. M. Rowe, *Thermoelectrics Handbook: Macro to Nano*, 1st ed. CRC Press, 2005.

[35] W. J. Minkowycz, E. M. Sparrow, and J. Y. Murthy, *Handbook of Numerical Heat Transfer*, 2nd ed. Wiley, 2006.

[36] K. Banerjee, A. Mehrotra, A. Sangiovanni-Vincentelli, and Chenming Hu, "On thermal effects in deep sub-micron VLSI interconnects," in *Design Automation Conference, 1999. Proceedings. 36th*, 1999, pp. 885-891.

[37] T. Akin, Z. Olgun, O. Akar, and H. Kulah, "An integrated thermopile structure with high responsivity using any standard CMOS process," *Sensors and Actuators A: Physical*, vol. 66, no. 1-3, pp. 218-224, Apr. 1998.

[38] R. Denker, A. Muhtaroğlu, and H. Külah, "Quantification of thermoelectric energy scavenging opportunity for microelectronic system integration," *PowerMEMS Conference 2011*, to be published.

[39] D. M. Rowe, D. V. Morgan, and J. H. Kiely, "Miniature low-power/high-voltage thermoelectric generator," *Electronics Letters*, vol. 25, no. 2, pp. 166-168, Jan. 1989.

[40] I. Stark and M. Stordeur, "New micro thermoelectric devices based on bismuth telluride-type thin solid films," in *Thermoelectrics, 1999. Eighteenth International Conference on*, 1999, pp. 465-472.

[41] K. Itoigawa, H. Ueno, M. Shiozaki, T. Toriyama, and S. Sugiyama, "Fabrication of flexible thermopile generator," *Journal of Micromechanics and Microengineering*, vol. 15, no. 9, p. S233-S238, Sep. 2005.

[42] H. Bottner et al., "New thermoelectric components using microsystem technologies," *Journal of Microelectromechanical Systems*, vol. 13, no. 3, pp. 414- 420, Jun. 2004.

[43] O. Paul, M. von Arx, and H. Baltes, "Process-dependent Thermophysical Properties Of CMOS IC Thin Films," in *The 8th International Conference on Solid-State Sensors and Actuators, 1995 and Eurosensors IX.. Transducers '95*, 1995, vol. 1, pp. 178-181.

[44] F. E. Rasmussen, J. Frech, M. Heschel, and O. Hansen, "Fabrication of high aspect ratio through-wafer vias in CMOS wafers for 3-D packaging applications," in *TRANSDUCERS, Solid-State Sensors, Actuators and Microsystems, 12th International Conference on, 2003*, 2003, vol. 2, pp. 1659-1662 vol.2.

[45] N. P.-S. Matthieu, M. Liger, and Y.-chong Tai, "Flexible Parylene-Valved Skin For Adaptive Flow Control."

[46] V. K. Khanna, "Adhesion–delamination phenomena at the surfaces and interfaces in microelectronics and MEMS structures and packaged devices," *Journal of Physics D: Applied Physics*, vol. 44, p. 034004, 2011.

[47] J. A. Thornton, "The microstructure of sputter-deposited coatings," *Journal of Vacuum Science & Technology A: Vacuum, Surfaces, and Films*, vol. 4, no. 6, p. 3059, Nov. 1986.

[48] P. Lambkin, B. Lane, I. O'Heifearnan, J. Gillham, and R. Eatton, "Characterisation of CMOS compatible uncooled microbolometers," in *2000 IEEE/LEOS International Conference on Optical MEMS*, 2000, pp. 99-100.

[49] A. Tanaka et al., "Infrared focal plane array incorporating silicon IC processcompatible bolometer," *IEEE Transactions on Electron Devices*, vol. 43, no. 11, pp. 1844-1850, Nov. 1996.

[50] S. Beeby and N. White, *Energy Harvesting for Autonomous Systems*. Artech House, 2010.

[51] Yu Zhou, S. Paul, and S. Bhunia, "Harvesting Wasted Heat in a Microprocessor Using Thermoelectric Generators: Modeling, Analysis and Measurement," in *Design, Automation and Test in Europe, 2008. DATE '08*, 2008, pp. 98-103.

[52] P. (Peter M. Mayer, "High-density thermoelectric power generation and nanoscale thermal metrology." [Online]. Available: http://dspace.mit.edu/handle/1721.1/40503. [Accessed: 17-Aug-2011].

[53] E. E. Antonova and D. C. Looman, "Finite elements for thermoelectric device analysis in ANSYS," in *24th International Conference on Thermoelectrics, 2005. ICT 2005*, 2005, pp. 215- 218.

[54] M. Jaegle, M. Bartel, A. Jacquot, H. Böttner, and D. Ebling, "Multiphysics Simulation of Thermoelectric Systems for Comparison with Experimental

Device Performance," *Journal of Electronic Materials*, vol. 38, no. 7, pp. 1456-1461, 2009.

[55] L. D. Landau, L. P. Pitaevskii, and E. M. Lifshitz, *Electrodynamics of Continuous Media, Second Edition: Volume 8*, 2nd ed. Butterworth-Heinemann, 1984.

APPENDIX A

MATLAB FILE FOR THERMOELECTRIC DESIGN

```
clear all

l=logspace(-3.92,-3.4,200); % thermocouple length span

tkp=logspace(-8,-5,200); % Cr thickness

tpary=5.5e-6; % Parylene C thickness

    kp=93.7; % thermal conductivity of Cr

    kn=90.9; % thermal conductivity of Ni

    kpary=0.082; % thermal conductivity of Parylene C

    wp=10e-6; % Cr width

    wn=10e-6; % Ni width

    wheat=10e-6; % heater width

    Th=310; % hot side temperature

    rop=125e-9; % Cr resistivity

    ron=69.3e-9; % Ni resistivity

    alphap=21.8e-6; % Cr Seebeck coefficient

    alphan=-19.5e-6; % Ni Seebeck coefficient

    alpha=(alphap-alphan)./2; % average Seebeck coefficient

hhot=10; %convection coefficient from the surface
```

```
qhot=10e-5; %heat flowing through the cross section of the diaphragm
arm
for i=1:size(l,2)

    for j=1:size(tkp,2)

    tkn(j)=tkp(j)/1.32;

    wdia(i)=2*((0.4e-3)-(l(i)-120e-6));

    n(i)=((round(wdia(i)./(20e-6))).*4);

    nheat(i)=((round((wdia(i)-100e-6)./(40e-6))).*4);

    lheat(i)=nheat(i).*(320e-6);

    tpeff(j,i)=(0.5.*n(i).*wp.*tkp(j))./(4.*wdia(i));

    tneff(j,i)=(0.5.*n(i).*wn.*tkn(j))./(4.*wdia(i));

    tparyeff=tpary;

    ttotal(j,i)=tpeff(j,i)+tneff(j,i)+tparyeff;

    keff(j,i)=(( (kp.*tpeff(j)) + (kn.*tneff(j)) + (kpary.*tparyeff)
) ./ ttotal(j));

    beta(j,i)=sqrt(hhot./(keff(j,i).*ttotal(j,i)));

    thermalR(j,i)=
0.25*sinh(beta(j,i).*l(i))./(keff(j,i).*ttotal(j,i).*wdia(i).*beta(j
,i).*cosh(beta(j,i).*l(i)));

    thermalK(j,i)=1./(thermalR(j,i));

    deltaTth(j,i) = qhot*thermalR(j,i);


heaterthermalR(j,i)=((1./nheat(i)).*(lheat(i)./(kn.*wheat.*tkn(j))))
;


heaterelectricalR(j,i)=((nheat(i)).*((ron.*lheat(i))./(wheat.*tkn(j)
)));

    Relfit(j,i)=(n(i)./2).*rop.*(l(i)./(wp.*tkp(j))) +
(n(i)./2).*ron.*(l(i)./(wn.*tkn(j)));

    Vfit(j,i)=n(i).*alpha.*deltaTth(j,i);

    Ite(j,i)=Vfit(j,i) ./(2.*Relfit(j,i));
```

```
    pheat(j,i)= (alpha.*Th.*Ite(j,i) ) -
(0.5.*((Ite(j,i)).^2).*Relfit(j,i)) +
((thermalK(j,i)).*deltaTth(j,i));

    powerfit(j,i)= (Vfit(j,i).^2)./(4.*Relfit(j,i));

    eff(j,i)=100.*((powerfit(j,i)/pheat(j,i)));

    Iheater(j,i)=sqrt(pheat(j,i)./heaterelectricalR(j,i));

    Vheater(j,i)=Iheater(j,i).*heaterelectricalR(j,i);

    end
end

figure(1)
meshc(log10(l),log10(tkp),(deltaTth))
xlabel('Log of l')
ylabel('Log of thickness')
zlabel('Magnitude of deltaT') %Plots the temperature difference
between the ends as a function of TC length and thickness

figure(2)
meshc(log10(l),log10(tkp),(powerfit))
xlabel('Log of l')
ylabel('Log of thickness')
zlabel('Magnitude of Electrical Power(W)') %Plots the electrical
power as a function of TC length and thickness

figure(3)
meshc(log10(l),log10(tkp),(Vfit))
xlabel('Log of l')
ylabel('Log of thickness')
zlabel('Magnitude of Voltage(V)') %Plots the Seebeck voltage as a
function of TC length and thickness

figure(4)
meshc(log10(l),log10(tkp),(thermalR))
xlabel('Log of l')
ylabel('Log of thickness')
zlabel('Magnitude of Thermal Resistance [K/W]') %Plots the thermal
resistance as a function of TC length and thickness

figure(5)
meshc(n,log10(tkp),(powerfit))
xlabel('n')
ylabel('Log of l')
zlabel('Magnitude of Electrical Power (W)')  %Plots the electrical
power as a function of TC number and thickness

figure(6)
meshc(n,log10(tkp),(deltaTth))
xlabel('TC number')
ylabel('Log of tkp')
```

```
zlabel('Magnitude of deltaT') %Plots the temperature difference
between the ends as a function of TC number and thickness

figure(7)
meshc(log10(l),log10(tkp),(pheat))
xlabel('log of l')
ylabel('Log of tkp')
zlabel('Magnitude of heater power (W)') %Plots the heater power as a
function of TC length and thickness

figure(8)
meshc(log10(l),log10(tkp),(eff))
xlabel('log of TC length')
ylabel('Log of tkp')
zlabel('TE conversion efficiency') %Plots the conversion efficiency
as a function of TC length and thickness


figure(9)
meshc(log10(l),log10(tkp),(Iheater))
xlabel('log of TC length')
ylabel('Log of tkp')
zlabel('Heater current (A)') %Plots the heater current required as a
function of TC length and thickness

figure(10)
meshc(log10(lheat),log10(tkn),( heaterelectricalR))
xlabel('log of heater length')
ylabel('Log of heater thickness')
zlabel('Heater electrical resistance (ohm)') %Plots the heater
electrical resistance as a function of heater length and thickness

figure(11)
meshc(nheat,log10(tkn),(heaterelectricalR))
xlabel('number of heaters')
ylabel('Log of heater thickness')
zlabel('Heater electrical resistance (ohm)') %Plots the heater
electrical resistance as  a function of number of turns in
serpentine and thickness

figure(12)
meshc(nheat,log10(tkn),(Vheater))
xlabel('number of heaters')
ylabel('Log of heater thickness')
zlabel('Heater voltage (V)') %Plots the required heater voltage as a
function of number of turns in serpentine and thickness
```

APPENDIX B

MASK SETS USED IN FABRICATION

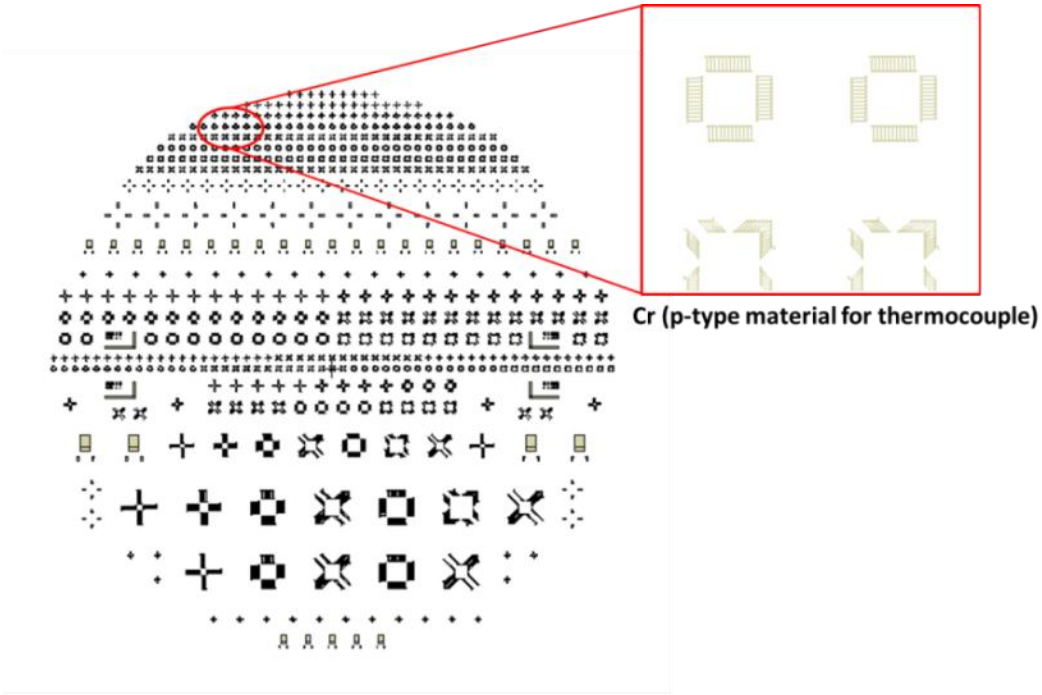

Figure B.1. 1st mask set for patterning and etching Cr layer is shown. Cr layer will form the p-type thermoelectric layer of the thermopile.

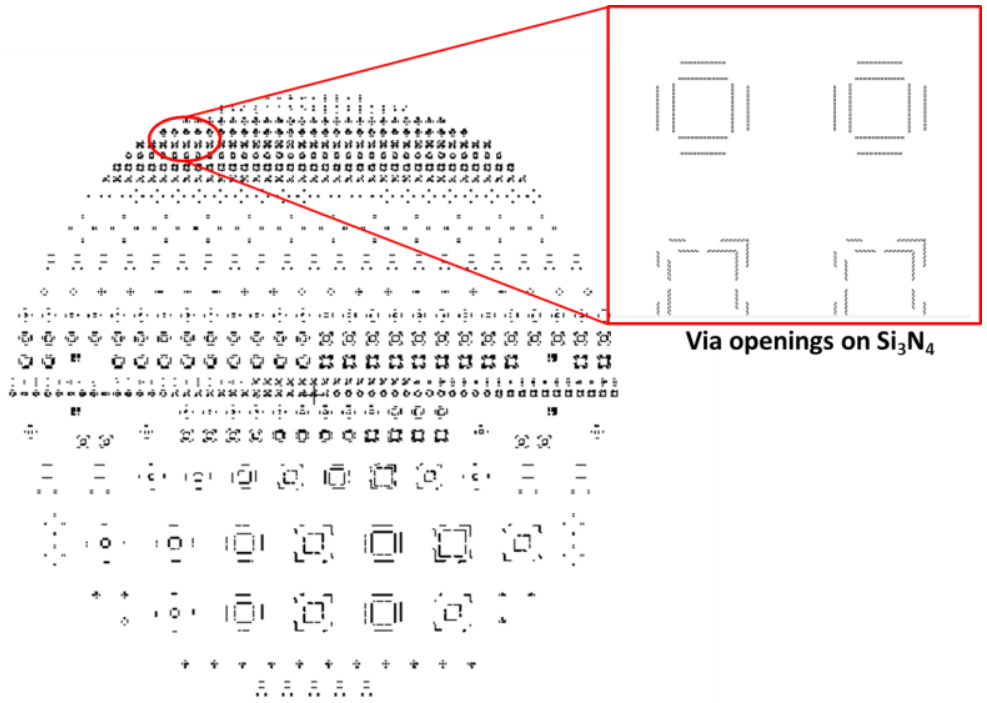

Figure B.2. 2nd mask set to form vias is shown. After deposition of intermediate insulation layer (Si_3N_4), it is patterned with 2nd mask to form vias that will enable junction of Cr and Ni to form thermocouples.

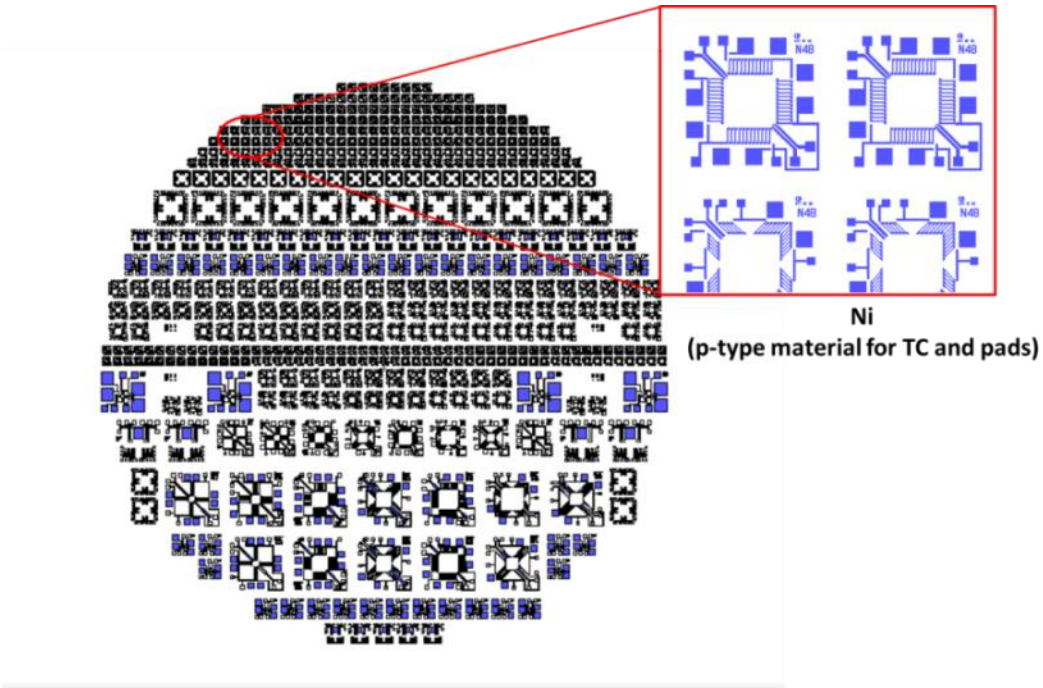

Figure B.3. 3rd mask set for patterning deposited Ni.

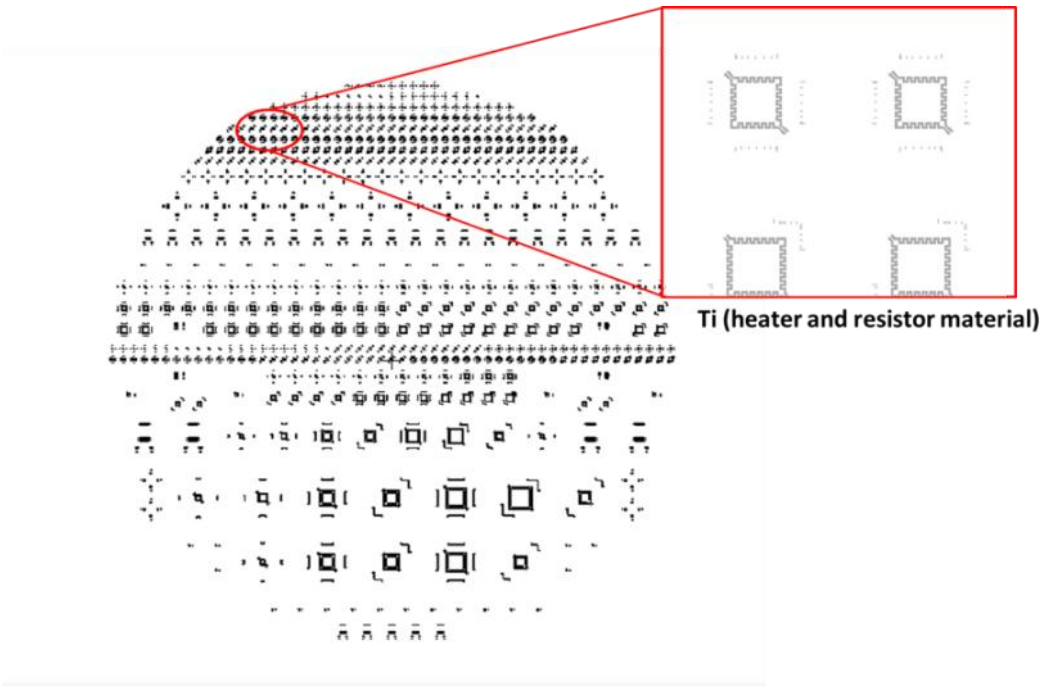

Figure B.4. 4th mask set for patterning deposited Ti.

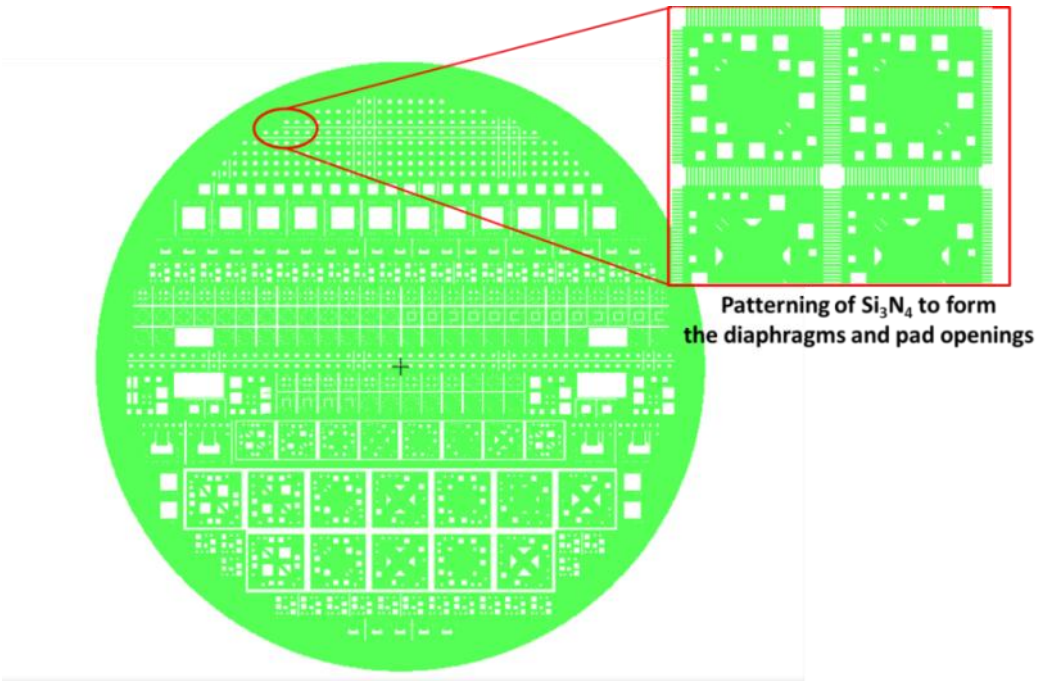

Figure B.5. 5th mask set used to form the diaphragms and pad openings on Si_3N_4.

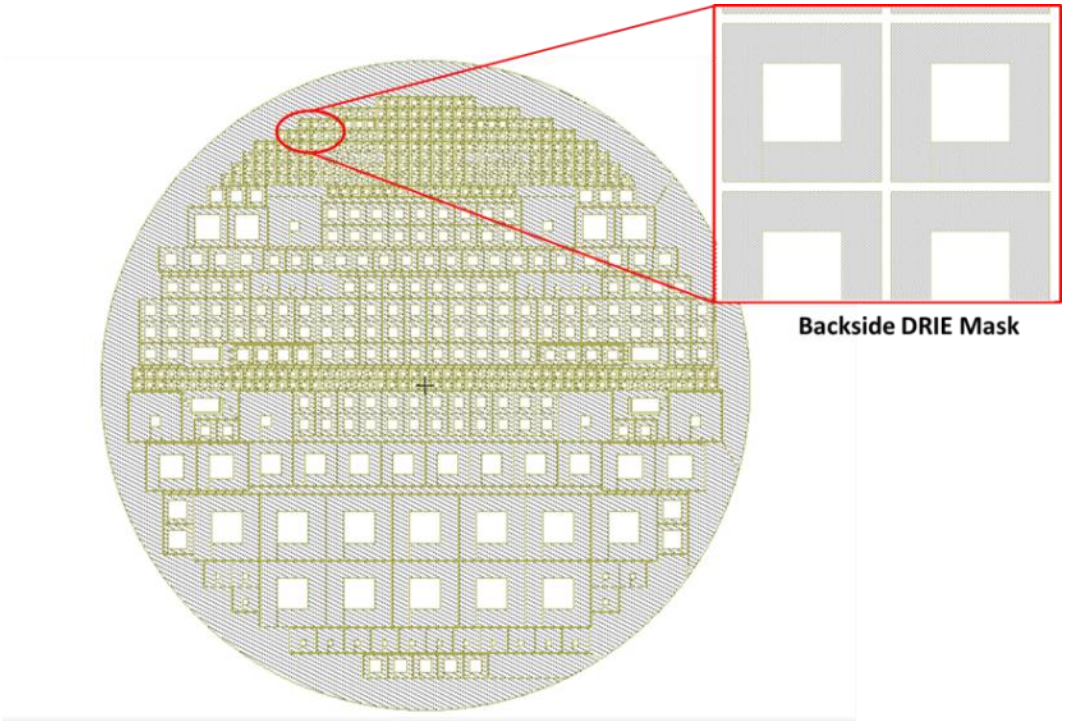

Figure B.6. 6th mask set for releasing the diaphragms.

APPENDIX C

DETAILED FABRICATION FLOW

Table C.1. Low stress Si_3N_4 deposition.

Si_3N_4 deposition by PECVD	A1	Dehydration (pre-deposition)	Dehydrate 20 min. in oven @110°C Cool in desiccator for 5 min.
	A2	Low stress Si_3N_4 deposition	

Table C.2. The process for Cr/Au deposition and Au patterning (Mask 2).

Cr (p-type TE material) and Au (on junctions) deposition and Au patterning (Mask 2)	B1	Dehydration (pre-sputter)	Dehydrate 30 min. in oven @110°C Cool in desiccator for 5 min.
	B2	Cr deposition	Process parameters: 5 mTorr chamber pressure, 300 W RF power, 3000 sec. Total thickness: 120 nm.
	B3	Au deposition	Process parameters: 3 mTorr chamber pressure, 75 W RF power, 400 sec. Total thickness: 20 nm.
	B4	Lithography	

Table C.2 continued.

Cr (p-type TE material) and Au (on junctions) deposition and Au patterning (Mask 2)	B4.1	Dehydration	Dehydrate 30 min. in oven @110°C Cool in desiccator for 5 min.
	B4.2	PR spin	AZ5214E spin @4000 rpm, t=45 s (3 μm aimed)
	B4.3	Soft Bake	Soft bake t=60 sec. over hotplate @110°C
	B4.4	Expose	Expose 7 sec. (Vacuum contact)
	B4.5	Image Reversal Bake	Post bake for image reversal Bake over hotplate @120°C for t=120 sec. Post bake time is critical for image reversal
		Flood exposure	Flood exposure for 15 sec. after image reversal bake
	B4.6	Develop	Develop in MF319 for 70 sec
	B4.7	Descum in O2 plasma	Descum in Nanoplas O2 plasma with 30 sccm O2 flow for 3 min. For removing exposed but undeveloped resist at smaller feature areas.
		Last Bake	Last bake @120°C, 60 sec.
	B4.8	Hard Bake	Hard bake (for wet metal etch) @110°C, 20 min. Cool in desiccator for 5 min.
	B5	Au wet etch	Au etchant for ~14 seconds
	B6	PR Strip	Acetone for 15 minutes + 5 minutes in O2 plasma

Table C.3. The process for Cr patterning to form p-type thermoelectric layer (Mask 1).

Cr Patterning (Metal 1) (Mask 1)	C1	Dehydration (pre-sputter)	Dehydrate 30 min. in oven @110°C Cool in desiccator for 5 min.
	C2	Lithography	
	C2.1	Dehydration	Dehydrate 30 min. in oven @110^0C Cool in desiccator for 5 min.
	C2.2	PR spin	S1813 spin @4000 rpm, t=40 s (1.3 μm aimed)
	C2.3	Soft Bake	Soft bake t=60 sec. over hotplate @115^0C
	C2.4	Expose	Expose 4.5 sec. (Vacuum contact) Optimizing the expose time is essential for smaller features (<2 μm).
	C2.5	Develop	Develop in MF319A for 40-50 sec
	C2.6	Descum in O2 plasma	Descum in Nanoplas O2 plasma with 30 sccm O2 flow for 3 min. For removing exposed but undeveloped resist at smaller feature areas.
	C2.7	Hard Bake	Hard bake (for wet metal etch) @110°C, 20 min. Cool in desiccator for 5 min.
	C3	Cr wet etch	Cr etchant TFD for ~4.5 - 5 minutes + Wash the Cr etchant residue in %3 H2SO4 solution *Rinsing in water should be done carefully after this step. Observe the wafer and wash after neither Cr etchant nor H2SO4 residue remains.
	C4	PR Strip	Acetone for 15 minutes + 5 minutes in O2 plasma

Table C.4. Intermediate Si_3N_4 deposition and patterning to form the vias.

Via patterning (Mask 2)	D1	Dehydration (pre-sputter)	Dehydrate 30 min. in oven @110°C Cool in desiccator for 5 min.
	D2	Low stress Si_3N_4 deposition	Process parameters: X sccm Ar, Y sccm N2 flow. Total thickness: 200 nm.
	D3	Lithography	
	D3.1	Dehydration	Dehydrate 30 min. in oven @110°C Cool in desiccator for 5 min.
	D3.2	PR spin	S1813 spin @4000 rpm, t=40 s (1.3 µm aimed)
	D3.3	Soft Bake	Soft bake t=60 sec. over hotplate @115°C
	D3.4	Expose	Expose 4.5 sec. (Vacuum contact)
	D3.5	Develop	Develop in MF319 for 40 sec
	D3.6	Descum in O2 plasma	Descum in Nanoplas O2 plasma with 30 sccm O2 flow for 3 min. For removing exposed but undeveloped resist at smaller feature areas.
	D3.7	Hard Bake	Hard bake (for RIE etch) @110°C, 20 min. Cool in desiccator for 5 min.
	D4	RIE etch	Process parameters: 80 sec.
	D5	PR Strip	Nanoplas O2 plasma: PR strip recipe for 45+45 minutes. Acetone or SVC bench are not compatible after RIE process. Resist chemical structure deteriorates after reactive ion etching.

Table C.5. Deposit and pattern Ni to form the n-type thermoelectric layer (Mask 3).

Ni (p-type TE material) deposition and patterning (Metal 2) (Mask 3)	E1	Dehydration (pre-sputter)	Dehydrate 30 min. in oven @110°C Cool in desiccator for 5 min.
	E2	Ni deposition	Process parameters: 5 mTorr chamber pressure, 200 W RF power, 5sccm N2 bath gas flow, 1800 sec. Total thickness: 100 nm.
	E3	Lithography	
	E3.1	Dehydration	Dehydrate 30 min. in oven @110°C Cool in desiccator for 5 min.
	E3.2	PR spin	S1813 spin @4000 rpm, t=40 s (1.3 μm aimed)
	E3.3	Soft Bake	Soft bake t=60 sec. over hotplate @115°C
	E3.4	Expose	Expose 4.5 sec. (Vacuum contact)
	E3.5	Develop	Develop in MF319 for 40 sec
	E3.6	Descum in O2 plasma	Descum in Nanoplas O2 plasma with 30 sccm O2 flow for 3 min. For removing exposed but undeveloped resist at smaller feature areas.
	E3.7	Hard Bake	Hard bake (for wet metal etch) @110°C, 20 min. Cool in desiccator for 5 min.
	E4	Ni wet etch	Ni etchant TFG @ 50°C for ~4 minutes
	E5	PR Strip	Acetone for 15 minutes + 5 minutes in O2 plasma

Table C.6. Process for deposition and patterning of titanium heaters (Mask 4).

Ti deposition and patterning (Metal 3) (Mask 4)	F1	Dehydration (pre-sputter)	Dehydrate 30 min. in oven @110°C Cool in desiccator for 5 min.
	F2	Ti deposition	Process parameters: 5 mTorr chamber pressure, 300 W DC power, 1200 sec. Total thickness: 100 nm.
	F3	Lithography	
	F3.1	Dehydration	Dehydrate 30 min. in oven @110°C Cool in desiccator for 5 min.
	F3.2	PR spin	S1813 spin @4000 rpm, t=40 s (1.3 µm aimed)
	F3.3	Soft Bake	Soft bake t=60 sec. over hotplate @115°C
	F3.4	Expose	Expose 4.5 sec. (Vacuum contact)
	F3.5	Develop	Develop in MF319 for 40 sec
	F3.6	Descum in O2 plasma	Descum in Nanoplas O2 plasma with 30 sccm O2 flow for 3 min. For removing exposed but undeveloped resist at smaller feature areas.
	F3.7	Hard Bake	Hard bake (for wet metal etch) @110°C, 20 min. Cool in desiccator for 5 min.
	F4	Ti wet etch	Ti etchant, prepare 100 ml (60% H2O+20% HF+20% H2O2), 25 ml Ti etchant + 1575 ml DI H2O, ~165 seconds (expose the wafer to air every 15 or 30 seconds to accelerate etching by oxidation)
	F5	PR Strip	Acetone for 15 minutes + 5 minutes in O2 plasma

Table C.7. The patterning of Si_3N_4 to form the diaphragms (Mask 5).

Si3N4 deposition and patterning (Mask 5)	F1	Dehydration (pre-sputter)	Dehydrate 30 min. in oven @110°C Cool in desiccator for 5 min.
	F3	Lithography	
	F3.2	PR spin (Backside)	Backside SiO2 is protected by S1813 during BHF etching of diaphragms on the front. S1813 spin @2000 rpm, t=40 s (1.7 µm aimed)
	F3.3	Soft Bake	Soft bake t=70 sec. over hotplate @115°C
	F3.4	PR spin (Frontside)	S1813 spin @2000 rpm, t=40 s (1.7 µm aimed)
	F3.5	Soft Bake	Soft bake t=70 sec. over hotplate @115°C
	F3.6	Expose (Frontside)	Expose 7 sec. (Vacuum contact)
	F3.5	Develop	Develop in MF319 for 50-60 sec
	F3.6	Descum in O2 plasma	Descum in Nanoplas O2 plasma with 30 sccm O2 flow for 3 min. For removing exposed but undeveloped resist at smaller feature areas.
	F3.7	Hard Bake	Hard bake (for wet metal etch) @110°C, 40 min. Cool in desiccator for 5 min.
	F4	Si3N4 wet etch	Etch in BHF solution for about 8 + 8 minutes (until underlying Si is observed)
	F5	PR Strip	Acetone for 15 minutes + 5 minutes in O2 plasma

Table C.8. BHF etch of backside SiO_2 (Mask 6)

Patterning backside SiO_2 to prepare Si for DRIE (Mask 6)	G1	Dehydration (pre-sputter)	Dehydrate 30 min. in oven @110°C Cool in desiccator for 5 min.
	G2	Lithography	
	G2.1	PR spin (Frontside)	Frontside Si_3N_4 and other structures are protected by SPR220-7 during BHF etching of diaphragms on the front. SPR220-7 spin @2000 rpm, t=45 s (9.5 μm aimed)
	G2.2	Soft Bake	Soft bake t=180 sec. over hotplate @115°C
	G2.3	PR spin (Backside)	SPR 220-7 spin @2000 rpm, t=45 s (9.5 μm aimed)
	G2.4	Soft Bake	Soft bake in oven @ 90°C for 35 min.
	G2.5	Expose (Frontside)	Expose 25 sec. (Vacuum contact)
	G2.6	Develop	Develop in MF24A for 1min 40 sec
	G2.7	Descum in O2 plasma	Descum in Nanoplas O2 plasma with 30 sccm O2 flow for 3 min. For removing exposed but undeveloped resist at smaller feature areas.
	G2.8	Hard Bake	Hard bake (for BHF etch) @90°C, 40 min. Cool in desiccator for 5 min.
	G3	SiO2 wet etch in BHF	Backside etch in BHF solution for about 17 minutes (until underlying Si is observed)
	G4	PR Strip	Acetone for 15 min.

Table C.9. Backside DRIE done in STS Pegasus to suspend the membranes.

Backside DRIE to suspend diaphragms (Mask 6)	G1	Dehydration (pre-sputter)	Dehydrate 30 min. in oven @110°C Cool in desiccator for 5 min.
	G2	Lithography	
	G2.1	PR spin (Backside)	AZ9260 double spin 1. Spin @ 2400 rpm for 60 sec.
	G2.2	Soft Bake 1	Soft bake t=80 sec. over hotplate @110°C
	G2.3	2nd PR Spin	2. AZ9260 spin @ 2100 rpm for 60 sec.
	G2.4	Soft Bake 2	Soft bake over hotplate @110°C for 160 sec.
	G2.5	Rehydration	Rehydrate in blue box with 4 pipettes of water for 2 hours.
	G2.6	Expose	Expose for 60 sec. (Vacuum contact or Soft contact) *The features are big in this mask, so soft contact will be satisfactory.
	G2.7	Develop	Develop in AZ826 MIF for ~11 min. (Use stirrer @300 rpm)
	G2.8	Descum in O2 plasma	Descum in Nanoplas O_2 plasma with 30 sccm O_2 flow for 3 min.
	G2.9	Hard Bake	Hard bake (for DRIE etch) 1. Start from 40°C, increase to 90°C and wait (total 30 min.) 2. Increase to 110°C and wait (total 20 min.) 3. Expose to natural cooling in oven till T<60°C 4. Cool in desiccator for 5 min.
	G3	DRIE etch	DRIE etch of backside Si (25 min.)
	G4	PR Strip	Strip in AZ100 remover @80°C, 30 min. If not stripped, 15 min. PRS1000

APPENDIX D

ALTERNATIVE FABRICATION FLOW FOR VERTICAL TE HARVESTERS

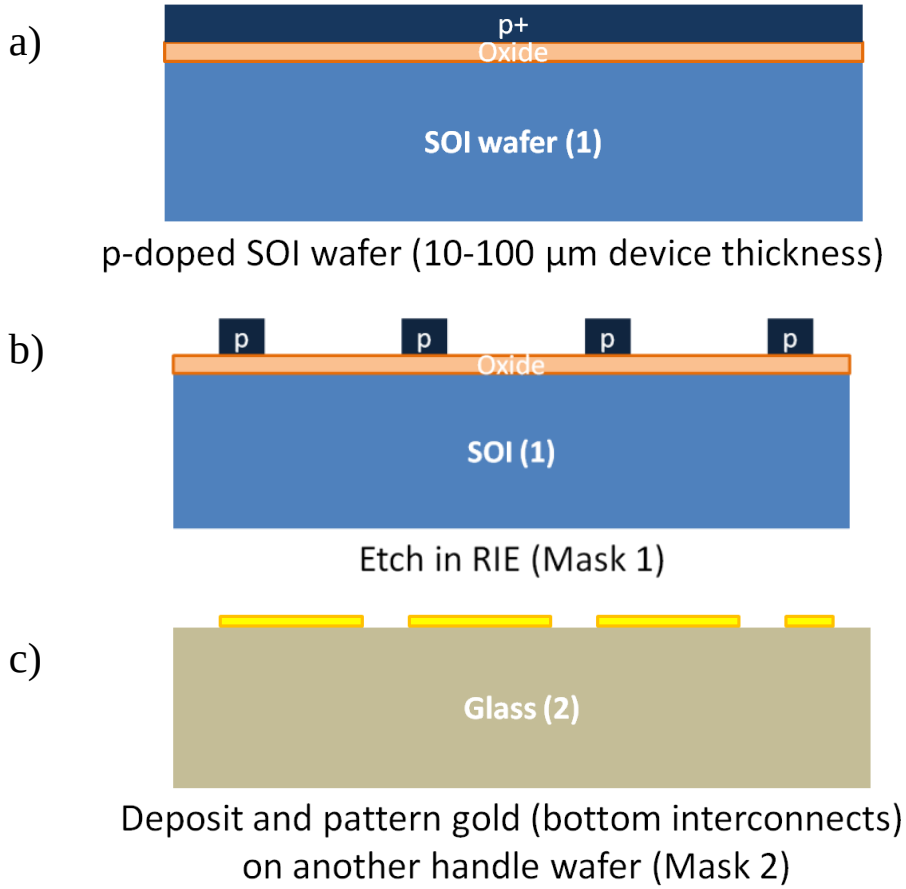

Figure D.1. The alternative fabrication flow for a vertical TE generator configuration. The thermocouple height can be up to 100 µm (or more) according to the SOI device layer thickness.

d)

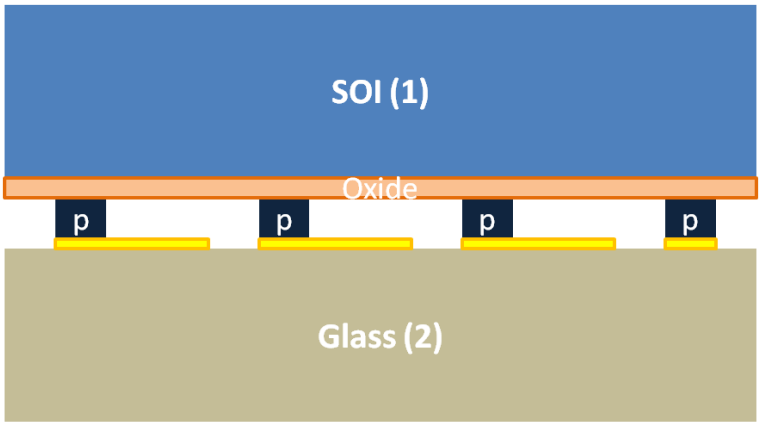

Bond the SOI (1) to the glass wafer (2)

e)

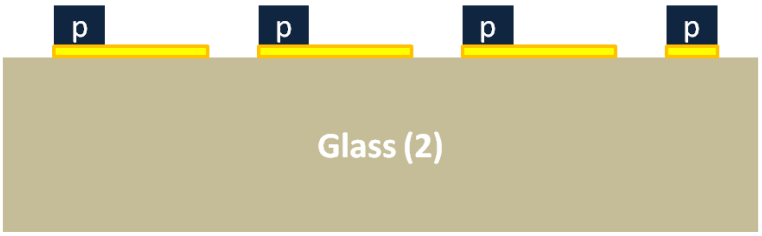

Etch SOI Silicon and SiO_2 in RIE+BHF

f)

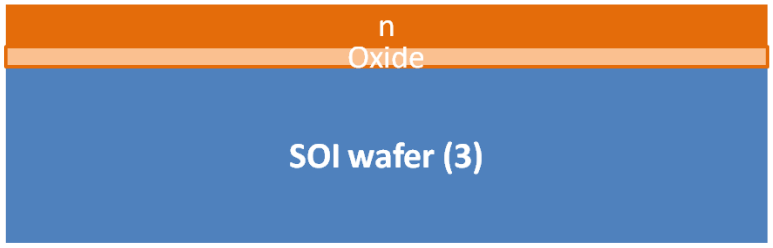

n-doped SOI wafer (10-100 µm device thickness)

Figure D.1 continued.

g)

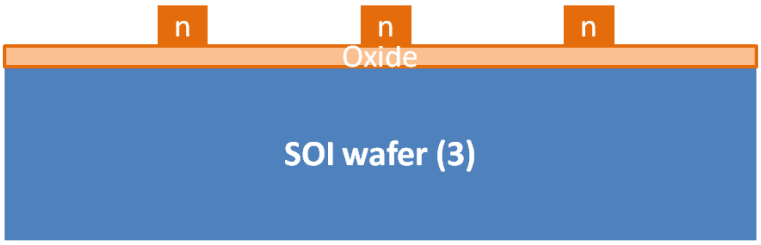

Etch in RIE (Mask 3)

h)

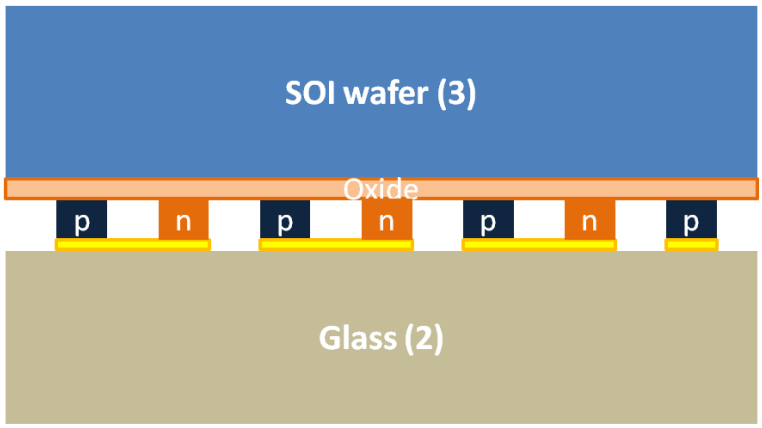

Bond the SOI to the glass wafer having p+ thermolegs

i)

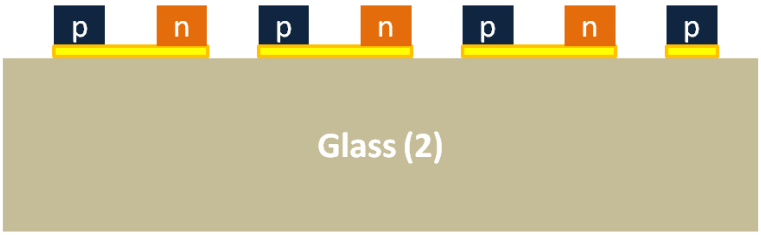

Etch in SOI Silicon and SiO_2 in RIE+BHF

Figure D.1 continued.

j)

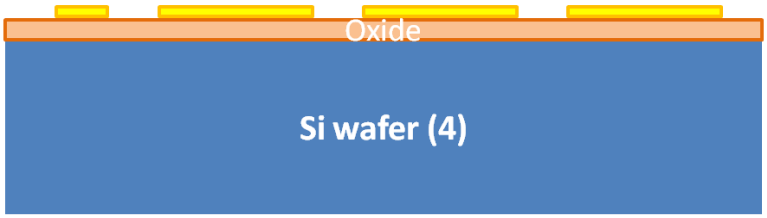

Deposit and pattern gold (top interconnects)
on another Si wafer
(Mask 4)

k)

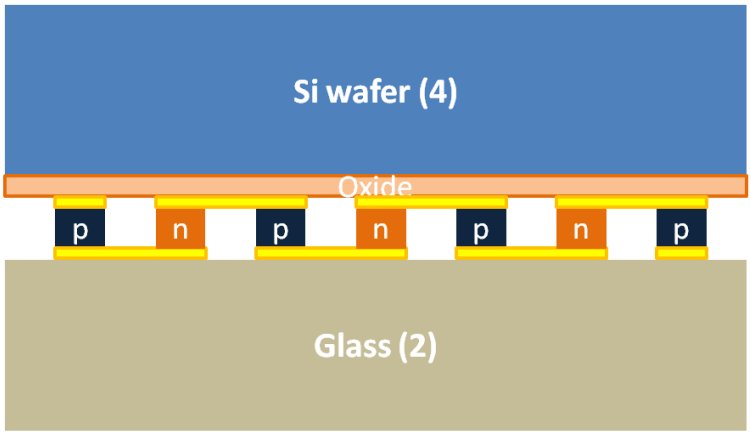

Bond (2) and (4) together to form the vertical TE generator

l)

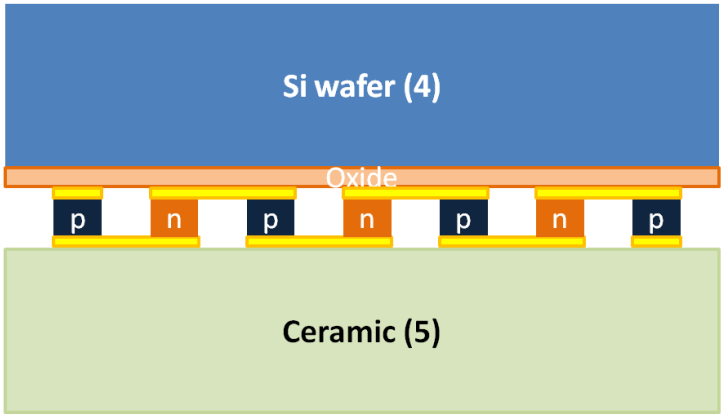

Etch Glass in BHF & bond to a ceramic wafer as
heat spreader or sink

Figure D.1 continued.